

*Attachment I*

U.S.C. AME Report 4-4-2001

**Sonic Boom Noise Penetration Under a Wavy Ocean:  
Part II. Examples and Extensions**

**H.K.Cheng**

Dept. of Aerospace and Mechanical Engineering  
University of Southern California  
and  
HKC Research, Los Angeles, CA

**C.J.Lee**

Applied Sciences Laboratories, Inc.  
Hacienda Height, CA

**J.R.Edwards**

Environment Management Div., SMC/AXFV  
AF Space & Missile System Center, Los Angeles, CA

Prepared for  
SPACE AND MISSILE SYSTEMS CENTER  
AIR FORCE MATERIAL COMMAND

and

PARSONS,  
Under Parsons Subcontract to HKC Research  
738249, 3000-00

## Table of Content

<b>Summary</b>	3
<b>Sec. 1 Introduction</b>	4
<b>Sec. 2 Preliminary Remarks</b>	
2.1 Assumptions and the Interaction Model	4
2.2 Essence of the Theory	5
2.3 Related Studies	6
<b>Sec. 3 Solution Procedures: Basic Steps, key Issues and Feature</b>	
3.1 Solving Direct and Inverse Problems	7
3.2 Supersonic Wave Field	9
3.3 Subsonic Wave Field Underwater	11
3.4 Extension to a More General Class of Surface Wave Forms	15
<b>Sec. 4 Examples with Incident N-Waves</b>	
4.1 Preliminary Remarks	16
4.2 Example of Solution Process: $M_A = 1.82$ , $k = 4$	19
4.3 Test of a General Computer Code: $M_A = 1.5$ , $k = 4$	20
4.4 Underwater Waveform Properties: $M_A$ and $k$ Dependence	20
4.5 Non-Aligned Wave Trains	22
4.6 Multiple Train Interference: “Cross Sea”	23
4.7 Departure From Sinusoidal Surface Waves	25
4.8 Sonic Booms Over Shallow Sea	26
<b>Sec. 5 Application to Rocket Space Launch</b>	
5.1 Known and Anticipated Features	34
5.2 Rocket Space Launch: Infra-sound Under Wavy Ocean	35
<b>Sec. 6 Concluding Remark</b>	37
<b>Acknowledgment</b>	39
<b>References</b>	40
<b>Figure Captions</b>	44
<b>Figures 1 - 41</b>	
<b>Appendices</b>	
Appendix I: Surface Velocity Potential Representing Wavy Surface Response To Sonic Booms	
Appendix II: Underwater Solution Details	
Appendix III: Large- $x$ Expansion Of Surface Velocity Potential	
Appendix IV: Extension To General, Periodic Surface Wave Trains; Synchronous Solution for High $k$ Re-Examined	
Appendix V: Notes On Power- Law Shear Speed Model	

## Summary

Examples of sonic boom noise field under wavy water are studied, based on the theory of Part I, to ascertain the surface-wave influence on sound level, frequency and waveform of the perceivable sonic boom disturbances generated during supersonic aircraft and space launch operations. The study substantiates that, owing to the much lower attenuation rate, the time-dependent disturbances produced by the interaction of incident sonic-boom waves with a sinusoidal surface-wave train can be comparable to and overwhelm the otherwise flat-ocean (Sawyers) wave field at large as well as at moderate depth levels, depending on the surface-wave number  $k$ , the Mach number above water  $M_A$ , and the maximum surface-wave slope,  $\delta$ . Examples of calculations indicate that audible disturbances from aircrafts at levels of 120-130 dB (ref.  $1 \mu\text{ Pa}$ ) can reach a depth of 1000-1500 ft. (300-450 m) where the waveform turn itself into a packet of wavelets with carrier frequency 20-40 Hz. Same dB levels are expected also at comparable depth (200-400 m) for the rocket space launch, but mainly in the low infrasound (1-10 Hz) range. Significant differences between sonic booms from supersonic aircraft and from rocket launch operations in noise characteristics underwater are discussed. Results are obtained for examples in which the surface-wave vector (propagation direction) does not align with the flight track and for examples involving multiple surface-wave trains. As an extension in the theoretical development, the series solution for a non-sinusoidal, periodic surface-wave train is developed, its convergence, and its far-field behavior (under  $kz \gg 1$ ) are established. Importance of the sea-floor presence and the potential for excitation of sediment-interface waves are examined with the model of a shallow sea.

# 1. Introduction

Sonic Boom is recognized as an outstanding environmental impact issue of supersonic aircraft and space-launch operations (Gladwin et al 1988, Stewart et al 1991, Air Force Material command 1997, Office Assoc. Adm. Commercial Space Transportation 2001). Methods for predicting sonic boom overpressure for impact assessments have evolved from ray/geometric acoustics theory (Guiraud 1965, Hayes 1971, Hunter & Keller 1983) and are extensively used for impact studies in many design and program-planning analyses (Walden 1958, Carson & Maglieri 1972, Thomas 1972, Plotkin 1984, Darden 1988).

An important development receiving much attention in recent years addresses the potential sonic boom effects on marine mammals and other forms of sea life (Sawyers 1968, Cook 1970, Water 1971, Intrieri & Malcolm 1973, Sparrow 1995, Sparrow & Ferguson 1997). Most research in this area have been concerned with the sound level and frequency range that may cause permanent or long-term physical harm to the animals, such as lowering in the hearing threshold after exposure to sonic booms (Bowles & Stewart 1980, Bowles 1995, Stewart et al 1991). These works do not address, however, problems underlying the audibility issue which may affect the animals in short and long terms, and has been central to recent studies on man made noise affecting marine mammals (Richardson et al 1995, 1997; National. Res. Council Ocean Study Board Committee 1992; Natural Resource Defense Council 1999; ARPA, NOAA & State of Hawaii 1995).

Our recent study presented in Part I (Cheng and Lee 2000, 2002) indicates significant interaction effects of surface waves on sonic boom noise in deep water. According to the analysis, audible signals perceived in deep, as well as moderately deep, water are significantly different from, and much stronger than, that predicted by the flat-ocean (Sawyers') model. To be used as a guide for studying the audibility issue, prediction methods based on the theory must be critically examined with concrete examples for its capability in predicting overpressure levels, frequency ranges and waveforms at depth levels of relevance to marine mammal studies. This will be the principal focus of the following examinations in Sections 4 & 5, in which examples for incident N-waves at several flight Mach numbers interacting with surface wave trains in a certain wave-number range will be considered. Included in the study are also examples modeling the underwater noise impact from a rocket space launch. Several features of the underwater acoustic field are brought out and model of sediment-interface waves in a shallow sea will be studied in some detail. Section 2 below delineates the interaction model and the theory in its essence, and their relations to other theoretical and experimental studies. Calculation procedures and computation programs used will be briefly explained in Section 3; key analytical details and equations are summarized in Appendices I-III. A theory extension to non-sinusoidal, periodic, surface-wave train is documented in Appendix IV, where an improved far-field analysis for high surface-wave number ( $kz \gg 1$ ), more complete than in Part I, will also be given. Unresolved analytical issues in sediment-wave excitation are noted in Appendix V.

## 2. Preliminary Remarks

### 2.1 Assumptions and the Interaction Model

The theory adopts a model of two adjoining inviscid, compressible media; across the interface the pressure and normal velocity (in the absence of surface tension) are continuous. The water-to-air density ratio  $\rho_w/\rho_A$  is assumed to be much high than unity (being 773.4 under standard condition). Its high density is expected to cause the water to behave very stiffly in response to the incident sonic boom wave,



with little changes in fluid velocities and the interface geometry (to the level of approximation considered); whereas, the overpressure underwater must vary in response to that above water.

The overpressure of interest, to be sure, is the pressure change from the local equilibrium value  $p + \rho gh$  which increases with depth  $z$  (Please refer to Fig. 1 for sign conventions and meanings for the depth and horizontal variables  $z$  and  $x$ , the sea-level signature length  $L'$ , the surface-wave length  $\lambda$ , the horizontal velocity of the wave field trailing the space/aircraft  $U$ , and the surface-wave velocity  $c$ ). As shown in Fig. 1, the surface-wave depression is represented by  $Z_w(x, y, t)$ ; for the sinusoidal surface-wave train considered, the maximum  $Z_w$  (which is one-half of the wave height) is  $\delta\lambda$ , and the maximum slope is  $2\pi\delta$ . Following the convention in Part I, all length scales will be made dimensionless in the out set with the signature length  $L'$ . The velocity  $U$  is assumed to be constant, or nearly uniform in time, and much larger in magnitude than  $c$ ; the latter will be omitted in most applications. Following Part I, the problem formulation and analyses were made in the Cartesian reference frame moving with horizontal velocity  $U$  with respect to the media at rest. Whereas, the corresponding waveform study in the time domain (at various depths) will be made in the rest frame (fixed to the medium at rest); this will allow a more meaningful comparison with sound field normally perceived under water.

The interaction theory considered assumes a small over-pressure ratio  $\varepsilon = (p - p_\infty) / p_\infty$  together with a small surface slope  $\delta$ , so that the interaction effect next to the surface is of the order of  $\varepsilon\delta$  pertaining to a second-order influence. As a valid asymptotic theory, the main requirement is found to be (Cheng and Lee 2002)

$$\varepsilon \rho_\infty / \rho_w \ll \delta$$

The analysis may therefore be expected to hold even if  $\delta$  were comparable or smaller than  $\varepsilon$ , as long as  $\varepsilon$  remains small.

## 2.2 Essence of the Theory

The significance of the surface-wave influence on deepwater wave field is made more apparent by a comparison in the (spatial) attenuation rate between the primary sonic boom disturbances under a flat ocean and the time-dependent disturbances generated by the interaction with a surface-wave train. Whereas the former diminish with increasing depth level as the *inverse square* of the depth, i.e.  $1/z^2$  for an N-like incident waveform, the time-dependent effect from the interaction with surface waves will attenuate, however, as the *inverse square-root* of the depth, i.e.  $1/\sqrt{z}$  in accord with the *cylindrical spreading rule* which is familiar from acoustics for a monochromatic point source in two dimensions [see for example, (Landau & Lifshitz 1959)]. This cylindrical spreading rule is indeed borne out by the 3-D theory in Part I by virtue of the high aspect ratio of the sonic boom impact zone. Hence, this time-dependent interaction effect, though being a secondary one at and near the surface, can exceed Sawyers' prediction in magnitude and overwhelm the otherwise primary wave field at large  $z$ . The manner in which the secondary effect evolves into a dominant feature in deepwater and the several of its unique properties are the results of analytical details worked out in Part I from the interaction model based on the foregoing anticipation.

Underlying the various features of the theory are the time-dependent acoustic source produced by the sonic boom and surface wave interaction, that generate, in turn, a dispersive wave system with a continuous wave-number spectrum. In progressing to deep water, these waves disperse into a packet of

quasi-monochromatic, cylindrically spreading wave-lets. The result overwhelms the otherwise, primary flat-ocean wave field by virtue of their much lower attenuation rate with depth.

Earlier theory and experiment on sound transmission from air to water (Medwin, Helbig & Hagy 1973) have indicated that the transmitted sound level can be augmented with a rough water surface. The results cannot be taken, however, as a direct support to the present work, since, unlike the model of Part I, these earlier studies considered mainly sound transmission in which the wavelength is *short* compared to the signature length.

## 2.3 Related Studies

Most studies of sonic boom effects underwater are based on Sawyers' (1968) flat-ocean model; among these are analytical development elucidating the original theory (Cook 1970) and experiments substantiating certain model predictions and properties (Water 1971, Intrieri & Malcolm 1973). Sparrow (1995) and Sparrow & Ferguson (1997) applied Sawyers' theory extensively to study effect of aircraft flight Mach number and incident waveform. Their studies would suggest that sonic boom noise underwater cannot be important at depth levels more than a signature length.

Whereas the present theory and its results in deep water represent a significant departure from Sawyers' model in deepwater, the analysis was based on the interaction of an incident sonic boom with surface wave of *small* slopes; as noted already, the interaction effect must therefore be secondary compared to the prediction for a flat ocean, at least at small depth level. Thus, Sawyers' model may be regarded as the departure point for the present analysis.

Three experiments on underwater sonic boom noise of relevance to the present work may be cited (Intrieri & Malcolm 1973, Desharnais & Chapman 1998, Sohn et al 1999). Intrieri & Malcolm's measurements were conducted in a (Plexiglas) water tank where the overpressure below the otherwise free surface was produced by an overflying projectile of small caliber, using 0.56 cm diameter Quartz pressure transducers (Kistler model 603 A) flushed mounted on a 17 cm square aluminum plate; the latter was connected through waterproof (microdot) cable to an electrostatic-charge amplifier (Kistler model 566). The projectile Mach number ranges from 2.7 and 5.7 in air, corresponding to Mach 0.6 to 1.3 underwater. The water in the tank prior to projectile firing was quiescent, allowing no surface waves. In the cases with subsonic Mach numbers underwater, the maximum overpressure were found to attenuate with depth in a manner anticipated by Sawyers' (1968) theory, borne out by the Prandtl-Glauert rule (for steady-state aerodynamics). Detailed signature waveform underwater was not recorded.

In Desharnais & Chapman's (1998) work, acoustic signals were recorded during sea trial of a vertical hydro-phone array and were identified subsequently to be the transmitted disturbances from an overflying Concorde airliner at Mach 2.02, and 8 km above. The array spanned the lower 50 m of the 70 m water column above a sand bank. Reasonably good agreement with Sawyer's solution in waveform recorded was found on the upper part of the array. Noticeable from the overpressure recorded in the lower part of the water column is a lee-wave like feature departing from Sawyers' prediction. The feature, referred to as 'ringing' for its prolong monotone character, were attributed by the authors to be the effect of excited sediment-interface wave. Their numerical study addresses the seismic-acoustic interaction of the underwater *infrasonic* waves with the elastic sediment of a model sea bed, and lends support to the ringing effect in question. A solution feature therein which indicate an increasing sediment-wave effect with distance from the sea bed is, nevertheless, difficult to explain; we will examine the possibility for its occurrence in a shallow water study later in Sec 4.8. Interestingly, ringing features similar to that mentioned have also been found in examples of interaction of sonic boom with a surface-wave train later in Section 4; it is unclear, however, if the surface-wave influence could provide a better explanation of the feature in question, since the water were reportedly clam during measurement.

Undersea measurement of sonic boom noise field has recently been made by Sohn et al (1999). It represents a first planned ocean experiment of this kind, including several supersonic overflights together with shipboard overpressure measurements. Six booms were generated by an F-4 aircraft at altitude 0.6-6.0 km and Flight Mach number 1.07-1.26. The recording system employed a vertical hydrophone array suspended from a small buoy, which telemetered data to a nearby research vessel. The sea-level overpressure amplitudes were found to range in 100-200 Pa (2.1-4.2 psf), which was reduced to the 1 Pa (0.021 psf) level at depth 30-40 m corresponding to 1-1.5 signature length, where the signals of interest were reportedly indistinguishable from that of the ambient noise. While the waveform data agreed reasonably well with Sawyers' prediction at depth down to 30-40 m, large discrepancies appear in most records at depth greater than 50 m. The measurement was not extended to depth beyond 70 m in the belief that the ambient noise level at greater depth would have overwhelmed the signals of interest.

As a field experiment to validate Sawyers' model, the study succeeded in demonstrating the model's applicability at depth levels down to one signature length (~40 m). In the interest of the audibility, however, one must recognize the important difference in the expected ambient noise levels between the very-shallow water (~40m) and the deep ocean, or even a shallow sea, according to the classic plots familiar from Wenz's (1962) and Urlick's (1983) studies. These plots give estimated sound pressure spectral densities as function of frequency, and indicates that the ambient noise level at the "very-shallow depths" (say 50 m or less) in the 5-30 Hz frequency range of interest is at the least 20 dB (re 1  $\mu$ Pa) higher than those in the "deep" and "shallow" (not-so-deep) water. Ample evidence from Sohn et al's data suggest that either the recording system or analyzing procedures therein became inadequate for depths 50 m and beyond (deeper). The prevailing sea state reported during the tests indicate that ocean waves were present, though regarded as being relatively calm. It is also unclear why the time-domain (waveform) were not described at time interval beyond half a second which would have revealed the noted ringing features. Finally, the rather limited flight-Mach number range of 1.07-1.26 in Sohn et al's work represents still another limitation of the experiment, in as much as our theory in Part I (explained in Section 4), shows that the lateral (y-) extent of the impact zone, where the surface-wave influence can manifest, becomes very small as the flight Mach number fall below 1.25. Even in the vertical plane directly under the flight track (y=0), the effect of interest cannot be detected for flight Mach number lower than 1.25, unless the surface-wave vector aligns closely with the flight track.

### 3. Solution Procedures: Basic Steps, Key Issues and Features

#### 3.1 Solving the Direct and Inverse Problems

Since the surface-wave slopes are assumed to be small, the interaction effect in question can be treated as a higher-order, nonlinear correction to the linear, flat-ocean (Sawyers) theory. As such, the equations governing the wave fields above and under water of interest can be linearized in successive approximations, and analyzed in a reference frame moving (with respect to a rest frame) at a velocity  $U$ . The problem is further simplified by the high water-to-air density ratio, which allows omission of surface-shape change in the determination of the interaction effect above water. The solution for the perturbation velocity-potential above water may then be obtained as that of a *direct* problem in aerodynamics, in which the (time-dependent) boundary conditions for the normal velocity on the interface are known *a priori* (at each stage of the approximation). With the sea-level (time-dependent) overpressure determined by the solution above water given as an input, the wave field underwater (at a lower Mach number) will be solved as an *inverse* problem in which boundary value of the overpressure of interest is given completely on the interface. In carrying out the perturbation analysis, the boundary conditions at the impermeable interface will be transferred analytically to the reference surface  $z=0$ ; this transfer contributes to an additional nonlinear, secondary correction.

### *Time-Dependent Solution as a Secondary Wave Field*

It is essential to note once again that, unlike other secondary on nonlinear effects which attenuate with distance rapidly (as do the primary disturbances), the surface-wave interaction effect of interest, owing to its much lower attenuation rate, dominates the secondary corrections and, in fact, overwhelms the primary wave field at a sufficiently large  $z$ .

The acoustic wave field is therefore composed of two parts, the primary and the secondary, for each of the two media. In the moving frame, the primary wave field is that corresponding to a steady, 2-D supersonic flow ( $M_A > 1$ ) in the air (above water) and to a steady 2-D subsonic flow ( $M_w < 1$ ) under water (for  $M_A > \rho_w / \rho_A = 4.53$ ). Applied to a bottom-free model ocean, the latter recovers the Sawyers theory. Adopting the notations of Part I, the perturbation velocity potential will be analyzed in the form of

$$\phi' = \phi'_1(x', z'; y') + \phi'_2(x', z'; y', t) \quad (3.1)$$

with a similar decomposition for the overpressure  $p'$ . Note that  $x'$ ,  $y'$ , and  $z'$  are the *normalized local* Cartesian variables with  $y'$  being the coordinate along either the (curved) centerline or leading edge of the surface impact zone (cf. Fig. 2).

### *Synchronous Wave Field Mode*

An important feature of the present model is the assumption of the sinusoidal surface waveform described by

$$\begin{aligned} z &= Z_w(\underline{x}, \underline{y}; t) \\ &= \delta\lambda \exp i[k_1 \underline{x} + k_2 \underline{y} - \omega t] \end{aligned} \quad (3.2a)$$

in a *rest* frame  $(\underline{x}, \underline{y}, \underline{z}; t)$ . In the moving frame, and under the assumption that the (span wise) variation along the centerline is relatively small,  $Z_w$  can be expressed as

$$Z_w = \delta\lambda \exp i[k'_1 x' + k'_2 y' - \Omega t], \quad (3.2b)$$

where

$$k'_1 = k \cos(\Lambda + \psi), \quad k'_2 = k \sin(\Lambda + \psi) \quad (3.2c)$$

$$\Omega = ck + Uk_1 = k(U \cos \psi + c).$$

Here,  $\Lambda$  is the local centerline swept angle of the surface-impact zone (cf. Fig. 2) which determines the normal Mach number  $M_n = U \cos \Lambda / a$  at the span station of interest, and the  $k'_1$  and  $k'_2$  are the two components of the surface-wave vector  $\vec{k}$  whose magnitude is  $k = 2\pi/\lambda$ . As indicated in Fig. 2,  $\psi$  is the angle that the surface wave-number vector made with the flight track. At  $\psi=0$ , the surface-wave vector aligns itself with the flight direction;  $\psi$  may be referred to as the “angle of non-alignment”. Part I has shown, and the subsequent study will confirm, that there is a wide range of  $\psi$  for which the surface-wave influence on the deep-water acoustics is significant.

The contribution from  $c$  to the normalized frequency  $\Omega$  in (3.2c) is generally small and will be omitted. This is because the wave trains move so much slower than the sonic boom wave field that it can be regarded as standing still. The assumptions of (3.21), together with the high aspect ratio of the surface-impact zone, allow one to treat the secondary acoustic field as one in a *synchronous* form, including a sinusoidal span wise dependence in  $y'$ .

After normalizing  $\phi'$  and  $p'$  with the appropriate scales, their primary and the principal secondary components may then be expressed as

$$\phi' = \phi'_1(x', \bar{z}, y') + \delta \hat{\phi}_2(x', \bar{z}) e^{ik'_2 y'} e^{-i\Omega y} \quad (3.3a)$$

$$p' = p'_1(x', \bar{z}; y') + \delta \hat{p}_2(x', \bar{z}) e^{ik'_2 y'} e^{-i\Omega t} \quad (3.3b)$$

where  $\bar{z} = |1 - M_n^2|^{1/2} z$ , and the dependence of  $\hat{\phi}$  and  $\hat{p}$  on the parameter set  $(M, \Lambda, k'_1, k'_2)$  or  $(M_n, k, \Lambda, \psi)$  is expected. The justification for considering  $(x, y, z)$  and  $(x', y', z')$  as *local Cartesians* rests with the assumption of a high aspect ratio for the sonic-boom impact zone on the ground or the sea level.<sup>1</sup>

### *Time-Domain Description in Rest Frame*

The time-domain waveform observed in a rest frame is of interest, since it offers a closer comparison with laboratory/field measurement and with signal perceived by a (slowly) swimming mammal/fish. In terms of a time  $t$  (normalized by  $L'/U$ ), the synchronous wave field in the moving frame can be described as a transient wave group in a *rest* frame with the same functional forms for  $\phi'$ , and  $p'$  (3.3a,b), except for the replacement of the variable  $x'$  in  $\hat{p}_2(x', \bar{z})$  by the substitution

$$x' = t \cos \Lambda \quad (3.4)$$

## **3.2 Supersonic Wave Field**

### *Leading Approximation*

Of interest are the  $\phi'$  and  $p'$  on top of the interface (3.2b), which will provide the boundary data for the problem underwater. To the leading order, the perturbation velocity potential above water, can be described by a form familiar from the Prandtl-Glauert theory

$$\phi_1 = f(x' + B_n z) + f(x' - B_n z) \quad (3.5)$$

where  $B_n$  is  $\sqrt{M_n^2 - 1}$  and  $f$  is a continuous function of the argument  $(x' \pm B_n z)$  with piecewise continuous derivatives, allowing shock-like, slope discontinuities. It satisfies the condition on the impermeable *flat* surface  $z=0$  where the overpressure is proportional to  $-2f'(x)$ . Here, the superscript prime stands for a derivative.

---

<sup>1</sup> A small price to be paid for this simplification is that since  $k'_2$  will not be strictly uniform span wise, it results in a slight phase difference between neighboring span stations. It is harmless otherwise.

### Synchronous Solution via Laplace Transform

Since the water is so *stiff* in its response to sonic boom, the surface-wave geometry cannot depart appreciably (in the leading approximation) from the assumed shape (3.2b). The secondary, time-dependent wave field above water may therefore be analyzed as a *direct* problem with the known shape of a time-dependent wavy wall – without the need of knowing a priori, or simultaneously, the corresponding wave field underwater. The spatially dependent part of the synchronous solution of (3.3a), i.e.  $\hat{\phi}_2(x', \bar{z})$ , which satisfies the governing PDE and the transferred boundary condition at the reference surface  $z=0$ , can be explicitly determined by the Laplace transform method. The result of  $\hat{\phi}_2(x', 0)$  obtained for an arbitrary  $f(x)$  is expressible after inversion in a convolution integral form, involving the Bessel function of the first kind, order zero, and parameters  $B_n$ ,  $k'_1$ ,  $\alpha$ , and  $\mu$ . These parameters are function of  $M_n$ ,  $k$ ,  $\Lambda$ , and  $\psi$ . The result was given in Part I (5.8a), and is reproduced in an equivalent form along with relation among the various parameters in appendix I, Section I.1. Essential to the subsequent underwater analysis is the overpressure distribution on the wavy surface, transferred (analytically) to the reference surface  $z=0$ . They will be evaluated from  $\phi_1(x', 0; y)$  and  $\phi_2(x'; 0)$ , respectively as

$$p_1(x', 0; y') = -\frac{\partial}{\partial x'} \phi_1(x', 0; y') \quad (3.6a)$$

$$\hat{p}_2(x', 0) = -e^{ik'_2 y'} e^{-i\Omega t} \left( \frac{d}{dx'} - ik'_2 \right) \hat{\phi}_2(x', 0) \quad (3.6b)$$

### The Case of an Incident N-wave

Commonly studied in the sonic boom impact analysis is the incident N-wave reaching the sea level, for which the derivative of function  $f(x')$  in (3.4) can be written as

$$\begin{aligned} f'(x') &= (2x' - 1)l(x')l(1 - x') \\ &= (2x' - 1)[l(x') - l(x' - 1)] \end{aligned} \quad (3.7)$$

where the leading and trailing edges of the N-waves are identified with  $x'=0$  and  $x'=1$ , respectively, and  $l(x')$  stands for a unit step function in  $x'$ . The lowest value of  $f'(\xi)$  occurring at  $\xi=0$  corresponds to the normalized peak pressure there. Explicit, analytical results can be obtained for this case, with which certain singular solution behaviors have been unambiguously examined in Part I; they prove to be valuable for assessing and implementing the numerical methods in the present study. With (3.7), the expression of  $\hat{\phi}_2$  for the N-wave takes on a special form which distinguishes three ranges of  $x'$ :

$$x' < 0, \quad 0 < x' < 1, \quad \text{and} \quad 1 < x'.$$

The results of the surface velocity potential  $\phi(x', 0)$  in a normalized form are reproduced in Sec. I.2 of Appendix I. A development of  $\phi$  for large  $x$  has proven to be useful in ascertaining the validity and accuracy of a more general numerical program for computing  $\phi$ , and is given later in Appendix III. A remark on the length scale used in normalizing  $x'$ , for the evaluation of  $\hat{\phi}_2$  may be added. If the local chord were not used as a length scale,  $f'(\xi)$  will not vanish at  $\xi \geq 1^+$  as in (3.6). But the expressions derived for the N-wave from (3.6) may still be used with a readjustment in the magnitudes of the parameters  $k'_1$ ,  $\alpha$ ,  $\mu$ , and the  $\delta$ . Similar readjustment would be needed also for these parameters in the underwater calculations (see Section 3.3 below).

An important function in the underwater analysis below is the Fourier transform of the  $\hat{p}_2(x', 0)$  determined from  $\hat{\phi}_2$  above the water (3.5b). There is, however, an additional part contributing to the  $\hat{p}_2$  at the reference surface  $z=0$  underwater,  $\Delta P_{BT}$ , resulting from the boundary-condition transfer. The latter (unlike that above water) is not negligible (cf. Part I and Section 3.3 below).

### 3.3 Subsonic Wave Field Underwater

The PDE and the parameters  $P$  and  $Q$  governing the underwater synchronous field are the same as above water, except that the normal Mach number therein is less than unity ( $M_n < 1$ ).

#### *Leading Approximation in Hilbert-Integral Form*

With the value of  $p_1$  above water being known at the reference plane  $z=0$ , it proves convenient to obtain the  $p_1(x', \bar{z})$  underwater in the form of an Hilbert integral

$$p_1 = IP \frac{1}{\pi} \int_{-\infty}^{\infty} \frac{p_1(x'_1, 0) dx'_1}{x'_1 - \zeta} \quad (3.8)$$

where  $\zeta$  is the complex variable embodying the subsonic Prandtl-Glauert similitude (in the moving frame)

$$\zeta = x' + i\beta_n z,$$

$$\beta_n = \sqrt{1 - M_n^2}$$

and “IP” is the acronym for Imaginary Part. This reproduces the solution underlying Sawyer’s model for a bottomless, flat ocean. The result can be expressed in explicit, analytic form for an incident N-wave (Appendix II, Sec. II.1).

#### *Synchronous Wave Field via Fourier Transform*

The time-dependent, 3-D overpressure field of (3.3b) is obtained by solving the *inversed, half-plane* problem underwater for the  $\hat{p}_2(x', \bar{z})$  with its boundary value given in the reference surface  $z=0$ :

$$\hat{p}_2(x', 0) = \hat{p}_{2A}(x', 0) - \left( \frac{\partial p_1}{\partial \bar{z}} \right)_o \beta_n \hat{Z}_w(x') \quad (3.9)$$

where  $\hat{p}_{2A}(x', 0)$  is that determined from (3.6b) above water,  $\hat{Z}_w$  is  $Z_w / \exp i(k'_2 y' - \Omega t)^2$ , and the subscript “o” refers to the condition at  $z=0$ .

The synchronous underwater overpressure will be obtained (later) as the inverse of the Fourier transform (with respect to  $x'$ )

$$FT \hat{p}_2(x', \bar{z}) = \frac{1}{\sqrt{2\pi}} \int_{-\infty}^{\infty} e^{i\xi x'} \hat{p}_2(x', \bar{z}) dx' \quad (3.10)$$

---

<sup>2</sup> Note that, above water  $\partial p' / \partial z$  vanishes with  $\bar{z}$ .

where “FT” stands for Fourier Transform;  $FT \hat{p}_2$  is a function of the transform parameter  $\xi$  and also the spatial variable  $\bar{z}$ . The Fourier transform of the PDE governing  $\hat{p}_2(x', \bar{z})$  underwater yields an ODE in  $\bar{z}$  for  $FT \hat{p}_2$

$$\left( \frac{\partial^2}{\partial \bar{z}^2} - \bar{K} \right) FT \hat{p}_2 = 0 \quad (3.11a)$$

$$\bar{K} = \frac{K}{\beta_n^2} = [\beta_n^2 \xi^2 - P\xi - Q] / \beta_n^2 \quad (3.11b)$$

where in addition to  $P$  and  $Q$ ,  $\xi$  appears as a parameter.<sup>3</sup> The  $K$  is being used in Part I and most of the computer programs below. The parameter  $\xi$  has the significance of a *wave number* in the underwater field, and may be referred to as such.

The important boundary data on the (reference) half plane  $\bar{z}=0$  is the Fourier transform of  $\hat{p}_2(x', 0)$  in (3.9)

$$\hat{A}(\xi) = FT \hat{p}_2(x', 0) = \frac{1}{\sqrt{2\pi}} \int_{-\infty}^{\infty} e^{i\xi x'} \hat{p}_2(x', 0) dx' \quad (3.12)$$

The solution to (3.10) is relatively simple:

$$FT \hat{p}_2(x', \bar{z}) = \hat{A}(\xi) \sigma(\xi; \bar{z}) \quad (3.13a)$$

with

$$\begin{aligned} \sigma(\xi; \bar{z}) &= \exp\left(-|\bar{K}|^{\frac{1}{2}} \bar{z}\right), \quad \bar{K}(\xi) > 0 \\ &= \exp\left(i|\bar{K}|^{\frac{1}{2}} \bar{z}\right), \quad \bar{K}(\xi) < 0 \end{aligned} \quad (3.13b)$$

This yields a vanishing far field as  $\bar{z} \rightarrow \infty$  for  $\bar{K} > 0$  and an un-attenuated sinusoidal behavior in  $\bar{z}$  for  $\bar{K} < 0$ . Together with the factor  $e^{-iKz}$ , the latter represents downward propagating waves (in the positive  $\bar{z}$  direction) and hence the correct far-field *radiation condition*. The values  $\xi_1$  and  $\xi_2$  where  $\bar{K}$  vanishes mark the transition between two very distinct behaviors. These two  $\xi$ -values are determined algebraically by the  $P$  and  $Q$  form  $K(\xi)=0$ . The wave components  $\xi$  in the positive  $\bar{K}$  range, characterized by the exponentially attenuated behavior, may be called *evanescent* waves, as in optics. Whereas, those in the negative  $\bar{K}$  range may be referred to as *effervescent/radiating* wave components by virtue of the non-attenuating sinusoidal behavior in  $\bar{z}$ . Nevertheless, the interference effects of

---

<sup>3</sup> Cf. Appendix I, Sec. I.1:  $P = 2M_n^2 k_1' = 2kM_n^2 \cos(a + \psi)$ ,  
 $Q = M_n^2 k^2 - (k_2')^2 = k^2 [M_n^2 \cos^2(a + \psi) - \sin^2(a + \psi)]$



combining the radiating sinusoidal waves of different wave number  $\xi$  results in a behavior that also leads to a vanishing  $\hat{p}_2$  field in deep water (cf. 3.4 below).

The field of  $\hat{p}_2$  of interest is therefore

$$\hat{p}_2(x', \bar{z}) = \frac{1}{\sqrt{2\pi}} \int_{-\infty}^{\infty} e^{-i\xi x'} \hat{A}(\xi) \sigma(\xi; \bar{z}) d\xi \quad (3.14)$$

Equation (3.14), together with (3.8), is the basis for the subsequent numerical computation of the  $\hat{p}_2$  and  $p_1$  underwater. The  $\hat{A}(\xi)$  in (3.14) can be computed for an arbitrary incident wave,  $f(x)$ , by taking the Fourier transform of  $\hat{p}_{2A}(x', 0)$  above water, corrected by the boundary-transferred term, as in (3.9). A fully explicit analytic form of  $\hat{A}(\xi)$  was obtained for the case of an incident N-wave in Part I, and is reproduced in Appendix II, with a slight generalization.

### Resulting $\hat{p}_2$ Behavior

Of interest is the combined effect from all the admissible wave components.. The large- $\bar{z}$  behavior of each individual  $\xi$ -component is seen to depend on the function  $\sigma(\xi, \bar{z})$  in (3.13b). It gives *two* distinct behaviors of  $\hat{p}_2$  at large  $\bar{z}$ . If the  $\bar{K}$  is positive (and non-zero) for *all*  $\xi$ , it can be shown that  $\hat{p}_2$  must attenuate with increasing  $\bar{z}$  at a rate *faster than* the exponential rate shown earlier for an individual  $\xi$ , (3.13). A parameter domain in  $M_n$ ,  $\Lambda$ , and  $\psi$  indeed exists for such a condition, this realm of in  $M_n$ ,  $\Lambda$ , and  $\psi$  may be referred to as a purely *evanescent domain*.

On the other hand, there exists the parameter domain where  $\bar{K}$  cannot remain *thoroughly* positive, i.e.  $\bar{K} < 0$  in some  $\xi$ -range, namely  $\xi_1 < \xi < \xi_2$ . In this parameter domain, application of stationary phase or steepest-descent method to (3.14) with the property of (3.13a,b), detailed in Part I, yields readily a  $\hat{p}_2$  behavior that attenuates with increasing depth as an *inverse square-root* of  $\bar{z}$ , being much slower than that in the evanescent domain (see below). Note that each of the individual components would have led to an undiminished  $\hat{p}_2$ , had there not been the *destructive interference* effect among neighboring components; the final result obtained represents, in fact, the contribution from a  $\xi$ -neighborhood with the *least* destructive interference. The  $(M_n, \Lambda, \psi)$  domain where  $K$  can fall below zero in some interval  $[\xi_1, \xi_2]$  will be called the *effervescent/radiating domain* (even though individual  $\xi$ -components outside of  $\xi_1 < \xi < \xi_2$  attenuate exponentially as an evanescent wave component). This domain may also be called the *cylindrical-spreading domain* for its resulting  $\hat{p}_2$  behavior. Interestingly, the overall contributions to  $\hat{p}_2$  by the branches  $\xi < \xi_1$  and  $\xi_2 < \xi$  are of the order  $(\bar{z})^{-2}$  which is comparable to that in the flat-ocean model. The cylindrical-spreading domain has also been called the domain of *downward propagating waves* in Cheng and Lee (2002).

Owing to its importance to the designs of laboratory and field experiment, the boundaries delimiting these two parameter domains of distinctly different behavior in deep water are reproduced from Part I in Fig. 3 for four flight Mach numbers based on the speed of sound above water:  $M_A = 1.05, 1.50, 2.00$ , and  $3.00$ . They are determined by the requirements

$$M_w^2 \cos^2 \Lambda - \sin^2(\Lambda + \psi) = 0 \quad (3.15a)$$

$$\Lambda = 90^\circ - \sin^{-1}\left(\frac{1}{M_A}\right) \quad (3.15b)$$

where the subscripts “w” and “A” refer to underwater and above water, respectively. The cylindrical-spreading domain is enclosed by these boundaries. The first condition corresponds to  $\xi_2 = \xi_1 = 0$  and the second to the limit set by the Mach cone angle.

### *Analytic Expression at Large Depth ( $\bar{z} \gg 1$ )*

An analytic expression of  $\hat{p}_2(x', \bar{z})$  for large  $\bar{z}$  not only will facilitate the task of predicting the surface-wave influence, but also illustrates the several distinct features of the deepwater sonic boom noise filed more explicitly than otherwise. Owing to its importance for the interpretation and validation of numerical calculations, the large- $\bar{z}$  expression for  $\hat{p}_2(x', \bar{z})$  of the effervescent/radiating domain derived in Part I is reproduced below.

$$\hat{p}_2(x', \bar{z}) = \sqrt{\frac{S_w}{2\beta_{nw}^2}} \frac{\hat{A}(\xi_*)}{(1 + \eta^2)^{3/4} \sqrt{\bar{z}}} \exp\left(i \left[ (2\beta_{nw}^2)^{-1} (S_w \sqrt{1 + \eta^2} - P_w \eta) \bar{z} - \frac{\pi}{4} \right] \right) \quad (3.16a)$$

where

$$\beta_{nw} = \sqrt{1 - M_n^2},$$

$$M_{nw}^2 = M_w^2 \cos^2 \Lambda \quad (3.16b)$$

$$P_w = 2kM_{nw}^2 \cos(\Lambda + \psi), \quad S_w = 2k\sqrt{M_{nw}^2 - \sin^2(\Lambda + \psi)}$$

$$\eta = \frac{x'}{\bar{z}} = \frac{x'}{\beta_{nw} z}, \quad \xi_* = \frac{\left[ P_w - S_w \frac{\eta}{\sqrt{1 + \eta^2}} \right]}{2\beta_{nw}^2} \quad (3.16c,d)$$

The  $\xi_*$  is seen to be a function of  $\eta$  and parameter  $M_A, k, \Lambda$ , and  $\psi$ , and is determined by the stationary phase of the integrand of (3.14); it ranges within the two limits  $\xi_1$  and  $\xi_2$

$$\xi_{1,2} = [P_w \mp S_w] / 2\beta_{nw}^2 \quad (3.16e)$$

As before, the subscripts “A” and “w” refer to the media above water and underwater, respectively. For the case of an N-wave, including the *unbalanced* one,  $\hat{p}_2$  of (3.16a), with  $\hat{A}(\xi)$  given in appendix II, Sec. II.2, can be expressed in a *completely* explicit analytic form.

In applying the synchronous solution (3.3a,b) to deep water in a rest frame, using the  $\hat{p}_2(x', \bar{z})$  of (3.16a), the  $\eta$  and  $\xi_*$  of (3.16c,d) therein must be evaluated with the  $x'$  replaced by the substitution  $x' = t \cos \Lambda$ , as noted earlier in (3.4). The Fourier transform of  $\hat{p}_2$  for the moving frames,  $\hat{A}(\xi) \mathfrak{T}(\xi; \bar{z})$  of (3.13a,b) will be seen in the rest frame in the same form, except that the wave-number  $\xi$  therein should be replaced with a frequency  $\bar{\omega}$  (normalized by  $U/L'$ ) through the substitution (cf. Sec. 7.A in Part I).

$$\xi = \bar{\omega} \sec \Lambda - k \cos(\Lambda + \psi) \quad (3.17a)$$

At a monitoring station directly under the flight track, it suffices to use the substitution

$$\xi = \bar{\omega} - k \cos \psi \quad (3.17b)$$

### 3.4 Extension to More General Classes of Surface-wave Forms

Apart from allowing super-positions of several synchronous solutions pertaining to different horizontal surface-wave number, i.e., different  $k$ 's and  $\psi$ 's, extensions of the analysis to surface-wave trains much more general than the sinusoidal one can be made for the class of surface waves

$$Z_w = F(k_1 x + k_2 y - \omega t) \quad (3.18)$$

which must be *periodic* in the argument  $\chi = k_1 x + k_2 y - \omega t$  with the period  $2\pi$ . As is in the theory of Part I, the assumption of a continuous and integrable  $F(\chi)$ , but allowing a finite number of slope discontinuities in each period, is implicit. The surface-depression function  $F(\chi)$  may then be represented by a Fourier series in “ $\chi$ ” with period  $2\pi$ , which is *absolutely* convergent (Churchill 1941, Pipes 1946). The wave-field solutions above and under water can be determined for each Fourier component of  $F(\chi)$ , applying the synchronous solutions for  $k, 2k, 3k, 4k, \dots$ .

The validity and properties of the resulting series-solution can be established on the basis of the Fourier series of the periodic surface-wave function  $F(\chi)$ . Crucial to the convergence of the resulting solution series is the properties of  $\hat{p}_2$  for a large  $k$ . With this property, the series solution may then be shown to converge *absolutely* (and uniformly). Thereby, the important feature that the overpressure magnitude reduces as  $1/\sqrt{z}$  can be established for this more general case. Appendix IV outlined steps for the proof, including an analysis for large and small  $k$ . More general/complex surface wave patterns can be built up with several or a series of periodic function  $F(\chi)$ , each with its own fundamental  $k$ -vectors.

The study can be extended further to treat problems with surface motions for which a distinct period cannot be identified, such as one generated from a *continuously distributed* wave-number/frequency *spectrum*. The attenuate rate of the inverse square root cannot be expected to hold in this case, owing to the unfavorable interference effects (once again) of the neighboring wave components. For such surface waves propagating in one direction, the underwater disturbances from its interaction with the sonic boom may be shown to diminish inversely as the *first power* of the depth  $z$ ; this rate is still considerably lower than the inverse square law for the flat-ocean model. For the continuous distribution

over a *narrow* wave-number band, nevertheless, the results of a train with distinct wave number will, of course, be recovered. These properties will also be examined in Appendix IV.

### 3.5 Remarks on the Numerical Methods

Standard numerical procedures were employed in computing the derivatives and integrals derived in the theory, which are given explicitly in the Appendices. Specifically, central-difference algorithm and trapezoidal-rule, or their equivalent, were used for the differentiation and integration, except near singularities where calculations were implemented with known functional behaviors to maintain second-order accuracy (in step/mesh size). For the principal value (PV) of an integral with a pole-type integrand, the evaluation is made by assigning the pole to the mid point of the interval (of the ranging variable) enclosing it; the PV so evaluated is expected to have a second-order accuracy, unless the integrand's singularity were stronger than a simple pole.

For the numerical evaluation of the function  $\hat{A}(\xi)$ , it would appear to be unclear a priori how far the integration with respect to  $x$  should be carried out for its adequate descriptions in the vicinities at  $\xi_{A1}$ ,  $\xi_{A2}$ , and other of its singularities. This is because these descriptions will depend on the  $\hat{p}_2$  or  $\hat{\phi}_2$  at large  $x$ . In this regard, the availability of an analytic (exact) results of  $\hat{A}(\xi)$  for the case of an incident N-wave, along with the corresponding large- $x$  description of  $\phi_2$ , has proven to be very useful in helping to determine/ascertain the need of performing numerical integration for  $\hat{A}(\xi)$  beyond a certain (large)  $x$ -value (See below in Sec. 4, and Appendix III).

## 4 Examples with Incident N-Waves

We consider the N-shape waveform as being typical of aircraft sonic booms. For incident N waves, analytic formula for explicit calculations are available from Part I and are applied below to ascertain the importance of the surface Mach number  $M_A$ , surface-wave number  $k$ , and the surface-slope parameter  $\delta$ . The calculations also provide an opportunity for assessing the accuracy and effectiveness of a more general program applicable to non-N incident waveforms.

Prior to the examination of the solution details, brief remarks will be given on several notions used in classical descriptions of sea waves and swell, with which the choice of parameters  $k$  and  $\delta$  as well as the model's relevance may find their base. Also given along these remarks are notes on the overpressure and frequency ranges anticipated in the calculations which may be of relevance to baleen whale audibility studies.

### 4.1 Preliminary Remarks

#### *Sea Waves and Swell: Parameter $\delta$ and $k$*

Surface waves grow under wind over an ocean and form an irregularly looking surface pattern known as “sea”--paraphrasing from W.H. Munk (1956). When a wind-raised waves travel out of the storm area, they advance as “swell”, and having traveled large distances they become a series of long, low and fairly regular waves of *sinusoidal* undulation. The chaotic appearance of the sea surface may still be conceptualized as the result of superimposing a number of *sinusoidal wave trains* one on top of another, [see, for example, Bascom (1964)]. Munk (1956) used the notion of “cross sea” to dramatized that sea coming from different quarters of a storm system run in *different directions*, giving peaks and hollows when crests and troughs of these non-aligned wave trains meet. Correspondingly, alternate groups of

high and low waves observed in a regular swell may also be caused by interference of the non-aligned wave trains from different distant storms (and could be called “cross swell”).

Whereas, the wave length and wave height are affected by the length of stretch and duration, over and during which the wind blow, these studies indicate nevertheless that the wave height and wave length of fully developed sea and swell may be grossly estimated as a function of wind speed. With wind speeds of 15 and 20 knots, corresponding to the “moderate” and “fresh” breezes, for example, wave height and wave length of a fully-developed sea may be estimated from Table III in Bascom (1965, p. 53) together with the relation between wave length and wave period for deep water:

	Wave Height	Period	Wavelength
(a) 15 knots	1.5m	6 sec	56m
(b) 20 knots	3m	8 sec	100m

where the wave height was bases on the average of the highest 10%, and the wavelength was computed from the period using the deep-water formula. This provides a reference frame with which the relevance of the parameter sizes of  $\delta$  and  $k$  for the model analyses can be judged.

While the slope parameter  $\delta$  in most our model calculations are either 0.02 or 0.025, the surface-wave number  $k \equiv 2\pi/\lambda$  varies considerably in the range  $k = 4$ -16 for aircraft studies, and in the range  $k = 16$ -64 for space-launch ascent studies. The wide variations in  $k$  among the examples were made with the expectation of its significant effect on the wave interaction mechanism, surface-wave height and wavelength. In particular, the surface-wave train with  $\delta=0.02$ ,  $k=16$  for a signature gives a length of  $L'=100\text{m}$  and wavelength  $\lambda L'=40\text{m}$  and a wave height  $2\delta\lambda L'=2\text{m}$ , not very far from (a) above; the wave train with  $\delta=0.02$ ,  $k=64$  for a signature length  $L'=1\text{km}$  gives a wavelength  $\lambda L' = 98 \text{ m}$  and a wave height  $2\delta\lambda L'=4\text{m}$ , comparable to (b) above. The comparison can be brought closer by readjusting  $\delta$ ,  $k$ , and  $L'$ .

### *Underwater Infrasound; Audibility*

Except for  $M_A > 4.53$  under standard conditions, sonic boom noise becomes *infrasound* (frequency  $< 20\text{Hz}$ .) or nearly so, shortly after water entry. While the flat-ocean (Sawyers) model would predict a frequency far below a *unit* Hertz in deep water, the sound field generated by interaction with a wavy surface produces audible disturbances in the 1-40 Hz range, at levels in common with infrasonic tones emitted by ships, icebreakers, drilling platforms, and airguns (though widely differs in waveform and duration, Cf. Richardson et al 1995). Whereas, how many marine mammal species can *detect* infrasound is unknown, certain baleen whale species particularly the fin and blue whales, most likely do so (Richardson et al, Sec. 8.6). It is believed, with the exception of extremely shallow water (where the ambient sound-pressure noise level would exceed  $100\text{dB}$ )<sup>4</sup>, the underwater sound in question can be important to marine mammals, as other low-frequency man-made sounds. Apart from the need for a proper frequency range, the received sound-pressure level (at depth) must be high/strong enough to be audible/perceivable in the presence of ambient noise. Recent Studies [Potter (1994), Natural Resource Defense Council (1999)] on low-frequency sound impact on marine mammals have placed the  $120\text{dB}$  (re  $1 \mu\text{Pa}$ ) to be the *critical* level which is substantially higher than the  $80\text{dB}$  (re  $1 \mu\text{Pa} / \sqrt{\text{Hz}}$ ) maximum sound-pressure density spectrum level from ocean traffic noise in deep and shallow waters (Wenz 1962,

\* Note that  $1\text{dB (re } 1\mu\text{Pa}) = 1\text{dB (re } 20\mu\text{Pa}) + 26$ .

Urlick 1983)<sup>5</sup>. [This 120dB falls within the 116-126 dB (re 1μPa) range perceived by a power-mower operator (Kinsler et al 1982) or by a pilot/passenger inside the cockpit of a light aircraft, and is loud enough, indeed].

The final results in most of the examples studied below will be presented in the waveform in the time domain, that is, overpressure (psf) vs. time (sec.), where psf stands for pound per square foot. From the zero crossing in the waveform, the signal frequency as well as its up/down sweep property can be inferred. The 120 dB (re 1 μPa) level mentioned correspond to an overpressure

$$120 \text{ dB (re 1 } \mu\text{Pa)} = 1 \text{ pascal} = \text{Newton/m}^2 \approx 0.0209 \text{ psf.}$$

This dB scale will also be marked along with psf in several time-domain presentations to help comparisons. [Note that every 10-fold change in psf corresponds to a change in 20 units on the dB scale]. Finally, we note that the comparison of signals in dB (re 1μPa) with estimated ambient noise in dB [re 1 μPa /  $\sqrt{\text{Hz}}$ ] can not be appropriate for signal durations significantly longer than one second. The noise level must be multiplied (and raised) by the logarithm of the square root of the signal duration (the allowed exposure time) for the comparison/assessment study. For example, a 10-second pulse duration would raise the ambient noise level from 80 dB to 86 dB.

### Examples Studied

Most calculations presented below were made for the sinusoidal wave train

$$z' = \delta \lambda Z_w = -\delta \lambda e^{i(k_1'x' + k_2'y' - i\omega t)}$$

which differs from that in the original formulation of Part I by a *phase*  $e^{i\pi}$ . The same phase difference enters in the final results for the time-dependent part of the results, such as  $\hat{A}(\xi)$  and  $\delta P_2$ . Since the time and spatial origin of the surface-wave train is arbitrary, the difference in question cannot lead to any difference of physical relevance and is unessential. In the following Subsection 4.2, we study the case of an incident N wave with  $M_A = 1.82$ ,  $k = 4$ , and  $\Lambda = \Psi = 0$  in various stages of the solution process, and finally apply it to the specific example with  $p'_{\text{max}} = 2$  psf and  $\delta = 0.02$ . It illustrates the key stages through which the final numerical solution was obtained; the same solution process was used for other more extensive studies with wider variation in  $M_A$ ,  $k$  as well as other physical parameters. Prior to Subsection 4.4, an examination is made on the results of a numerical procedure applicable to *non-N* incident waveform (Subsection 4.3).

#### 4.2 Example of Solution Process: $M_A = 1.82$ , $k = 4$

This example corresponds to the 2-D interaction problem and is applicable to the wave field directly under the flight track ( $\Lambda = 0$ ) while the surface-wave vector aligns exactly with the flight direction ( $\Psi = 0$ )<sup>6</sup>. We shall examine in this case the adequacy of our results at various stages of the solution process, including certain methods of implementation and the use of the far-field (stationary-phase) formula.

<sup>5</sup> This comparison is meaningful provided the duration of the sound pulse does not far exceed one second. Note that  $1\text{dB}[\text{re } 1(\mu\text{Pa})^2 \text{ */Hz}]$  in sound-pressure density spectrum level is equivalent to 1 dB [re 1μPa /  $\sqrt{\text{Hz}}$ ] when expressed in the form of sound-pressure level.

<sup>6</sup> Results for this case were presented in one of our earlier study (Cheng & Lee 1998). While significant difference from the data set are not apparent, the older results did not satisfy the radiation condition in the far field correctly, apart from a number of uncorrected algebraic error in the computer code.

The first stage of the calculation is to compute the normalized forms of surface velocity potential  $\phi(x', 0)$  pertaining to the synchronous solution, using the convolution integral given in Sec. I.2 of Appendix I. Its real and imaginary parts are shown by the pair of graphs in Fig 4.a as functions of  $x'$ . The accuracy of the function  $\hat{A}(\xi; \bar{z})$  to be computed later is sensitive to the error of  $\phi$  at large  $x'$ ; a set of asymptotic expansions for large  $x'$  was developed to ascertain the solution accuracy and to reduce computation work (Cf. Appendix I, Sec. I.2). The good agreement between the large- $x'$  expansion and very-accurate numerical integration are seen in Fig. 4.a. With the  $x'$ -derivative of  $\phi(x', 0)$  and the analytic result for the boundary-value transfer term [Cf. (3.9), Appendix I, Sec. I.2], the spatial-dependent part of the synchronous solution of the surface pressure  $\hat{p}_2(x', 0)$  is obtained; its real and imaginary parts are shown in Fig. 4.b. For this and most other examples, the  $\hat{A}(\xi)$  was computed from the Fourier transform of  $\phi(x', 0)$ , together with an explicit, analytic form of the Fourier transform of the boundary-transfer correction. Note that leading and trailing edges of the overpressure of the incident N-wave are located at  $x' = 0$  and  $x' = 1$ , respectively.

The important function  $\hat{A}(\xi)$ , i.e. the Fourier transform of  $\hat{p}_2(x', 0)$ , may now be computed numerically [Cf. (3.12)] and the real and imaginary parts of results are presented in Fig. 5. The Fourier integral was computed by trapezoidal rule implemented with local treatment of the known singularities expected at  $\xi = \xi_{A1}, \xi_{A2}$  associated with the  $\phi(x', 0)$  at large  $x'$ . [The standard FFT procedure does not give adequate results in this case]. Our numerical procedure proves to be indeed very accurate—the two graphs in Fig. 5 are indistinguishable from the exact, analytic results for the N-wave from Part I (in filled circles).

The underwater solution to  $\hat{p}_2(x', \bar{z})$  is obtained from the inverse Fourier transform of the product  $\hat{A}(\xi)\sigma(\xi; \bar{z})$  for a specified  $\bar{z}$ , (3.14). The distribution of real and imaginary parts of  $\hat{p}_2$  at two different depth levels  $z = 0.5$  and  $z = 2.5$  are shown in Fig. 6 and Fig. 7. In Fig. 6 for  $z = 0.5$ , where the depth is only a *half* of the signature length  $L'$ , the far-field formula (light dashes) works surprisingly well over the whole  $x'$ -range except near  $x'=0$ , where the formula still provides the right behavior and order of magnitude. The light dashes computed from the far-field formula, (3.16), is seen from Fig. 7 to closely capture the oscillatory features calculated by the intensive numerical integration (solid curve) at a depth level which is two and a half of the signature length  $L'(z=2.5)$ .

To see how these results from the wavy-ocean model can be meaningfully compared with one based on the Sawyers' model, we must assign values to the slope parameter  $\delta$ , signature length  $L'$ , and to a reference surface overpressure. For the present purpose, we only need to assume  $\delta=0.02$ , and will present the results in terms of a normalized overpressure and the normalized time. Three graphs comparing the overpressure waveforms (in the time domain) predicted by the flat-ocean model (dashes), the time-dependent part of the wavy-ocean model (dash dots) the sum (total) of the two (solid curve) are presented in Figs. 8, 9, and 10, for the three depth levels  $z=0, 0.5$ , and  $2.5$ , respectively. As is apparent from Fig. 8, the time is normalized by the transit-time  $L'/U$  and the reference overpressure is so chosen that the normalized maximum surface pressure equals to 2. The persistent ringing feature is the response of the supersonic wave field above water to the sinusoidal surface-wave train and is clearly a *secondary* effect in the presence of the towering N-wave signature over the segment  $0 < x < 1$ .<sup>7</sup> In Fig. 9 where the overpressure waveform at depth level of one-half the signature length ( $z=0.50$ ) is presented, the wavy-surface effect begins to markedly alter the otherwise smoothly degenerated N-wave profile (in dashes); the peak over/under-pressure is seen to increase by nearly 45%. At  $z=2.5$ , Fig. 10 shows that even at this moderate depth level the expected dominance of the surface-wave interaction effect is fully realized. Here, the persistent ringing feature next to the surface transform itself into a *packet of wavelets* (dash-dot

<sup>7</sup> Note that the overpressure waveforms in Figs. 8-10, are plotted as negative  $p'$  vs. the normalized time.

and solid curves) and overwhelms the otherwise primary (Sawyers) wave-field (in dashes). The waveform indicates a (slow) frequency downshift/sweep in the course of its passage, in accord with Doppler's principle. We note, in passing, that, this graph could be applied directly to an example with a 2 psf maximum surface overpressure. In this case, the peak overpressure would reach 0.06 psf at  $z=2.5$  well above the 120 dB (re 1  $\mu$ Pa) or 1 Pascal mark mentioned earlier.

### 4.3 Test of a General Computer Code: $M_A=1.5, k=4$

Results obtained for most our earlier studies were obtained by a computer program made strictly for incident N-waves. Usefulness of the program for space-launch applications requires consideration of non-N waveforms, for which a program is developed. There are four stages in the solution process, at which the results obtained are critical, namely, the surface velocity potential  $\phi(x', 0)$ , the contribution from the boundary-value transfer or its Fournier transform  $FT(\Delta P_{BT})$ , the Fourier transform of  $\hat{p}_2(x', 0)$ , i.e. the  $\hat{A}(\xi)$ , and finally the  $\hat{p}_2(x', \bar{z})$  at depth  $\bar{z}$  underwater. Adequacy of this more general program in generating the surface velocity potential and the boundary-transfer term were of concern in view of the anticipated solution singularities. Detail comparison with the N-wave results in these four stages provides a crucial test for the general program. The unquestionable agreement in the comparison is evident from Figs. 11-13 made for the case  $M_A=1.5, k=4$ . The comparison for the normalized  $\hat{p}_2(x', \bar{z})$  in Fig. 13 was made at the depth  $z=2.5$  corresponding to  $\bar{z} = \beta_w z = 2.36$  in this case.

### 4.4 Underwater Waveform Properties: $M_A$ and $k$ Dependence

The wave interaction effects analyzed are seen to depend linearly on the slope parameter  $\delta$ , but are more critically (and nonlinearly) dependent on the surface wave number  $k$  and Mach number  $M_A$ . These dependencies have been studied for wide ranges of  $M_A$  and  $k$ . The results for  $M_A=1.5, 1.88, 2.38$ , and  $k=4, 16$  are shown and examined below.

#### *$\hat{A}(\xi)$ : Fourier Transform of Surface Overpressure*

The real and imaginary parts of the important function  $\hat{A}(\xi)$  are shown for the four  $(M_A, k)$  combinations, namely (1.5, 4), (1.5, 16), (1.88, 16), and (2.38, 16). Note the  $k = 2\pi/\lambda = 16$  gives  $\lambda=0.39$  and corresponds to a surface wavelength nearly 40% of the sonic-boom signature length  $L'$ . The  $\hat{A}(\xi)$  function shown in Figs. 14-16 is fundamentally important in that it is, in essence, the equivalence of the (time-dependent) acoustic-source distribution generated by the wave interaction that will control the wave-packet envelope in the deeper part of the water. These  $\hat{A}(\xi)$  functions were computed from the exact, analytic formulas derived in Part I for incident N-waves, reproduced in Appendix II.1. The symbols  $\xi_{A1}$  and  $\xi_{A2}$  in the figures, mark the  $\xi$ -value of the two square-root singularities. As noted earlier, these and other singularities lie completely outside the range  $\xi_1 < \xi < \xi_2$  through which  $\hat{A}(\xi)$  exerts its control in the far field ( $k \bar{z} \gg 1$ ). These singularities must, nevertheless, be properly treated in numerical calculation at locations which are not so deep ( $k \bar{z} = 0(1)$ ). Of interest are the several  $\xi$ -values where  $\hat{A}(\xi)$  vanishes; these zero-crossings will be found along the certain rays of constant  $\eta = x'/\bar{z}$  in the far field, along which the time-dependent pressure field must altogether vanish.

#### *Signal Duration and Ambient Ocean Noise*

In an attempt to make the results more pertinent, we have assumed in the calculations a signature length  $L'=300$ ft. and the surface-wave slope parameter  $\delta=0.025$ . This allows the description of sound-pressure waveform in units of psf and second. As seen below, the sound-pressure of interest are found to



be well above 0.002 psf corresponding to the 100 dB (re 1 $\mu$ Pa) level over a signature duration 4-6 seconds. From the viewpoint of signal's audibility, this observation is helpful in that the maximum sound-pressure level (averaged over one second) of the ambient noise in deep as well as shallow water are contributed primarily by ocean traffic, and were estimated by Wenz (1962) and Urlick (1983) to be 80 dB (re 1  $\mu$ Pa/ $\sqrt{\text{Hz}}$ ); its resulting effect on the perceived signal should remain well below the 100 dB (re 1  $\mu$ Pa) mark, as long as the signal duration does not exceed 100 seconds.<sup>8</sup>

### *Comparison with Flat-Ocean Model*

The results obtained for the deep water ( $z=1500\text{ft.}$ ) presented in the lower parts of Figs. 17a, 17b, 18, and 19 shows unquestionably the dominance of the surface-wave train effect over the corresponding signals of the flat-ocean model. Even at a depth level as close to the surface as  $z=150\text{ft.}$ , apart from the distinct ringing feature absent from the flat-ocean analysis, a peak overpressures 40% higher than Sawyer's prediction are found in all cases studied.

### *Effects of Surface-Wave Number Change*

The effects of increasing  $k$  can be studied with Fig. 17a for  $k=4$ ,  $M_A=1.5$ , and Fig. 17b for  $k=16$ ,  $M_A=1.5$ , where results computed for the small and large depth levels ( $z=150\text{ft.}$ ,  $1500\text{ft.}$ ) are presented. Here, the noticeable reduction in overpressure with the four-fold increase in  $k$  is evident upon comparing the results for  $k=4$  in Fig. 17a with those for  $k=16$  in Fig. 17b; the results are in accord with the  $1/\sqrt{kz}$  rule from the theory noted earlier. Similar comparisons with same conclusion have been made for  $M_A=1.88$  and  $M_A=2.38$  and will not be repeated here.

The instantaneous frequency pertaining to the individual carrier wave (wavelet) of the wave packet is obviously controlled by the surface wave number  $k$ . Increasing  $k$  is expected to cause the wave packet more densely packed. Counting the "zero-crossing" of the waveform and dividing it by the period covered in each case indicates that at least for  $M_A=1.5$ , the average wavelet frequency is not far from the value of  $k$  (with the exception of  $k=16$  at  $z=150\text{ft.}$ ). However, at the higher Mach numbers, the number of zero-crossings will be seen to increase much more rapidly with  $k$ .

### *Mach-number Influence on Wave-field Characteristics*

- (i) Overpressure peak. The wave-packet features are made more distinct by increasing the Mach number  $M_A$ . The peak overpressure in the large depth level ( $z=1500\text{ft.}$ ) is seen from Fig. 17b, Fig. 18, and Fig. 19 to increase successively from 0.035 through 0.05 to 0.09 psf, as  $M_A$  increases from 1.5 through 1.88 to 2.35. A lesser peak increase trend with Mach number is also seen from Fig. 17b, Fig. 18, and Fig. 19 at the smaller depth level ( $z=150\text{ft.}$ ), with the peak overpressure reaching 0.25, 0.30, and 0.35 psf for  $M_A=1.5$ , 1.88, and 2.38, respectively.
- (ii) Carrier-wave frequency. The number of wavelets seen earlier in the waveforms at  $M_A=1.5$  are now seen to give a more densely packed waveform at the higher Mach number,  $M_A=1.88$  and 2.38 (Cf. Figs. 18, 19); here the time intervals between neighboring wavelets are made even smaller; therefore, the frequencies of these wavelets – the carrier-wave frequencies – become much higher. Counting the number of peaks in the waveform (or the half of the zero-crossing number) within a given interval should give a fair estimate of the *carrier-wave*

<sup>8</sup> For a duration of 100 sec the sound-pressure noise level in this case would accordingly be 100 dB (re 1 $\mu$ Pa).

*frequency*. Since the wave form in the forward part is more densely packed than in the real, the estimates must be made for the forward and real parts separately. Applying the counting to the forward and real portions of the waveform at depth level  $z=1500\text{ft.}$  yields two sets of frequency estimates:

$M_A$	1.5	1.88	2.38
$t < 0$	19 Hz	26 Hz	43 Hz
$t > 0$	14 Hz	19 Hz	24 Hz

Similar estimates with slightly less values are found with waveforms at the small depth levels ( $z=150\text{ft.}$ ). The frequency downshift/sweep shown is expected from the Doppler principle.<sup>9</sup> This (carrier) frequency variation, however, indicates a (time-wise) building-up process of the acoustic power spectrum, namely, as the sound sources pass by, only a portion of the spectrum near the higher frequency end will first be built up; the remainders of the spectrum in the mid and lower frequency end are completed later (in time). The deep-water wave field dictates that frequency range of this spectrum be limited to the interval  $[\xi_1, \xi_2]$  of (3.16e) noted earlier in Section 3. These frequency downshifts in the waveform (observed in the rest frame) signifies that, forward, backward (as well as downward) propagating waves will be observed in a frame moving with the sonic-boom waves, as demanded by an acoustics model satisfying the correct radiation condition in the deepwater far field.

In passing, we note that as these carrier waves spread and move away, the propagation speed observed in the moving frame (identified with that of the crests and troughs) is shown (in Part I) to be none but the *group* velocity.

#### 4.5 Non-aligned Wave Trains

For surface-wave trains not aligned with the flight track and/or at span stations not directly under the flight track (cf. Fig. 3), the solution procedure remains the same except the constants  $P$ ,  $Q$ ,  $\Omega$  etc. must be evaluated by the chosen values of  $\Lambda$ ,  $\Psi$ ,  $M_A$ , and  $k$  in accordance with Appendix I, Section I.1. [Also refer (3.16a, b)] As observed earlier, the significant effect of the surface-wave interaction can be found only inside the  $M_{nw}^2$  and  $(\Lambda + \Psi)$  domain [Cf. Fig. 3 and (3.15a, b)]. To see how the underwater wave field within this domain holds up for non-vanishing  $\Lambda$  and/or  $\Psi$  is the main objective for a study comparing solutions for various combination of  $\Lambda$  and  $\Psi$ . Several examples in ranges of  $|\Lambda| < 30^\circ$ ,  $|\Psi| < 30^\circ$  are examined below for a fixed Mach number  $M_A = 2.38$ .

In as much as the effects of  $\Lambda$  and  $\Psi$  on the overpressure in deep water are the main concern, only function  $\hat{P}_2$  needs to be considered; comparison of its value with the corresponding value obtained earlier for  $\Lambda = \Psi = 0$  will suffice to indicate the degree of significance in question. As will be seen below, while the waveforms can be noticeably altered, the magnitude of the peak overpressure and the general characteristics of the wave-packet are not significantly changed from those with  $\Lambda = \Psi = 0$  studied earlier. Figures 20 and 21 compare results of  $\phi(x', 0)$  and  $\hat{A}(\xi)$  in four  $(\Lambda, \Psi)$  combinations

$$(\Lambda, \Psi) = (0,0), (-15,0), (0,15), (-15, 15),$$

<sup>9</sup> Frequency down-sweep is commonly reported in works on whale calls (D'Spain et al 1995, Cumming & Thompson 1971, Edds 1988)

with the Mach number and surface wave number fixed at  $M_A=2.38$  and  $k=16$ . The corresponding waveforms in  $\hat{p}_2$  are shown for the depth level  $z=2.5$  in Fig. 22.<sup>10</sup> The wave-packet structure for  $(\Lambda, \Psi) = (-15, 0)$  in Fig. 22 appears to depart more significantly from that for  $(\Lambda, \Psi) = (0, 0)$ . It was uncertain that the far-field formula for large  $kz$  could still remain useful at the station  $\Lambda=-15^\circ$  in this case. Figure 23 compares the prediction by far-field formula for  $\hat{p}_2$  with the numerical calculation for  $(\Lambda, \Psi) = (-15^\circ, 0)$  at  $z=2.5$ ; the highly varying wavelet structure (in both amplitude and frequency) in the range  $|x'| < 3$  does not compare as well as for  $\Lambda=\Psi=0$ . Whereas, detail agreement is found over the wider range  $|x'| > 3$ .

Wider non-aligned surface-wave angles are considered in Figs. 24-26, in which results from three  $(\Lambda, \Psi)$  combinations are compared for

$$(\Lambda, \Psi) = (0, 0), (0, 30^\circ), (-30^\circ, 30^\circ)$$

are compared again with  $M_A=2.38$  and  $k=16$ . For these three cases, the waveform in the time domain were also computed for  $\delta=0.025$  and shown in Figs. 26.Xa,b,c. Conclusions on the peak overpressures and characteristic features of waveforms and their dependence on  $\Lambda$  and  $\Psi$  are again similar to those on the preceding figures. From these examinations, the peak overpressure and waveform characteristics are seen not being significantly different from the aligned case  $\Lambda=\Psi=0$ .

The final results for the time-domain overpressure waveforms are obtained for each of the three combinations of  $(\Lambda, \Psi)$ , shown and compared in Figs. 26Xa,b,c for the same depth level  $z=2.5$ , assuming  $M_A=2.38$ ,  $k=16$ .

#### 4.6 Multiple Trains Interference: “Cross Sea”

The solution procedure for the nonaligned surface-wave train ( $\Psi \neq 0$ ) can be adopted to study underwater wave field for a sea surface resulting from a combination of an arbitrary number of horizontal wave trains, each with its own wave height  $2\delta_n \lambda_n$ , wave number  $k_n = 2\pi/\lambda_n$ , and non-alignment angle  $\Psi_n$ :

$$z = Z_w(x, y) = \sum \delta_n \lambda_n e^{-i(k_n x + k_{2n} y - \omega_n t)} \quad (4.2)$$

At a given Mach number  $M_A$  and a span station identified by the swept angle  $\Lambda$ , the solution to the normalized overpressure underwater is the real part of

$$p' = p_1(x', \bar{z}; y') + \sum_{n=1} \delta_n \hat{p}_{2n}(x', \bar{z}; y') e^{-i\Omega_n t} \quad (4.3)$$

The mode superposition in (4.2), (4.3) are expected to give rise to interference patterns in the surface-wave topography and the corresponding underwater wave field. Chaotic-like waveforms could be generated with two or three trains, depending on  $k_n, \Psi_n$ , and  $\delta_n$ , aptly called “cross sea” (Munk 1956) in such case. In the following, three cases will be examined directly under the flight track  $\Lambda=0$ : (i) A

<sup>10</sup> Recall that to obtain the complete time-domain waveform, one must multiply  $\hat{p}_2$  with  $\delta \exp[i(k'_2 y - \Omega t)]$ , and covert  $x'/L'$  to  $Ut/L'$ . In application, the product must also be rescaled with the reference overpressure at the surface, which subject to change from station to station by the factor  $\cos^2 \Lambda$ .

combination of two surface trains which are well aligned with the flight track ( $\Lambda = \Psi = 0$ ), but have wave lengths rather close to each other ( $k=3.8, 4.0$ ); (ii) A combination of two *obliquely crossing* trains, one with  $(\Lambda, \Psi) = (0, 0)$  and the other with  $(\Lambda, \Psi) = (0, 30^\circ)$ ; (iii) A particular case involving two crossing surface trains with equal and opposite alignment angles, such as  $(\Lambda, \Psi) = (0, 30^\circ)$  and  $(0, -30^\circ)$ . Except for  $k=3.8$ , the function  $\hat{p}(x', \bar{z})$  of the synchronous wave field have been computed and shown earlier.

#### *Two Aligned Wave Trains: $\Lambda = \Psi = 0, k=3.8, 4.0$*

Figures 27 a, b, c, d present results of interaction of an incident N-wave with wavy surface made up of two sinusoidal trains which are aligned with the flight track ( $\Lambda = \Psi = 0$ ) and have rather close wave numbers  $k=4$  and  $3.8$ . The example in Fig. 27 a shows the surface depression  $Z_w$  in ft. as function of time in sec., resulting from the sum of the two sinusoidal shapes, assuming  $\delta=0.025$  and  $L'=300\text{ft.}$ . The wave field underwater generated from the wavy-surface interaction can be computed as the *sum* of two *synchronous* solutions, one for  $k=4.0$  and the other for  $k=3.8$ . The overpressure waveform at  $z=5$   $L'=1500\text{ft}$  for  $k=4.0$  and  $k=3.8$  are shown in Fig. 27b and Fig. 27c, respectively. Apart being almost indistinguishable, the envelope of these two waveforms possess a strong fore and aft symmetry. This symmetry is completely destroyed, however, in Fig. 27d as a result of their combination.

#### *Example of Obliquely Crossing Trains*

We consider the wavy surface directly under the flight track ( $\Lambda=0$ ) made up of an aligned ( $\Psi=0$ ) and a non-aligned ( $\Psi=30^\circ$ ) trains. For simplicity, we assume  $k=16$ ,  $\delta=0.02$  for both trains. The result can be generated with the  $\hat{p}_2$  solutions presented earlier in Figs. 26.Xa,b,c with  $(\Lambda, \Psi) = (0,0)$  and  $(0,30^\circ)$  for  $M_A=2.38$  and  $k=16$  at  $z=2.5$ . The sum of the two yields the  $\hat{p}_2$  waveform of interest and the result in total overpressure ( $p'_1 + p'_2$ ) is shown in Fig. 28a.<sup>11</sup> Evidently seen are the amplified overpressure peaks and the asymmetrical features in the waveform envelope caused by the mutual interference of the two crossing surface trains.

#### *Example of the Special Case: $(0, \Psi)$ & $(0, -\Psi)$*

The very special case, in which the obliquely cross wave trains are set at equal but opposite angles with the flight track, may serve to illustrate the interference effect without much additional effort. Since the entire water column under the flight track is now a *symmetry plane*, the overpressure distribution perceived at any point (any  $\bar{z} > 0$ ) therein is none other than *twice* the waveform value of the  $p'_2$  obtained from  $p'_2$  for  $(\Lambda, \Psi) = (0, 30^\circ)$  shown earlier in Fig. 26Xb, provided we take  $M_A=2.38$  as was in Fig. 26Xb, and the same  $\delta$  in both trains. The result is shown in Fig. 28b for  $\delta=0.025$ . On the other hand, were the  $\delta$ 's of the trains opposite in sign, or the  $Z_w$ 's differing by  $\pm 180^\circ$  (or its odd integral multiple),  $p'_2$  would *vanish* and no wave could be found in the symmetry plane other than that in Sawyers' theory. To be sure, the  $\delta$  can be complex; the event with the doubling effect presented in Fig. 28b and the occurrence of  $p'_2 \equiv 0$  in the symmetry plane cannot happen unless  $\delta = \pm 1$ .

### **4.7 Departure from Sinusoidal Surface Waves**

The study of sonic boom interaction with sinusoidal surface waves may be extended to treat the interaction problems for two kinds of water waves, namely, the Stokesian waves (Stokes 1847; Yih 1977, pp.206-308) and the "deepwater solitary waves" (Yuen & Lake 1980, Redekopp 1980). The former

<sup>11</sup> The results presented in Figs. 28a and 28b for  $p_2$  were based on the peaks and valleys read from the graphs of Figs. 26Xa and 26Xb, and may suffice for illustrating the nature under a cross sea.

represents a correction to the sinusoidal wave train for weak nonlinearity and the latter is also a periodic wave train with slowly varying amplitude of which the envelope takes on a solitary-wave like shape. Applications to the problem involving the solitary-wave like wave train will be the subject of a subsequent study. In the following we shall examine the nonlinear corrections to surface waves and to the underwater wave field based on the Stokesian approach. Numerical example underwater will not be presented below, since the nonlinear effect as well as the instability growth rate for the range of  $\delta$  of interest is too small.

The Stokes expansion for the surface elevation to the third order in  $(2\pi\delta)$  is (Yih 1977, pp. 201-203)

$$Z_w/\delta\lambda = \cos kx + [\pi\delta + \frac{17}{24}(2\pi\delta)^2] \cos 2kx + \frac{3}{8}(2\pi\delta)^2 \cos 3kx + \frac{1}{3}(2\pi\delta)^3 \cos 4kx + \dots \quad (4.4)$$

This is a Fourier series representation of a *periodic wave train* with a fundamental period  $2\pi/k$ , of which the underwater acoustic field is amenable to treatment noted in Section 3.4 and the underlying theory detailed in Appendix IV. The series affords the inference of the maximum amplitude occurring at the highest points of the free surface, which are the vertices of angles  $120^\circ$ . Many terms have since been added and corrected (see Van Dykes 1975, p. 216). Schwartz (1974) extended the series to 117 orders, and, after a slight modification of the expansion parameter, was able to calculate the maximum height to five figures. Owing to the nonlinearity, it may not be possible to infer from the series (4.4) or its extension the precise ratio of the wave-height to wave-length; Bascom (1964) gave an empirical value of the ratio for swells occurring in real ocean to be 1:7; whether it comes close to that from Schwartz's (1974) calculation is unclear. At this ratio and beyond white caps and spays ensure. Using  $2\delta\lambda$  of the sinusoidal train to indicate the wave height, Bascom's 1/7 criterion for the vertices formation calls for  $\delta = 1/14 = 0.071$ . Using the maximum slope of sinusoidal surface  $2\pi\delta$  as the maximum slope at the vertices, (with the  $120^\circ$  including vertices angle) the  $\delta$  would be subject to the requirement  $\delta \leq \tan 30^\circ/2\pi \approx 0.092$ . The range of  $\delta=0.01-0.025$  considered in our numerical study is well below these estimates. Figs. 29 a, b, c show the difference in surface depression  $Z_w$  of the Stokesian wave and the corresponding sinusoidal wave with  $k=4$  for  $\delta=0.025, 0.05$  and  $0.10$ .

Even before their disintegration, instability of periodic wave trains can grow on account of nonlinearity (Benjamin & Feir 1967). The growth rate of the instability, in terms of the imaginary part of the frequency of the stability theory,  $\omega_i$ , may be shown to be comparable to the square of the product of  $k$  and the half wave height (Yuen & Lake 1980, Redekopp 1980)

$$\omega_i = O[(2\pi\delta)^2] \quad (4.5)$$

being small and comparable to 0.016 for  $\delta=0.02$ , and to 0.025 for  $\delta=0.025$ . In this sense, instability growth of the sinusoidal surface train may be considered quite insignificant.

#### 4.8 Sonic Boom over Shallow Water

The theory of Part I and the foregoing studies do not allow the presence of a sea floor. The potential sonic-boom impact is expected to be much more severe in the shallow coastal water than in the deep open sea. Here, the descriptions "deep" and "shallow" refer to the ratio of ocean depth to the (sea-level) sonic-boom signature length,  $h/L'$ , being much larger and smaller than unity, respectively. The

theory extension to shallow water can be readily made, and lends itself to a study of the sediment-boundary waves. Occurrence of the latter phenomenon depends critically on the sediment shear-wave speed,  $C_s$ , which can be very low near the interface of certain sediments. There have been considerably different opinions with regards to the vanishing magnitude of  $C_s$  next to the sediment interface and its importance (Stoll 1989; Hamilton 1971; Badiéy et al 1996,1998; Clay & Medwin 1977; Chapman & Godin 1999). In the following we shall examine examples with the simplest sediment model to illustrate the potential of sediment wave excitation by sonic boom, proposed originally in Desharnais and Champman's (1998) paper.

### *Flat-Ocean Bottom Effect*

The sea-floor effect on the wave field below a non-wavy ocean under sonic boom can be studied as an extension of Sawyers' theory. For  $M_A < 4.53$  (under standard conditions), the elliptic problem was solved in Cheng & Lee (1998) paper through conformal mapping to a half-plane. As an example for demonstrating the bottom effect and the relative insensitivity of the wave field to the bottom's presence with the exception for its *vicinity* (and unless  $h/L' = 1/2$ ), we consider a model of an *open* channel (with a flat, free surface) and a variable/adjustable (channel) depth  $h$ . We would like to predict the sonic boom generated overpressure distributions at a *fixed* distance below the water surface, which is taken to be one half of the signature length,  $z = L'/2$ , while the channel depths changes successively from  $h=8$  to  $h=L'/2$ . The result of the calculations made for an incident N wave at  $M_A = 1.5$  are shown in Fig. 30 together with a sketch identifying  $h, L'$  and the coordinates, where the (negative of twice of the) overpressure ratio

$$-2 p' / p'_{\max}$$

observed in a frame moving with the sonic-boom wave is plotted as functions of  $x/L'$  for five channel depths in the range  $0.5 < h/L' < 8$ . The explicit integral form of the solution for  $u' = -p'/\rho U$  is also reproduced in Fig. 30.

Of interest in these plots is the relatively small departure from the Sawyers' waveform (for infinite  $h/L'$ ) as the floor is raised, i.e., as the channel depth reduces, until the fixed (monitoring) station/level  $z' = L'/2$  is reached, where an 80% peak-value increase is found on the sea floor. Note that for  $h/L' = 1$ , the monitoring station is, exactly at the half channel depth where the difference from Sawyers' result is no more than 5%. Accordingly, bottom effect may not appear to significantly affect the overpressure field under a flat ocean, except next to the sea floor and unless the open channel becoming shallower than  $h/L' = 0.5$ .

The markedly amplified signal next to the bottom is nevertheless a significant feature to be recognized, concerning effects on the sea floor environment. The likelihood and issues of exciting sediment boundary waves by sonic booms over shallow coastal water will next be briefly examined.

### *Sediment-Boundary Waves Under a Shallow Sea*

#### The 2-D model

To allow interaction of an elastic, solid bottom wall with a hydro-acoustic medium, a 2-D shallow-ocean model is assumed which satisfies the continuity condition in the normal velocity, normal

stress and shear stress across the interface. For this model three potential functions will be considered. Namely, in addition to the  $\phi$  for the water, a scalar potential  $\Phi$  and a component of the vector potential  $\Psi$  for the sediment median, will be simultaneously solved. Each of these potentials satisfies their respective acoustics equations pertaining to the three characteristic propagation speed of the media  $C_1, C_p$ , and  $C_s$  with the subscripts “1” referring to the water, “p” and “s” referring to the compressive waves and the shear waves of the elastic medium, respectively. (See, for example, Tolstoy & Clay 1966, 1987). In the elastic medium, the normal stress and shear stress (on the x-y plane) are

$$\sigma_{zz} = \lambda \left( \frac{\partial^2}{\partial x^2} + \frac{\partial^2}{\partial z^2} \right) \Phi + 2\mu \left( \frac{\partial^2}{\partial z^2} \Phi + \frac{\partial^2 \Psi}{\partial x \partial z} \right) \quad (4.6a)$$

$$\sigma_{zx} = \mu \left[ \left( \frac{\partial^2}{\partial x^2} - \frac{\partial^2}{\partial z^2} \right) \Psi + 2 \frac{\partial^2}{\partial x \partial z} \Phi \right] \quad (4.6b)$$

where  $\lambda$  and  $\mu$  can be related to  $C_p$ ,  $C_s$ , and density  $\rho$  as

$$C_p^2 = \frac{\lambda + 2\mu}{\rho}, \quad C_s^2 = \frac{\mu}{\rho} \quad (4.7a,b)$$

The three compatibility conditions across the interface at  $z=0$  give, in the rest frame, are

$$\frac{\partial \Phi_1}{\partial z} = \frac{\partial \Phi_2}{\partial z} + \frac{\partial \Psi_2}{\partial x} \quad (4.8a)$$

$$\rho_1 \frac{\partial^2}{\partial t^2} \Phi_1 + \lambda_2 \nabla^2 \Phi_2 + 2\mu_2 \left( \frac{\partial^2}{\partial z^2} \Phi_2 + \frac{\partial^2 \Psi_2}{\partial x \partial z} \right) \quad (4.8b)$$

$$0 = \frac{\mu_2}{\rho_2} \left[ \left( \frac{\partial^2}{\partial x^2} - \frac{\partial^2}{\partial z^2} \right) \Psi_2 + 2 \frac{\partial^2}{\partial x \partial z} \Phi_2 \right] \quad (4.8c)$$

where the subscripts “1” and “2” refer to the water and the elastic media, respectively.

### Wave-train mode

For an infinitely extended elastic medium in half space, the three conditions at the water-solid interface at  $z=0$ , and the prescribed overpressure at the air-water interface  $z=-h$  together with a radiation condition or evanescent behavior at  $z \rightarrow \infty$  (cf. sketches in Figs. 31-33), will suffice for the determination of a synchronous solution in the wave train form:

$$\begin{pmatrix} \Phi_1 \\ \Phi_2 \\ \Psi_2 \end{pmatrix} = \begin{pmatrix} \hat{\Phi}_1 \\ \hat{\Phi}_2 \\ \hat{\Psi}_1 \end{pmatrix} \cdot e^{i(\alpha x - \omega t)} \quad (4.9)$$

This equation system, with the implicit assumption of the two homogeneous media, is no more or less than that for a homogeneous wave guide with an elastic wall modeling ocean's sedimentary layer (Tolstoy & Clay 1966, 1987, pp.134-134), and is in common with the mathematical models of submarine earthquake (Press et al 1950), mud slides (Ewing et al 1952) and large underwater explosion (Milne 1959). The depth of the water layer/channel  $h$ , or its product with the wave train wave number,  $\alpha h$ , is an important parameter that distinguishes the system from the Stoneley wave [recoverable from the limit of an unbounded  $\alpha h \rightarrow \infty$ ], and from the Rayleigh wave corresponding a vanishing water layer [recovered in the limit of a vanishing  $\alpha h \rightarrow 0$ ].

Of interest is the free propagation mode, susceptible to excitation. Unlike wave guide studies concerning mainly with signal transmission along the wave guide (in the  $x$ -direction), our interest is how a traveling acoustic source, such as the sonic-boom wave field over water surface, may excite and maintain a sediment boundary wave. In Desharnis and Chapman's model (1998), a more realistic multi-layer model representing variable  $C_p$  and  $C_s$  was employed. Whereas, the homogeneous elastic model adopted here offers greater simplicity in the analysis and perhaps more clarity in the results. Apart from a less ambiguous solution, the following study takes into account the finite-water depth effect on the multimedia-interaction, not accounted for completely in Desharnis and Chapman's (1998) analysis.

In the following analysis, we consider an N-wave incident upon the flat, shallow-ocean with the foregoing sediment model. Much details in the problem formation and solution procedures are in common with existing analyses of elastic-wall wave guide (Tolstoy & Clay 1966, 1987) and will not be detailed here. The analysis is made in the moving frame at the uniform horizontal velocity  $U$ , same as that of the sonic boom wave field. In this frame, (4.8a, b, c) is unchanged, except  $\partial^2/\partial t^2$  is replaced by

$$\frac{\partial^2}{\partial t^2} + 2U \frac{\partial^2}{\partial x \partial t} + U^2 \frac{\partial^2}{\partial x^2}$$

and the  $(\alpha x - \omega t)$  in (4.9) is changed to  $(\alpha x - \Omega t)$  with  $\Omega = U\alpha + \omega$ . The velocity of the reference frame  $U$  is chosen to coincide with the phase velocity  $-\omega/\alpha$  so that the complex exponential factor in (4.9) become time-independent.

#### The subsonic wave-train mode

The system underwater admits solutions with evanescent behavior, with the sediment interface chosen to be at  $z=0$ :

$$\hat{\phi}_1 = A_1 e^{|\beta_1 \alpha| z} + A_2 e^{-|\beta_1 \alpha| z} \quad (4.10a)$$

$$\hat{\phi}_p = B e^{-|\beta_p \alpha| z}, \quad \hat{\phi}_s = C e^{-|\beta_s \alpha| z} \quad (4.10b, c)$$

for *real* value of

$$\beta_1 = \sqrt{1 - M_1^2}, \quad \beta_p = \sqrt{1 - M_p^2}, \quad \beta_s = \sqrt{1 - M_s^2} \quad (4.10d)$$



i.e. for  $M_1 \equiv U/C_1 < 1$ ,  $M_p \equiv U/C_p < 1$ ,  $M_s \equiv U/C_s < 1$ . It also admits effervescent (radiating-wave) behavior like  $e^{i|\beta|\alpha z}$  if any of the  $\beta$  becomes imaginary if  $M > 1$ .<sup>12</sup> From the interface boundary conditions at  $z=0$  at  $z=-h$ , linear relations among the four constants  $A_1$ ,  $A_2$ ,  $B$ , and  $C$ , can be obtained. After eliminating  $A_2$  and  $C'$ , one arrives at

$$\left| \frac{\beta_p}{\beta_1} \right| \left( 1 - \frac{2}{2 - M_s^2} \right) \cdot B + D_{BW} \cdot A_1 = 0 \quad (4.11a)$$

$$\left[ 1 + e^{-2|\beta_1\alpha|h} + D_{BW} \right] \cdot A_1 = \frac{\hat{P}_0}{\rho_1 U^2 \alpha^2} e^{-|\beta_1\alpha|h} \quad (4.11b)$$

where

$$D_{BW} \equiv \frac{2}{1 + \frac{\beta_1}{\beta_p} \frac{\rho_2}{\rho_1} M_s^{-4} \left[ 4\beta_s \beta_p - 2(2 - M_s^2)^2 \right]} \quad (4.11c)$$

Note that the surface overpressure prescribed over the (flat) water surface has been assumed, up to this stage, to be a sinusoidal one

$$p'(x, 0; \alpha) = \rho_1 U^2 \alpha^2 \cdot \hat{P} e^{i\alpha x} \quad (4.12)$$

#### Free mode existence condition

The condition for the free mode (with propagation velocity  $U$ ) is seen from (4.11b) as

$$1 + e^{-|\beta_1\alpha|h} + D_{BW} = 0, \quad (4.13a)$$

that is,

$$-(2 - M_s^2)^2 + 4\sqrt{1 - M_s^2} \sqrt{1 - M_p^2} = \left( \frac{\rho_1}{\rho_2} \right) M^4 \frac{\sqrt{1 - M_p^2}}{\sqrt{1 - M_1^2}} \tanh(|\beta_1\alpha|h) \quad (4.13b)$$

identifiable with the free mode condition for the homogeneous shallow-water wave guide with an elastic solid floor (Tolstoy & Clay 1966, 1987, p. 135); it reduces to that of the Stoneley wave for an unbounded  $h$ , and to that of the Rayleigh wave in limit of a vanishing  $h$ . With a finite, non-vanishing  $h$ , the wave speed  $U$  (through  $M_1$ ,  $M_p$ , and  $M_s$ ) is now a function of the wave number  $\alpha$ , hence, unlike the Stoneley and Rayleigh waves, this interface wave is dispersive. The above condition indicates a permissible range  $U$  (or  $M_A$ ) for the free mode under

$$-2 < D_{BW} < -1. \quad (4.13c)$$

---

<sup>12</sup> The form  $e^{-i|\beta|\alpha z}$  is unacceptable because  $\exp i[-|\beta|z + x]\alpha$  does not give the correct Mach angle.

Note that for this free mode to occur, its propagation speed  $U$  must be less than  $C_1, C_p$ , and  $C_s$ , i.e. thoroughly subsonic.

An alternative is having  $U > C_1$  and  $C_s, C_p > U$ , i.e. being supersonic underwater. Equation (4.13b) is still a valid condition because

$$\sqrt{1 - M_1^2} = -i|\beta_1|, \quad |\beta_s \alpha| h = -i|\beta_s| |\alpha| h$$

in this case, with which the RHS of (4.13b) is changed according to

$$\frac{\tanh(|\beta_s \alpha| h)}{\sqrt{1 - M_s^2}} = \frac{\tan(|\beta_s \alpha| h)}{|M_s^2 - 1|^{1/2}}. \quad (4.14)$$

This would give an effervescent behavior in  $\Psi$  with respect to depth level  $z$ . The thoroughly subsonic case pertains to our interest, since we are concerned mainly with  $M_A < 4.53$  in the present context.

#### Overpressure field in water: generalization

The overpressure in the water channel/layer can be calculated from

$$p' = -\rho_1 U \frac{\partial^2}{\partial x^2} \Phi_1 = +\rho_1 U^2 \alpha^2 \left[ A_1 e^{|\beta_1 \alpha| z} + A_2 e^{-|\beta_1 \alpha| z} \right] e^{-i|\beta_1 \alpha| x}$$

and, with results from (4.11) and other relations established among constants  $A_1, A_2, B$ , and  $C$ , may be obtained in a normalized form

$$p' = \hat{q} e^{i\alpha x} \quad (4.15a)$$

with

$$\hat{q}(z, \alpha) = e^{-|\beta_1 \alpha|(h+z)} + \frac{e^{-|\beta_1 \alpha|(h-z)} - e^{-2|\beta_1 \alpha| h} \cdot e^{-|\beta_1 \alpha|(h+z)}}{(1 + e^{-2|\beta_1 \alpha| h} + D_{BW})} \quad (4.15b)$$

which satisfies the boundary condition  $\hat{q} = 1$  at the water surface  $z = -h$ . The product  $\hat{q} e^{i\alpha x}$  is a solution to the system with  $p' = e^{i\alpha x}$  at  $z = -h$ , so is its integral with respect to  $\alpha$

$$I(x, z) \equiv \frac{1}{\sqrt{2\pi}} \int_{-\infty}^{\infty} e^{i\alpha x} \hat{q}(z, \alpha) d\alpha = \frac{1}{\sqrt{2\pi}} \int_{-\alpha}^{\alpha} e^{-i\xi x} \hat{q}(z, \xi) d\xi. \quad (4.16a)$$

Since  $\hat{q}(-h, \xi) = 1$ ,  $I$  is recognized as the inverse Fourier transform of the underwater wave field generated by a concentrated surface overpressure

$$p'(x,0) = \delta(x) = \delta(-x) \quad (4.16b)$$

The inverse transform of the product of  $\hat{q}$  and another function of  $\xi$ , say  $\hat{P}(\xi)$ , not to be confused with  $P_o$  in (4.11b), may then be identified with the (normalized) overpressure field underwater for a known surface overpressure  $p'(x,0)$  (in the moving frame)

$$p'(x,z) = \frac{1}{\sqrt{2\pi}} \int_{-\infty}^{\infty} e^{-i\xi z} \hat{q}(z,-\xi) \hat{P}(\xi) d\xi \quad (4.17a)$$

with

$$\hat{P}(\xi) \equiv \frac{1}{\sqrt{2\pi}} \int_{-\infty}^{\infty} e^{i\xi x} p'(x,0) dx \quad (4.17b)$$

While the free mode for  $\hat{P} \equiv 0$ , if exists, is given by

$$\hat{p} = A_1 \left[ e^{|\beta_1 \alpha|z} - e^{-2|\beta_1 \alpha|h} e^{-|\beta_1 \alpha|z} \right] \Phi_1, \quad (4.18)$$

under a distributed surface overpressure  $p'(x,0)$ , there is the effect of the forcing described by (4.17) with the  $\hat{q}(z, \xi)$  given by (4.15b). Where the condition (4.13) for the free mode is met, (4.17) gives the result of forcing at resonance condition. The pole-like singularity of  $\hat{q}$  occurring at some  $\xi \rightarrow 0$  is responsible for the oscillatory behavior extending to large  $|x|$

$$p \sim \text{const. sgn}(x) e^{i\alpha x} \quad (4.19)$$

where  $a$  is a real constant. These underwater wave field behaviors and their critical depends on the Mach number  $M_A$  and the shear-wave speed  $C_s$  of the sediment are illustrated by three sets of examples shown below in Figs. 31, 32, and 33, assuming an incident N-wave.

#### Sediment elastic properties selected

The sediment boundary wave of interest requires all fields in  $\phi_1$ ,  $\Phi_2$ , and  $\Psi_2$  to remain subsonic, i.e.  $M_1$ ,  $M_p$ , and  $M_s$ , be all less than unity. If  $M_s \equiv (U/C_s)$  on the RHS of (4.13b) were too small, the system would degenerate to that of the Rayleigh wave. We shall select for this study the type of sediment materials with a shear-wave speed low enough to realize an  $M_A$  under 4.53. We select from the list of sand and mud with (averaged) measured and computed elastic constants, North Pacific sediment, on Table 8.2.1 in Clay & Medwin (1977), p. 258:

	$\rho/\rho_1$	$C_p (m/sec)$	$C_s (m/sec)$
I. Very fine sand (continental terrace)	1.91	1711	503
II. Clay (Abyssal hill)	1.42	1491	195
	(1.91)	(1711)	

where the  $C_s$  were computed from data of Young's moduli and other (measured) elastic constants. In both examples, the sound speed in air and water are taken to be  $C_a=331$  m/sec and  $C_1=1500$  m/sec, respectively. To bring out more distinctly the change brought about by the sediment shear-wave speed, we use the same density and compressive-wave speed in all examples considered.

#### Two cases with supersonic flight Mach number

With the set of constants assumed for data set I, we have  $\rho_2/\rho_1=1.91$ ,  $M_1=0.300$ ,  $M_p=0.263$ ,  $M_s=0.895$ ,  $\beta_1=0.954$ ,  $\beta_p=0.965$ ,  $\beta_s=0.446$ , and  $D_{BW}=-1.089$ . In addition, the water-layer depth is taken to be twice the signature length, i.e.  $h=2$ . The condition (4.13) gives, for this data set, the admissible Mach number range for the free mode

$$1.35 < M_A < 1.44 \quad (4.20)$$

Two Mach numbers  $M_A$  will be considered, one is within the above range for the free mode,  $M_A=1.36$ , and the other is outside of it,  $M_A=1.5$ . Overpressure waveform at the sea level for an incident N-wave is shown in Fig. 31a where the normalized maximum overpressure is set equal to 0.33. The underwater waveform at mid tank (i.e.  $z=-1$ ) computed for  $M_A=1.5$  from (4.17a,b) is shown in Fig. 31b. As expected, no evidence of interaction involving sediment medium can be found. In fact, the result differs little from that of a rigid, flat wall and compares closely with the result for  $h=1$ ,  $z=1/2$  examined earlier in Fig. 30.

Next, we examine the results for  $M_A=1.36$  falling in the  $M_A$ -range of (4.20) with otherwise the same data set. The overpressure waveforms at the water surface  $z=-h=-2$ , at mid tank  $z=-h/2=-1$ , and on the bottom  $z=0$ , are shown in Figs. 32a, 32b, and 32c, respectively. Unlike the underwater wave field for a rigid, inelastic lower wall and for an elastic wall for at  $M_A=1.5$  (Fig. 31b), undiminished sinusoidal oscillations at large distances in the form anticipated by (4.19) are seen at both the lower depths levels. The oscillation on the floor ( $z=0$ ) is seen to be *twice* as strong as that at mid channel ( $z=-h/2=-1$ ), indicating clearly that the disturbances are generated from the multi-media interaction and radiated upward from the new acoustic sources on the bottom. Examples with other Mach number falling within the range of (4.20) have also been studied with similar conclusions.

#### A case with $M_A < 1$

As another example, we employ the modified data set II which has a much lower shear-wave speed ( $C_s=195$  m/sec), keeping the density and compressive-wave speed same as in set I. The admissible  $M_A$  range for the free mode in this case is

$$0.524 < M_A < 0.562 \quad (4.21)$$

requiring a subsonic flight. The calculated results for  $M_A=0.54$  are presented in Figs. 33 a, b, c for a relatively thin water layer (shallower channel depth) with  $h=1$ . The overpressure waveforms with expected behavior and features under (4.21) are shown in Figs. 33a, 33b, 33c for  $z=-h=-1$ ,  $z=-h/2=-1/2$ , and  $z=0$ , respectively. The result in this case is less realistic since there can be no sonic boom at  $M_A < 1$  giving N-waves. While a different signature form can be used as an input to evaluate the function  $\hat{P}$ , the model example at hand suffices to indicate the potential of sediment boundary-wave excitation by low flying subsonic aircraft over shallow water with low sediment shear-wave speed.

A noticeable feature common to both mid-tank waveform in Figs. 31b and 32b is the lowering amplitudes and shortening oscillation periods in the vicinity of the center,  $x=0(1)$ ; the same feature is not found, however, at the floor level ( $z=0$ ). This feature supports a finding in Deshanais & Chapman's (1998) model study in that spectrum density in certain higher frequency band appear to increase with distance from the sediment interface. According to the present model, an explanation on a more elementary level can be made: the feature in question represents the *near-field* effect of the surface N-wave that attenuates and disappears at the bottom but remains detectable at mid channel.

Also of interest are the comparable values of the  $C_s$ ,  $C_p$ , and  $\rho/\rho_1$  selected for our model study that results in resonance in the  $M_A$  range  $1.35 < M_A < 1.44$  and the representative values  $C_s = 517$  m/sec,  $C_p = 1600$  m/sec, and  $\rho/\rho_1 = 1.8$  in Deshanais & Chapman's study. The estimate of  $C_s$  made for the power law in Deshanais & Chapman's

$$C_s = 160(z)^{0.3} \quad (4.22)$$

where  $z$  is in meter, is taken at  $z=50$ m. The Concord flight Mach number reported in the study was estimated at 1.75, equivalent roughly to be  $M_A \sim 1.5$ , being not far from the upper  $M_A$  limit 1.44 of (4.20).

The computational study in Deshanais & Chapman (1998) did not appear to allow a vanishing  $C_s$  at  $z=0$  as required by (4.22), since the variable medium properties were modeled by several uniform layers. On the other hand, Godin and Chapman (1999) have obtained an exact solution to the power-law shear-speed problem. The analysis documented in Appendix V below examines several features and issues of the power-law model.

## 5. Application to Rocket Space Launch

Underwater penetration of sonic-boom noise from rocket space launch has been shown by Cheng & Lee (1998), using a flat ocean model, to differ significantly from that of aircraft sonic booms not only for the much longer sea-level signature length, but in the signature waveform due mainly to the rocket plume. The latter gives rise to underwater field characteristics distinctly different from that anticipated for a balanced  $N$  wave. In the following, we examine from the available records the distinct features of the sea-level sonic boom waveform produced during the ascent phase of a space launch, and their impact on the underwater acoustic field. Examples will be analyzed with both flat and wavy-surface models.

### 5.1 Known and Anticipated Features

Three overpressure waveform representing the more severe sea-level sonic booms recorded during a typical space launch ascent are shown in Figs. 34a, b, c. The overpressure (in psf) shown in Fig. 34a at the sea level was inferred from data recorded during the ascent of Apollo 17 (Hick et. al. 1973) when the launch vehicle reached an altitude of 100,00 ft., where the ambient Mach number was about 3.55. The speed of the wave-field movement at the sea level inferred from the calculated wave fronts is estimated to be 1,150 ft/sec, which corresponds to a Mach number above water  $M_A = 1.03$  and a *subsonic* underwater Mach number  $M_w = 0.23$ . The peak of the sea-level overpressure exceeds 8 psf, while the signature length extends over an  $x$ -range of  $L' = 6,500$  ft (nearly 2 km).

Similar sea-level signature waveforms were recorded during the ascent of a Titan IV launch, Fig. 34b, with a peak overpressure also exceeding 8 psf, and a signature length estimated to be 1 km long. Figure 34c reproduced from Hilton & Henderson (1974) gives variants of sea-level overpressure wave forms recorded during Apollo 15 launch at different locations from launch site, among which is one with U-like double peaks along with the overpressure undershoot, much like the rabbit-ear or U-like feature characteristics of the overpressure distributions found near the *super-boom/cut-off* plane (Haglund 1996).

With the sea-level signature of Fig. 35a (same as Fig. 33a) as input, the corresponding overpressure underwater was computed in Cheng & Lee (1998) for a flat-ocean model to depths down to  $z = 1.5 L'$ . The overpressure at  $z = 1000$  ft and  $z = 5000$  ft corresponding  $0.156 L'$  and  $0.776 L'$  are shown in Fig. 35b and Fig. 35c respectively. Included also in Fig. 35c is a (negative) source-like representation for Sawyer's solution at large depths (in dashes), signifying the dominance of a sink-like behavior resulting from the non-vanishing, negative impulse from the extensive underpressure part of the sea-level signature. The latter has been attributed to the divergence effect of the rocket plume and to the ray-focusing effect due to the trajectory curvature and vehicle acceleration. Similar underwater features are expected of most space-launch examples in Figs. 34a, b, c. The subsequent study on a model utilizing the distribution from Titan IV (Fig. 34b) as input confirms the foregoing observations for the flat ocean and will reveal several unique physical and analytical properties of the wave field under a wavy surface.

Simple reasoning would suggest that owing to the large penetration depth made possible by the long signature length  $L'$ , the wavy-surface influence could not play a significant role, as it has been with the  $N$ -waves. As a significant source of infrasound production, however, this influence cannot be ignored as will be made apparent below.

## 5.2 Rocket Space Launch: Infrasound under a Wavy Ocean

As an example of surface wave influence on underwater sonic-boom noise produced during the ascent phase of a space launch, we use the Titan IV overpressure waveform in Fig. 34b as input. The similarity in shape of the Titan data with Fig. 34a and Fig. 34c (except for the one with double-spike feature), suggests that the horizontal Mach number for this data set must be in a supersonic  $M_A$ -range rather close to one, not fallen in the super boom domain. In the absence of concrete data on  $M_A$ , we took  $M_A = 1.08$  for this numerical study. Assuming a surface sound speed above water as  $a_A = 331$  m/sec, this  $M_A$ -value gives a surface speed for the sonic-boom wave as  $U = 357$  m/sec, hence a signature length corresponding to 3 seconds to be  $L' = 357 \times 3 = 1072m$ . Note that the precise  $M_A$  is immaterial for the present purpose since the corresponding wave field Mach number underwater is

$$M_w^2 = \left( M_A / 4.53 \right)^2 \quad \text{or} \quad \beta_w = \sqrt{1 - M_w^2},$$

which makes little difference from the values for  $M_A = 1$ , as long as  $M_A$  is close enough to one.

We shall first examine the case with  $k = 64$ . The latter corresponds to  $\lambda = 2\pi L'/k = 0.0982L' \sim 105.2m \approx 100m$ . Consider for the present purpose the wave field directly under the flight track ( $\Lambda = 0$ ) and a wave train well aligns with the flight track ( $\psi = 0$ ). The real and imaginary parts of the synchronized velocity potential  $\hat{\phi}_2$  is computed for this case applying the numerical procedure developed for general, non- $N$  waveform; the results are shown in Figs. 36a, b. Its Fourier transform, together with the Fourier transform of the boundary-transfer term computed also by a general, non- $N$  program, can be used to generate the Fourier transform of the surface overpressure produced by wavy surface interaction  $\hat{A}(\xi)$ ; the result is presented in Figs. 36c, d for  $M_A = 1.08$  and  $k = 64$ . Unlike

the case of the  $N$  wave, exact, analytic results for  $\hat{A}(\xi)$  is unavailable for accuracy assessment and for inferring the behavior of  $\hat{A}(\xi)$  for large  $k$  and large  $\xi$ . The graphs in Figs. 36c,d indicate nevertheless finite limits for  $|\hat{A}|$  as  $|\xi| \rightarrow \infty$ , consistent with the conclusion for the  $N$  waveform; a feature distinctly differing from the  $\hat{A}(\xi)$  for the  $N$ -wave, however, is the absence of the successive zero-crossings prevalent in Figs. 5, 12, and 14-16.

The inverse Fourier transform of the product  $\hat{A}(\xi)\sigma(\xi; z)$  may now be computed to obtain the part  $\hat{p}_2(x, z)$  of the synchronous solution at different depth level  $z$ . Results are presented in Figs 37a, b, c, d for depth levels equal to  $1/8$ ,  $1/4$ ,  $1/2$  and  $1$  of the signature length  $L'$ , corresponding to  $z = 0.125$ ,  $0.25$ ,  $0.50$  and  $1.00$ , respectively. Also included for comparison are results by the “far-field” formula computed from the product of  $\hat{A}(\xi) = \hat{A}(\eta)$  and an analytic function of  $\bar{z}$  and  $\eta = x/\bar{z}$ . The good agreement of the far-field formula with the more exact numerical evaluation at  $z = 0.125$  ought not come as a total surprise, since the far-field formula is expected to hold for large  $k\bar{z}$ . With  $k=64$ , the product  $k\bar{z}$  is large indeed even at  $z = 1/8$ .

To see how the presence of a surface wave train may affect the underwater overpressure waveform in the time domain, one must assign a value to  $\delta$  and a realistic scale to the overpressure, for which we take

$$\delta = 0.025$$

$$\max p' = 8.6 \text{ psf}$$

The latter was adopted in accord with the Titan IV launch record in Fig. 32b. The results are presented in Figs. 38a, b, c, d for four depth levels  $z=1/8$ ,  $1/4$ ,  $1/2$  and  $1$ , where the overpressure waveforms of the Sawyers flat-ocean model  $p'_1$  (in light dashes), the wavy-surface contribution  $p'_2$  (dash-dot curve), and their sum (solid curve) are plotted against time in seconds. Labeled along the ordinates for the overpressure in psf are the corresponding units in  $dB$  (re  $1\mu\text{Pa}$ ). The smooth, sink-like waveform from the flat-ocean model reaches down to a (negative) peak as low as  $-0.4 \text{ psf}$  at  $z=1/8$  ( $0.125 \text{ km}$ ) and  $-0.14 \text{ psf}$  at  $z=1$  ( $1 \text{ km}$ ), comparable to those found earlier for the Apollo 17 launch (Cheng & Lee 1998). The wavy-surface effects (dash-dot curves) may not seem to contribute noticeably to the overpressure magnitude, there is a significant difference from results of the flat-ocean model with regard to *infrasound* production: whereas, the signal durations of 10 – 30 seconds of these plots give a frequency range of  $1/30 - 1/10 \text{ Hz}$  for the flat-ocean model, the wavy-surface interaction generates a wave-packet with frequency in the range of  $3 - 5 \text{ Hz}$  (estimated by counting peaks) and a peak sound pressure well above  $0.02 \text{ psf}$  or  $120 \text{ dB}$  (re  $1 \mu\text{Pa}$ ). To be sure, at the deepest level  $z=1$ , the frequency is in the range of  $5 - 6 \text{ Hz}$  with the wave-packet overpressure  $114 - 126 \text{ dB}$  (re  $1 \mu\text{Pa}$ ). Accordingly, these infrasound signals at depth level  $1/2 - 1 \text{ km}$  underwater have durations 20-30 seconds, depending on the chosen cut-off amplitude. Noteworthy is the *frequency downshift* characteristics, which is typically  $3 - 4 \text{ Hz}$  downshifting to  $1 - 2 \text{ Hz}$  for depth level  $1/8 - 1/4 \text{ km}$ , and  $5 \text{ Hz}$  downshifting to  $3 \text{ Hz}$  at the larger depth levels  $1/2 - 1 \text{ km}$ . Even though the peaks of the wavelets are relatively small, the wave-surface effect does add markedly to the total overpressure. All results shown can be closely reproduced by the semi-analytic procedures based on the far-field formula described earlier, including the smallest depth level  $z=1/8$ .

To see how a reduction in the surface-wave number  $k$  may affect the underwater signal waveform and intensity, we examine the case of  $k = 16$ , with  $M_A$ ,  $\delta$  and other parameters unchanged. The results for  $k = 16$  are presented in Figs. 39a, b, c, d through 41a, b, c, d in an order corresponding to results presented earlier for  $k = 64$ . Of the time-domain overpressure waveforms in Figs. 41a, b, c, d, a common feature noticeably different from those in Figs. 38a, b, c, d for the higher  $k$  is the lower carrier-wave (wavelet) frequency of the wave packet (cf. dash-dot curves); this is made evidenced by the increased spacing between the neighboring wavelets, expected as a result of the four-fold reduction in  $k$ .

A more significant property upon examining closely these two data sets is, however, a significant departure from the cylindrical spreading rule  $1/\sqrt{k\bar{z}}$  established for high  $k\bar{z}$  studies of  $N$ -waves and similar waveforms (Appendix IV). The peak  $|p'_2|$  from the foregoing calculations for the space launch reveals, instead, a slight reduction from that for  $k = 64$ . Owing to the importance of this issue, a computer program re-run was made for the case of  $k = 64$  with the  $\xi$  - range extending much further to  $-300 < \xi < 300$ ; the results change little however from those of the earlier runs.

To see more clearly the reason for this departure and the significant difference in the wavy-surface effect between a rocket space launch sonic boom and the carpet booms from a supersonic aircraft, one may reexamine the integral solution (3.14) that can be recast for a given Mach number  $M_A$  and large  $k\bar{z}$ , as

$$\hat{p}_2(\eta, k\bar{z}; k) = \frac{1}{\sqrt{2\pi}} \int_{-\infty}^{\infty} k \hat{A}(\bar{\xi}; k) e^{i(|K|^{1/2} - \eta)(k\bar{z})} d\bar{\xi} \quad (5.1a)$$

where

$$\bar{\xi} = \xi/k, \quad K \equiv K/k\beta^2 = \bar{\xi}^2 - \bar{P}\bar{\xi} - \bar{Q}$$

$$\bar{P} = P/k, \quad \bar{Q} = Q/k^2,$$

and

$$\hat{A}(\xi; k) = \hat{A}(k\bar{\xi}; k) = \hat{A}(\bar{\xi}; k) \quad (5.1b)$$

For cases with  $N$ -waves, as well as waveform made of step functions and polynomials of  $x$ ,  $k\hat{A}(\xi; k)$  is independent of  $k$  in the limit  $k \rightarrow \infty$  [cf. (IV.3 in Appendix IV)] and  $\hat{p}_2$  is clearly a function of  $(k\bar{z})$ , according to (5.1) and its further simplification that yields the cylindrical spreading rule

$$|\hat{p}_2| \propto |k\hat{A}(\xi_*; k)| / \sqrt{k\bar{z}} \sim D(\bar{\xi}_*) / \sqrt{k\bar{z}} \quad (5.2)$$

where  $\bar{\xi}_*$  is a function of  $\eta$  alone. In the more general case, the far field formula for high  $k\bar{z}$

$$\hat{p}_2 \propto \frac{k\hat{A}(\xi_*, k)}{\sqrt{k\bar{z}}} \quad (5.3)$$



still holds, as it has been substantiated by the foregoing examples for a fixed  $k$ . However, the computed results shown in Figs. 35-37 indicate that  $|\hat{A}|$  may no longer reduce with large  $k$  simply as the reciprocal of  $k$  for those sea-level waveforms shown in Figs. 34a, b, c; therefore the inverse  $\sqrt{kz}$  rule for  $\hat{p}_2$  may not apply in these cases involving large and different  $k$ 's.

The foregoing examinations and comparisons have not only brought out several distinct underwater wave field feature unique to the rocket space launch, but also the importance of the function  $\hat{A}(\xi; k)$ ; its analytical structure and its relations to physical nature of the wave field deserve more thorough investigation in future work.

## 6. Concluding Remarks

The work in Part I is extended and applied to calculations for model examples of sonic boom noise penetration into wavy and non-wavy (flat) oceans, and to studying the sea-floor influence and the sediment-boundary wave excitation. The numerical study of concrete examples substantiates that, due to the much lower attenuation rate (cylindrical spreading), the time-dependent disturbances produced by the interaction of incident sonic boom waves with a sinusoidal surface-wave train can overwhelm the otherwise flat-ocean (Sawyers) wave field at depth levels much larger than, as well as comparable to the signature length  $L'$ , depending on the flight Mach number  $M_A$ , the wave number  $k$ , the alignment angle  $\psi$ , and the max. slope  $\delta$  of the surface-wave train. Calculations for supersonic aircraft, including cases with nonaligned as well as multiple wave trains, indicate that, under sea states corresponding to moderate and fresh breezes, disturbances at levels of 120-130 dB (re 1  $\mu Pa$ ) can reach a depth level of 300-450m where the sonic boom noise will be perceived as a wave-packet with carrier-wave frequency in the 10-40 Hz range, which is commonly characterized by a frequency downshift. Same dB levels are found at comparable depth level (200-400m) in examples of rocket space-launch ascent, but mainly in the low infrasound frequency (1-10 Hz) range. Significant differences in underwater noise characteristics between sonic booms from supersonic aircrafts and that during a space-launch ascent operation, result primarily from the presence of the rocket plume through its effect on the acoustic exposure spectral density  $\hat{A}(\xi_*)$ .

One noticeable feature of sonic boom noise in deep water is the relatively long transit time that may expose the reception to a higher ambient noise level. The length of this duration will depend on the threshold sound-pressure level chosen. Using the threshold value of 100 dB (re 1  $\mu Pa$ ) for the present purpose, the ambient noise would appear in a sound-pressure level no higher than 87 dB (re 1  $\mu Pa$ ) for the aircraft example and 95 dB (re 1  $\mu Pa$ ) for the case of a rocket space launch, and is not expected to mask the sonic boom signal underwater of interest at 100 dB (re 1  $\mu Pa$ ) and higher.<sup>13</sup>

The bottom effect is found to little affect Sawyers' prediction even in shallow water at depth levels as small as a half of the signature length, except in the immediate vicinity of the sea floor where significant increase in peak overpressure can be found. Depending on the elastic properties of the seafloor, the examples studied substantiate that sediment-boundary waves can be excited by supersonic overflight, and is detectable in shallow water.

---

<sup>13</sup> The estimates were based on the max. average vessel traffic noise of 80 dB (re 1  $\mu Pa$ ) [Wenz 1962, Urlick 1983] for deep and shallow water.

As is the theory in Part I, various parts of the computer codes have been up-dated for a general program, not restricted to the special case of an incident N-wave, based on the improved version, in which several anomalies (and non-uniformities associated with the solution discontinuities) in the earlier version of the theory have been removed. Critical tests have shown that the general numerical program is highly accurate. The far-field analysis for the case of incident N-wave has been extended to allow application of high surface-wave number  $k$ , which becomes extremely effective for predictions applied to problems of rocket space launch, and proves to be vital in the further extension of the interaction theory to non-sinusoidal, periodic surface-wave trains.

A resolved issue may be noted in passing; it concerns the magnitude of the water surface depression under loading from the sonic boom overpressure, not considered in this and other theories. In resolving the issue, an explicit solution for the surface depression under an N-wave was obtained (not reproduced here); applications with realistic max. overpressure and pulse transit time under field as well as laboratory conditions confirmed that the amount of surface depression in question is far below that of the surface-wave train, at least by an order of  $10^{-4}$ .

Several investigations on the wavy-surface effect that remain to be completed are apparent from the discussions presented above and are noted below.

#### **I. Need for wider parametric and type coverage; graphics and audio**

Space-Launch Examples—Available recorded/computed sea-level sonic boom signatures pertinent to modern space-launch operation needs must be included in a more extensive wave-field study.

Wider Parameter Coverage—Ranges of Mach number, surface wave number, wave height, wave-train alignment angle, etc. should be enlarged to allow more realistic representations; an analytical development for high surface- wave-number is included.

Graphic and Audible—Static and cinematic contour plots illustrating wave-field penetration depth and time sequence are needed to reach a wider audience and aid insight; audio play-back in synch with computed wave packet in transit is also expected to help in this respect.

#### **II. Marine mammal response to audio playback**

Underwater Experiments with Marine Mammals—Over-pressure signals computed from theory for deep water is broad-cast and directed to a marine mammal species (preferably not too far from the surface, when the sea is relatively calm) in close range, in an audio play-back experiment under water to observed/record the animal's response to the predicted deep-water sound. The project is to be carried out jointly with marine biologists and may reduce substantially the resource for supporting full-scale flight and space-launch operations

#### **III. Shallow-water response to sonic booms**

Non-Wavy Shallow Water—Large parameter domain of a flat, shallow ocean, including the limit of a vanishing depth, must be explored and ascertained. The work will be a joint theoretical and experimental effort.

Wavy Shallow Water—Response to sonic boom in this case has not been analyzed thus far; laboratory investigation is expected to precede theory in this study.

Sediment Boundary Wave Excitation—Studies will include greater varieties in elastic properties and in shear-wave speed distribution, including the singular problem of a vanishing shear-wave speed at the sediment interface; the study will be made jointly with seismic-acousticians; laboratory study in limited scope will be considered.

Near-Surface Wave Field of a Wavy Ocean—The results, not thoroughly delineated thus far, may impact significantly the study of potential physiological harm to a broader animal group, including dolphins and seals.

#### **IV. Non-uniform surface wave train and other laboratory issues**

Attenuation and Compactness (Finite Length) of Surface Wave Train—In response to the capillary wave decay observed in the laboratory measurement, a new theory is being developed to address non-uniformity in surface wave train due to attenuation and other shape changes; the analysis multi-scale and Laplace transform technique. Test of theory will be provided by comparison with underwater measurement for laboratory-generated compact wave train..

### **Acknowledgement**

The authors would like to express their appreciation of the fruitful collaborations and enlightening communications with M. Badiey, A. Bowles, D.M.F. Chapman, C.S. Clay, F. Desharnais, G. D'Spain, A. Fincham, C.R. Greene, R. Kaplan, J. Kunc, Y.G. Li, V. Lang, G. Malcolm, T. Maxworthy, H. Medwin, P. Newton, R. Nigbor, L. Redekopp and J. Sigurdson. Our work has also received much benefit from discussions with E. Haering, V. Sparrow, R. Sohn, and fellow members of the Southern California Sonic Boom Forum and also with colleagues at the University of Southern California, and the Aerospace Corporation.

The production of this report could not have realized in time without the able assistance of A. Anaya, L. Aragon, M. Patel, M. Penoliar, J. Wong and other AME Department staffs. A good part of this work was produced under the Ocean Sonic Boom Program sponsored by the Environmental Management Division, AF Missile and Space System Center, Los Angeles, through Parsons Engineering Science Subcontract: 738249-3000-00 during July 2000-August 2001. The helpful assistance and valuable service offered by A. Hashad and R. Crisologo and their colleagues in program and contract management are gratefully acknowledged.

### **References**

- Air Force Material Command (1997) "Environmental Assessment for USAF Atmospheric Interceptor Technology Program", Dept. AFMC Headquarter
- ARPA, NOAA and State of Hawaii (1995) "Final Environ. Impact Statement for the Kauai Acoustic Thermometry of Ocean Climate Project and its Assoc. Marine Mammal Res. Program", ARPA, NOAA & Univ. Calif., San Diego vols. I & II
- Badiey, M., Cheng, A.H.D. and Jaya, I. (1996) "Deterministic and Stochastic Analyses of Acoustice plane-wave Reflection From In Homogeneous Porous Seafloor", *J. Acoust. Soc. Am.*, vol.99, no.2
- Badiey, M., Cheng, A.H.D. and Mu, Y. (1998) "From Geology to Geoacoustics--Evaluation of Biot-Stoll Sound Speed and Attenuation for Shallow Water Acoustics", *J. Acoust. Soc. Am.*, vol.103, no.1, pp.309-320
- Bascom, W. (1964) *Waves and Beaches*; Educational Services, Inc.

- Benjamin, T.B. (1967) "The Instability of Periodic Wave Trains in Certain Nonlinear Systems, *Proc. Roy. Soc. London*, Ser. A, vol.299, pp.59-75
- Benjamin, T.B. and Feir, J.E. (1967) The Disintegration of Wave Trains in Deep Water, Pt. I. Theory, *J. Fluid Mech.*, vol.27, pp.417-430.
- Bowles, A. and Stewart, B. (1980) "Disturbances to the Pinnipeds and Birds of San Miguel Island, 1979-1980", in *Potential Effect of Space Shuttle Sonic Boom on Biota and Geology of Calif. Channel Islands* (ed. J.R. Jehe & C.F. Cooper) also as Tech. Rept. 80-1, San Diego State Univ., Hunsb-Sea World Res. Inst. And USAFS Space Div.
- Carson, H.W. and Maglieri, D.J. (1972) "Review of Sonic Boom Generation Theory and Prediction Methods", *J. Acoustical Soc. America*, vol.51, no.2 (pt.3), pp.675-685
- Chapman, D.M.F. and Godin, O.A. (1999) "Dispersion of Interface Waves in Sediments with Power-Law Shear Speed Profiles I: Experimental Observation and Seismo-Acoustic Inversions", proc. 3<sup>rd</sup> Int. Cong. Theoretical & Comp. Acoustics
- Churchill, R.V. (1941) *Fourier Series and Boundary Value Problems*, McGraw Hill Book Co, New York & London, pp.64-87
- Cheng, H.K. and Lee, C.J.(2000) "Sonic Boom Noise Penetration Under Wavy Ocean: Part I. Theory", Univ. Southern Calif. Dept. Aerospace and Mechanical Engineering, USC AME Report 11-11-2000; documented on web site "<http://www-bcf.usc.edu/~hkcheng>"
- Cheng, H. K. and Lee, C. J..(2002) "Sonic Boom Noise Penetration Under a Wavy Ocean: Theory manuscript completed for journal publication.
- Clay, S. C. and Medwin, H., *Acoustical Oceanography*, John Wiley & Son (1977).
- Cook, R. (1970) "Penetration of a Sonic Boom into Water", *J. Acoustic Soc. Am.*, vol.47, no.3, pt.2, pp.1430-1460
- Cumming, W.C. and Thompson, P.O. (1971) "Underwater Sounds from Blue Whale, *Balaenoptera Musculus*", *J. Acou. Soc. Am.*, vol.50, no.4, pp.1193-1198
- Darden, C.M., ed. (1988) Status of Sonic Boom Methodology and Understanding, NASA Conf. Pub. 3027
- Desharnais, F. and Chapman, D.M.F. (1998) "Underwater Measurement and Modeling of a Sonic Boom", *J. Acoustical Soc. Am.*, vol.104, no.3. pt.2, p.1848
- D'Spain, G.L. Hodgkiss, W.S. and Edmons, G.L. (1991) "Energetics of the Deep Ocean's Infrasonic Sound Field", *J. Acoust. Soc. Am.*, vol.89, no.3, pp.1134-1158
- D'Spain, G.L., Kuperman, W.A., Hodgkiss, W.S. and Berger, L.P. (1995) "3-D Localization of Blue Whale", Univ. Calif., San Diego, Scripps Inst. Oceanography Marine Physical Lab. Report, *MPL Tech. Memo. 447*; also see *J. Acoust. Soc. Am.*, vol.97, no.5, pp.3353

- Edds, P.L. (1988) "Characteristics of Finback, *Balaenoptera Physalus*, vocalization in the St. Lawrence Estuary", *Bioacoustics*, vol.1, pp.131-149.
- Frankel, A.S. and Clack, C.W. (1998) "Results of Low Frequency Playback of M-Sequence Noise to Humpback Whales, *Megaptera Novaeangliae*, in Hawaii", *Canadian J. Zool.*, vol.76, pp.521-535
- Gladwin, D.N., Mancini, K.M. and Vilella, R. (1988) "Effect of Aircraft and Sonic Booms on Domestic Animals and Wildlife: Biographic Abstracts", Tech. Rept. US Fishery & Wildlife Service Nat. Ecology Center
- Godin, O.A. and Chapman, D.F.M (1999) "Dispersion of Interface Waves in Sediments with Power-Law Shear Speed Profiles II: Exact and Approximate Analytical Results", paper submitted to *J. Acoust. Soc. Am.*
- Guiraud, J.P. (1965) "Acoustics Geometrique, bruit balistique des avions supersoniques et focalisation", *J. de Mecanique*, vol.4, pp.215-267
- Hamilton, E.L. (1971) "Elastic Properties of Marine Sediments" *J. Geophysic. Res.*, vol.76, pp.579-604
- Hayes, W.D. (1971) "Sonic Boom", *Annual Rev. Fluid Mech.*, vol.3, pp.269-290
- Hilton, P.A. and Henderson, H.R. (1974), "Measurements of Sonic Boom Overpressure from Apollo Space Vehicles", *J. Acoust. Soc. Am.*, vol.56, no.2, pp.323-328.
- Holloway, P.E., Wilbold, G.A., Jones, J.H., Garcia, F., and Hicks, R.A. (1973) "Shuttle Sonic Boom Technology and Prediction" AIAA Paper 73-1039
- Hunter, J. and Keller, J.B. (1983) "Weakly Nonlinear High Frequency Waves", *Comm. Pure Appl. Math.*
- Hunter, J. and Keller, J.B. (1984) "Weak Shock Defraction" *Wave Motion*, vol.6, pp.79-89
- Interier, P.F. and Malcolm, G.N. (1973) "Ballistic Range Investigation of Sonic Boom Overpressure in Water", *AIAA J.*, vol.11, no.4, pp.510-516
- Lang, V.I., Huynh, T., Bowles, A., Stewart, B. and Plotkin, K. (2001) "Environmental Impact Assessment of U.S. Air Force Launches from Kodiak, Alaska, Aerospace Report TR-2001(1306)-2
- McDonald, M.A. and Fox, C.G. (1999) "Passive Acoustic Methods Applied to Fin Whale Population Density Estimation", *J. Acoust. Soc. Am.*, vol.105, no.5, pp.2643-2651
- Medwin, H., Helbig, R.A. and Hagy, J.D. (1973) *J. Acoustical Soc. Am.*, vol.54, no.1, pp.99-109
- Medwin, H. and Clay, C.S. (1998) *Fundamental of Acoustic Oceanography*, Acad. Press
- Munk, W.H. (1956) "Waves of the Sea", *Encyclopedia Britannica*, Ed. 1956, vol. 23, pp.442-444
- National Research Council Ocean Study Board Committee (1992) Low Frequency Sound and Marine Mammals, NRC Rept. 1992, vol.viii

- Natural Resource Defense Council (1999) "Sounding the Depth: Supertankers, Sonar, and the Rise of Undersea Noise", NRDC Rept.
- Office of Assoc. Admin. Commercial Space Transportation (2001) Programmatic Environmental Impact Statement for Licensing Launches, vols.I, II, prepared by ICF Consulting, Inc. for AST, FAA and DOT
- Pipe, L.A. (1946), "*Applied Math for Engineers and Physicists*", McGraw Hill Book Co., pp.49-68
- Plotkin, K. J. (1985) "Evolution of a Sonic Boom Focal-Zone Prediction Method", Wyle Lab. Rept. WR 84-43, Feb. 1984
- Potter, J.R. (1994) *J. Environment and Development*, vol.3, no.2, pp.47-62
- Redekopp, L. (1980) Lecture Notes on Linear and Nonlinear Waves, Univ. So. Calif.
- Richardson, W.J., Greene, C.R., Jr., Malme, C.I. and Thompson, D.H. (1995) *Marine Mammals & Noise*, Acad. Press, pp.15-86,525-552
- Richardson, W.J. and Wursig, X.X. (1997) "Influence of Man-Made Noise and Other Human Actions on Cetacean Behavior", *Marine Freshwater Behavior Physiology*, vol.29, p.188
- Sawyers, K.H. (1968) "Underwater Sound Pressure from Sonic Boom", *J. Acoustice Soc. Am.*, vol.44, no.2, pp.523-524
- Schwartz, I.W. (1974) Computer Extension and Analytic Continuation of Stokes' expansion for gravity waves, *J. Fluid Mech.*, vol.62, pp.553-578
- Sparrow, V.W. and Ferguson, T. (1997) "Penetration of Sharp Sonic Boom Noise into a Flat Ocean", *AIAA*, paper 97-0486
- Sparrow, V.W. (1995) "The Effect of Aircraft Speed on the Penetration of Sonic Boom Noise in Flat Ocean", *J. Acoustic Soc. Am.*, vol.97. pp.159-162
- Sohn, R.A., Vernon, F., Hildebrand, J.A. and Webb, S.C. (1999) "Field Measurement of Sonic Boom Penetration into the Ocean", *J. Acoust. Soc. Am.*, vol.107, no.6, pp.3073-3082
- Stewart, B.S., Young, R.W., Francine, J.K. and Drawbridge, M. (1991) "Geological Effects of Launch-Specific Related Noise and Sonic Booms from Titan IV on 8 March 1991", *Huubs-Sea World Res. Inst. Report*, 96-264: 1-68
- Stoll, R.D. (1989) *Sediment Acoustics*, Lecture Notes in Earth Sciences, Springer Verlag
- Thomas, C.L. (1972) "Extrapolation of Sonic Boom Signature by the Waveform Parameter Methods", *NASA TND-6832*
- Tolstoy, I. And Clay, C.S. (1966) *Ocean Acoustics*, McGraw Hill
- Urlick, R.J. (1983) *Principles of Underwater Sound*, McGraw Hill

- Van Dyke, M.D. (1975) *Perturbation Methods in Fluid Mechanics*, the Parabolic Press, p.216
- Walkden, F. (1958) "The Shock Pattern of Wing-Body Combination Far from the Flight Path", *Aeronautical Quarterly*, vol.9, pp.164-194
- Water, J. (1971) "Penetration of Sonic Energy into the Ocean: An Experimental Simulation", *Noise & Vibration Control Engineering Proc. Noise Control Conf. Purdue Univ.*, (ed. M. Croker), pp.554-557
- Wenz, G.M. (1962) "Acoustic Ambient Noise in the Ocean: Spectra and Source, *J. Acoustical Soc. Am.*, vol.34, no.12, pp.1936-1956
- Yih, C.S. (1977) *Fluid Mechanics*, West River Press, pp.201-209
- Yuen, H.C. and Lake, B.H. (1980) *Annual Review in a Fluid Mech.*, vol.12, p.303

## Captions of Figures

- Fig. 1 Schematic representation of the interaction problem, showing variables and quantities used in the analysis
- Fig. 2 Sketch illustrating the sonic boom impact zone in the horizontal reference plane, with surface-wave crests represented by thin solid lines. The two sets of coordinates  $(x, y)$  and  $(x', y')$  are fixed to the moving frame, with  $\Lambda$  and  $\psi$  identified with the local swept angle of the surface impact zone and the non-alignment angle of the surface-wave vector, respectively.
- Fig. 3 The boundaries in the  $\Lambda$ - $\psi$  realm enclosing the cylindrical-spreading domains for four surface Mach numbers  $M_A = 1.05, 1.5, 2.0$ , and  $3.0$ , in which the surface-wave interaction effects attenuates according to the inverse square-root rule.
- Fig. 4a Semi-analytical and asymptotic results of real and imaginary parts of the surface-velocity potential  $\phi$  pertaining to the synchronous solution above water for an incident N-wave at surface Mach number  $M_A = 1.821$  and surface-wave number  $k=4$ .
- Fig. 4b Semi-analytical integrated results of real and imaginary parts of the normalized contribution to the synchronous surface pressure  $\hat{p}_2(x', 0)$  for N-wave at  $M_A = 1.821, k=4$ .
- Fig. 5 Real and imaginary parts of the Fourier transform of  $\hat{p}_2(x', 0)$  for N-wave with  $M_A = 1.821, k=4$  and their comparison with the exact analytic results.
- Fig. 6 Real and imaginary parts of the synchronous surface pressure  $\hat{p}_2(x', z)$  for N-wave with  $M_A = 1.821, k=4$  at depth level equal to one half signature length  $z=0.5$ .
- Fig. 7 The  $\hat{p}_2(x', z)$  at depth level equal to two and a half signature length  $z=2.5$ , with conditions otherwise same as in the preceding figure.
- Fig. 8 Time-domain waveforms of overpressure at the reference surface  $z=0$  produced by an incident N-wave at  $M_A = 1.821, k=4$  computed from the flat surface (in dashes), from the surface-wave interaction effect (dash-dot curve), and from the sum of the two (solid curve).
- Fig. 9 Time-domain waveforms of overpressure at depth level equal to one half signature length  $z=0.5$ , with conditions otherwise same as in preceding figure.
- Fig. 10 Time-domain waveforms of overpressure at depth level two and a half signature length  $z=2.5$ , with conditions otherwise same as in preceding figure.
- Fig. 11 Real and imaginary parts of surface  $\phi$  for N-wave at  $M_A = 1.5, k=4$  computed from the semi-analytical method (developed for N-wave) and from the general numerical program applicable to non-N-waves. [The comparisons in this and the three following sets serve as a critical test of the more general program].



- Fig. 12a Real and imaginary parts of the Fourier transform of the  $\hat{p}_2(x', 0)$  correction for transferring the boundary from  $z=Z_W(x', 0)$  to the reference surface  $z=0$  for N-wave with  $M_A = 1.5$  and  $k=4$ .
- Fig. 12b Real and imaginary parts of the Fourier transform of  $\hat{p}_2(x', 0)$  for N-wave with  $M_A = 1.5$ ,  $k=4$ .
- Fig. 13 Real and imaginary parts of  $\hat{p}_2(x', z)$  at depth level two and a half signature length  $z=2.5$  for N-wave with  $M_A = 1.5$ ,  $k=4$ .
- Fig. 14a Real and imaginary parts of the Fourier transform of  $\hat{p}_2(x', 0)$  from numerical calculations and its comparison with the exact analytical results for N-wave with  $M_A = 1.5$  and  $k=4$ .
- Fig. 14b Fourier transform of  $\hat{p}_2(x', 0)$  from numerical calculation and comparison with exact analytical results for N-wave with  $M_A = 1.5$  and  $k=16$ .
- Fig. 15 Fourier transform of  $\hat{p}_2(x', 0)$  from numerical calculation and comparison with exact analytical results for N-wave with  $M_A = 1.88$  and  $k=16$ .
- Fig. 16 Fourier transform of  $\hat{p}_2(x', 0)$  from numerical calculation and comparison with exact analytical results for N-wave with  $M_A = 2.38$  and  $k=16$ .
- Fig. 17a Example of underwater overpressure waveform produced by N-wave with  $M_A=1.5$ , surface-wave number  $k=4$ , maximum wave slope  $\delta=0.025$ , sea-level signature length  $L'=300\text{ft.}$ , and max. sea-level overpressure 2 psf, at two depth levels:  $z'L'=150\text{ft}$  and  $z'L'=1500\text{ft}$ .
- Fig. 17b Example of underwater overpressure waveform with  $M_A = 1.5$ ,  $k=16$  at two depth levels, with conditions otherwise same as in the preceding figure.
- Fig. 18 Example of underwater overpressure waveform with  $M_A = 1.88$ ,  $k=16$  at two depth levels, with conditions otherwise same as in the preceding figure.
- Fig. 19 Example of underwater overpressure waveform with  $M_A = 2.38$ ,  $k=16$  at two depth levels, with conditions otherwise same as in the preceding figure.
- Fig. 20 Example of N-wave interacting with surface-wave train for  $M_A = 2.38$ ,  $k=16$  at different non-alignment angles  $\psi$  and at different span-station swept angle  $\Lambda$ : real and imaginary parts of surface velocity potential  $\phi$  as functions of  $x'$  for combinations  $(\Lambda, \psi)=(0, 0)$ ,  $(-15^\circ, 0)$ ,  $(0, 15^\circ)$ , and  $(-15^\circ, 15^\circ)$ .
- Fig. 21 Example of N-wave interacting with surface-wave train at different non-alignment angles  $\psi$  and swept angle  $\Lambda$ : real and imaginary parts of the Fourier transform of  $\hat{p}_2(x', 0)$ ; conditions otherwise same as in preceding figure.

- Fig. 22 Example of N-wave interacting with surface-wave train at different  $\psi$  and  $\Lambda$ : real and imaginary parts of the synchronous overpressure  $\hat{p}_2(x', z)$  at the depth level  $z=2.5$ ; conditions otherwise same as in preceding figure.
- Fig. 23 Test of far-field formula for  $\hat{p}_2(x', z)$  at span-station removed from the flight track at depth level  $z=2.5$  for the case of  $\Lambda=-15^\circ$ ,  $\psi=0$  for  $M_A = 2.38$  and  $k=16$ .
- Fig. 24 Example of N-wave interacting with surface-wave train at different  $\psi$  and  $\Lambda$  angles: real and imaginary parts of  $\phi$  as functions of  $x'$  for  $(\Lambda, \psi)=(0, 0)$ ,  $(0, 30^\circ)$ , and  $(-30^\circ, 30^\circ)$ ; conditions otherwise same as in Figs. 20 thru 22.
- Fig. 25 Example of N-wave interacting with surface-wave train at different  $\psi$  and  $\Lambda$  angles: real and imaginary parts of Fourier transform of  $\hat{p}_2(x', 0)$ ; conditions otherwise same as in Fig. 24.
- Fig. 26 Example of N-wave interacting with surface-wave train at different  $\psi$  and  $\Lambda$  angles: real and imaginary parts of the synchronous overpressure  $\hat{p}_2(x', z)$  at depth level  $z=2.5$ ; conditions otherwise same as in Figs. 24 and 25.
- Fig. 26x.a Example of N-wave interacting with surface-wave train: overpressure time-domain waveform with  $M_A = 2.38$ ,  $k=16$ ,  $\delta=0.025$ , at depth levels  $z=2.5$ , for  $\Lambda=0$ ,  $\psi=0$ .
- Fig. 26x.b Overpressure time-domain waveform at  $z=2.5$ , for  $\Lambda=0$ ,  $\psi=30^\circ$ ; conditions otherwise same as in preceding figure.
- Fig. 26x.c Overpressure time-domain waveform at  $z=2.5$ , for  $\Lambda=-30^\circ$ ,  $\psi=30^\circ$ ; conditions otherwise same as preceding figure.
- Fig. 27a Surface-wave ordinate (depression) as function of time resulting from superposition of two aligned surface-wave trains with slightly different wave numbers,  $k=3.8, 4$ .
- Fig. 27b Overpressure time-domain waveform at depth level  $z=5$  produced by a N-wave of max  $p'=2$  psf and  $L'=300$ ft. interacting with a single well aligned wave train ( $\Lambda=\psi=0$ ), with  $\delta=0.025$ , for  $k=4$ .
- Fig. 27c Overpressure time-domain waveform at depth level  $z=5$ , for  $k=3.8$ ; conditions otherwise same as in preceding figure.
- Fig. 27d Overpressure time-domain waveform at depth level  $z=5$  (1,500ft.) produced by N-wave of max peak overpressure 2 psf and  $L'=300$ ft. interacting simultaneously with two aligned wave trains ( $\Lambda=\psi=0$ ), of  $\delta=0.025$ , one with  $k=3.8$  and the other with  $k=4.0$ .
- Fig. 28a Example of sonic boom interacting with a “cross sea” (multiple wave trains with different non-alignment angles): overpressure time-domain waveform at depth level  $z=2.5$  in the presence of two wave trains  $(\Lambda, \psi)=(0, 0)$  and  $(\Lambda, \psi)=(0, 30^\circ)$ ; conditions otherwise same as in Figs. 16x.a and 16x.b.
- Fig. 28b Example of sonic boom interacting with a “cross sea”: overpressure time-domain waveform at depth level  $z=2.5$  in the presence of two wave trains  $(\Lambda, \psi)=(0, 30^\circ)$  and  $(\Lambda, \psi)=(0, -30^\circ)$ .

- Fig. 29 Comparison of the sinusoidal and the Stokesian waves for different slope parameters  $\delta=0.025, 0.05, \text{ and } 0.10$ , at the same surface-wave number  $k=4$ .
- Fig. 30 Example illustrating sea-floor influence on underwater overpressure waveform produced by an N-wave incident upon a flat interface. In this examination, the depth level  $z$  (distance from the interface) is  $z=0.5$  (one half of the signature length  $L'$ ), while the channel depth ratio takes on several values  $h/L' = 0.5 \text{ thru } \infty$ .
- Fig. 31 Example of sonic boom disturbance penetrating into shallow water in which sediment boundary wave is not excited. The normalized max. overpressure is 0.33 and the channel depth ratio is  $h/L' = 2.0$ ; the density and sound speeds of water and sediment material are listed with the figure. For this set of properties, sediment-boundary wave cannot be excited unless  $1.33 < M_A < 1.44$ . The waveform shown for the mid channel for  $M_A=1.5$  indicates no sign of resonance, as expected. (a) overpressure on water surface, (b) overpressure at mid channel  $z=-1$ .
- Fig. 32 Example of sonic boom disturbance penetrating into shallow water in which sediment boundary wave is excited. Conditions same as in preceding figure except  $M_A=1.36$ , fallen within the resonance range  $1.33 < M_A < 1.44$ . (a) overpressure on water surface, (b) overpressure at mid channel, and (c) overpressure on sea floor.
- Fig. 33 Example of sediment boundary wave in shallow water excited by a traveling disturbance at subsonic speed. The set of density and sound speed properties shown with the figure differs from that in the preceding figure mainly in shear-wave speed  $C_s$ , being 195 m/sec. instead of 503 m/sec. For this set, the resonance condition is  $0.521 < M_A < 0.562$ . A highly idealized N-waveform is assumed on the water surface for simplicity. The example shown for  $M_A=0.54$  indicates sediment wave excitation, as expected.
- Fig.34 Representative sonic booms recorded at sea level during the earliest phase of rocket space launch: (a) Apollo 17 Ascent, (b) Titan IV Ascent, (c) Apollo 15 Ascent.
- Fig. 35 Overpressure waveform at three depth levels according to the flat-ocean (Sawyers) model based on the sea-level overpressure signature from the Apollo 17 ascent record: (a) sea level, (b)  $z=0.156$  (1,000ft.), and (c)  $z=0.776$  (5,000ft.).
- Fig. 36a Example of sonic boom from rocket space launch interacting with a well aligned surface-wave train ( $\Lambda=\psi=0$ ) assuming  $M_A=1.08$ ,  $k=64$ ,  $L'=1$  km and a sea-level overpressure same as one recorded for Titan IV launch [Fig. 34(b)]: real and imaginary parts of surface velocity potential  $\phi$  of the synchronous solution.
- Fig. 36b Real and imaginary parts of the Fourier transform of the synchronous surface pressure,  $\hat{A}(\xi)$ ; conditions same as in the preceding figure.
- Fig. 37a Real and imaginary parts of the normalized synchronous overpressure  $\hat{p}_2(x', z)$  at depth level  $z=1/8=0.125$  and comparison with prediction by (semi-analytic) high- $k$ , far-field formula; conditions same as in the preceding figure.

- Fig. 37b Real and imaginary parts of  $\hat{p}_2(x', z)$  at depth level  $z=1/4=0.25$  and comparison with results from the high- $k$ , far-field formula; conditions otherwise same as in the preceding figure.
- Fig. 37c Real and imaginary parts of  $\hat{p}_2(x', z)$  at depth level  $z=1/2=0.5$  and comparison with results from high- $k$ , far-field formula; conditions otherwise same as in the preceding figure.
- Fig. 37d Real and imaginary parts of  $\hat{p}_2(x', z)$  at depth level  $z=1$  and comparison with results from high- $k$ , far-field formula; conditions otherwise same as in the preceding figure.
- Fig. 38a Predicted overpressure time-domain waveform at depth level  $z=1/8$ , assuming max. surface-wave slope  $\delta=0.025$ ; conditions otherwise same as in Fig. 37a.
- Fig. 38b Predicted overpressure time-domain waveform at depth level  $z=1/4$ , assuming  $\delta=0.025$ ; conditions otherwise same as in Fig. 37b.
- Fig. 38c Predicted overpressure time-domain waveform at depth level  $z=1/2$ , assuming  $\delta=0.025$ ; conditions otherwise same as in Fig. 37c.
- Fig. 38d Predicted overpressure time-domain waveform at depth level  $z=1.0$ , assuming  $\delta=0.025$ ; conditions otherwise same as in Fig. 37d.
- Fig. 39a Example of sonic boom from rocket space launch interacting with a well aligned surface-wave train ( $\Lambda=\psi=0$ ) assuming  $k=16$ ; conditions otherwise same as in Fig. 36a: real and imaginary parts of  $\phi$ .
- Fig. 39b Real and imaginary parts of  $\hat{A}(\xi)$ ; conditions same as in the preceding figure.
- Fig. 40a Real and imaginary parts of  $\hat{p}_2(x', z)$  at depth level  $z=1/8$  and comparison with high- $k$ , far-field prediction; conditions otherwise same as in the preceding figure.
- Fig. 40b Real and imaginary parts of  $\hat{p}_2(x', z)$  at depth level  $z=1/4$  and comparison with high- $k$ , far-field prediction; conditions otherwise same as in the preceding figure.
- Fig. 40c Real and imaginary parts of  $\hat{p}_2(x', z)$  at depth level  $z=1/2$  and comparison with high- $k$ , far-field prediction; condition otherwise same as in the preceding figure.
- Fig. 40d Real and imaginary parts of  $\hat{p}_2(x', z)$  at depth level  $z=1$  and comparison with high- $k$ , far-field prediction; conditions otherwise same as in the preceding figure.
- Fig. 41a Predicted overpressure time-domain waveform at depth level  $z=1/8$ , for  $\delta=0.025$ ; conditions same as in Fig. 40a.
- Fig. 41b Predicted overpressure time-domain waveform at depth level  $z=1/4$ , for  $\delta=0.025$ ; conditions same as in Fig. 40b.

- Fig. 41c Predicted overpressure time-domain waveform at depth level  $z=1/2$ , for  $\delta=0.025$ ; conditions same as in Fig. 40c.
- Fig. 41d Predicted overpressure time-domain waveform at depth level  $z=1$ , for  $\delta=0.025$ ; conditions same as in Fig. 40d.

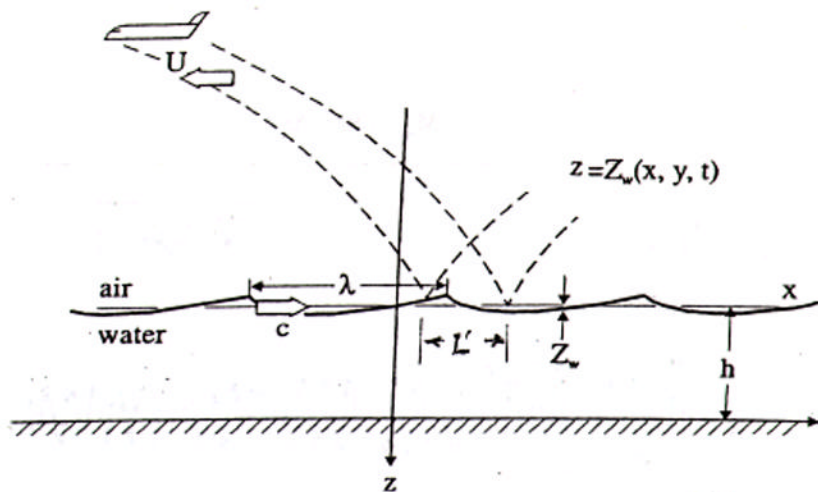


Fig. 1

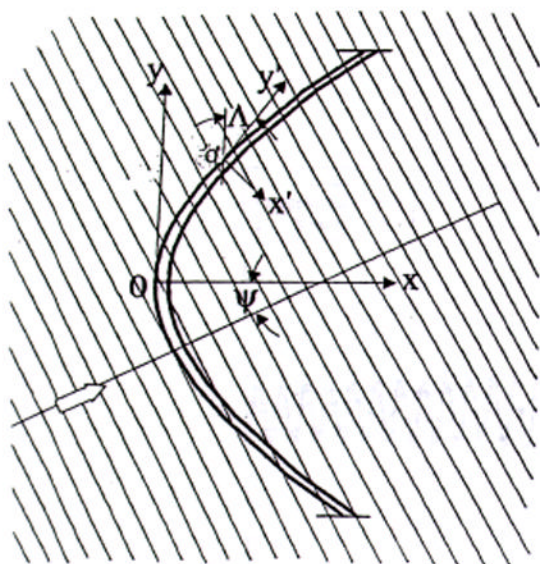


Fig. 2

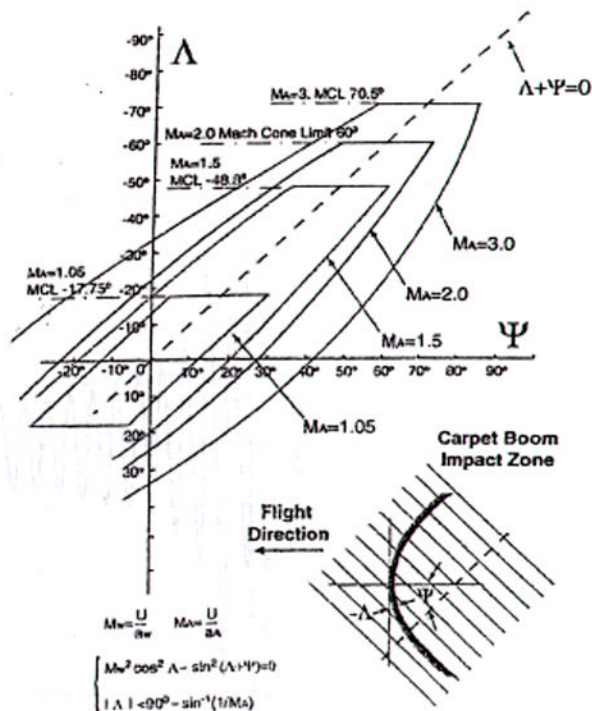


Fig. 3

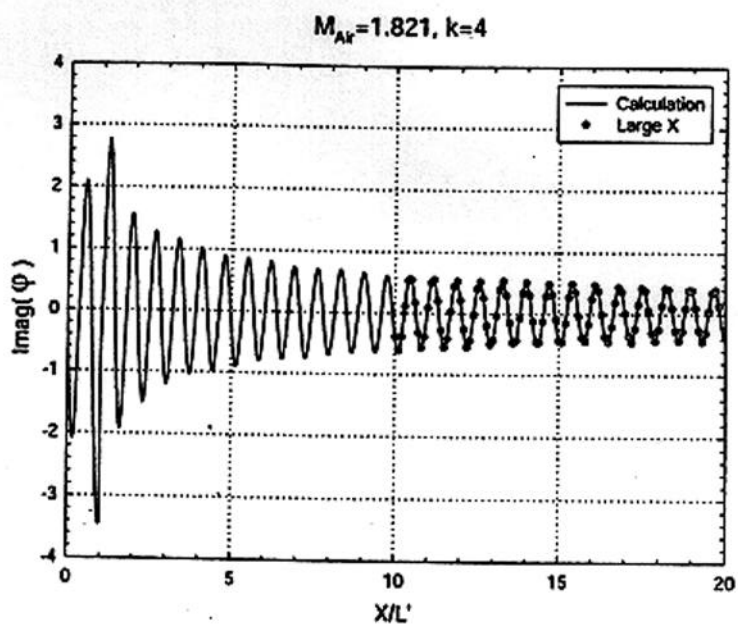
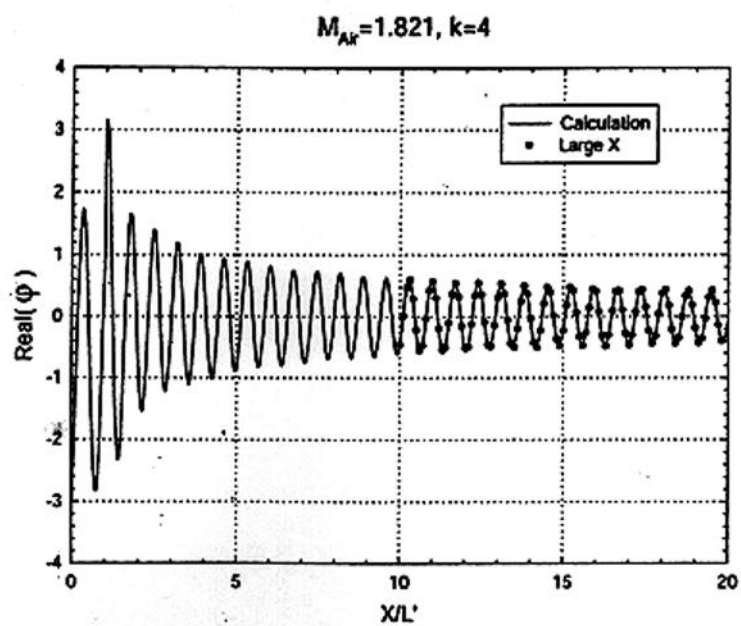


Fig. 4a

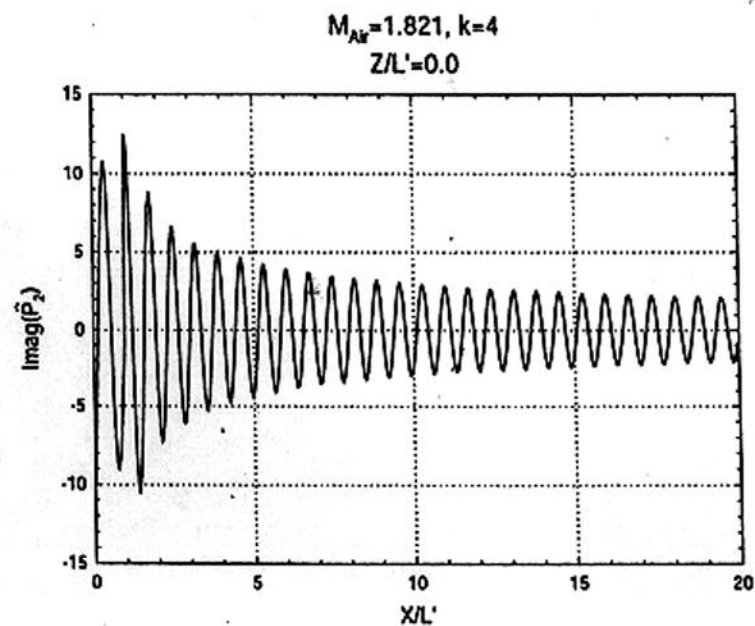
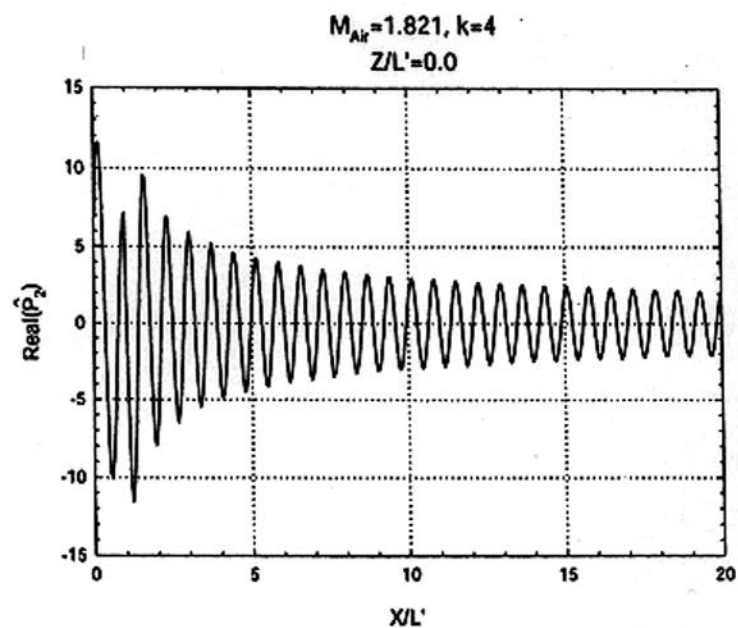


Fig. 4b

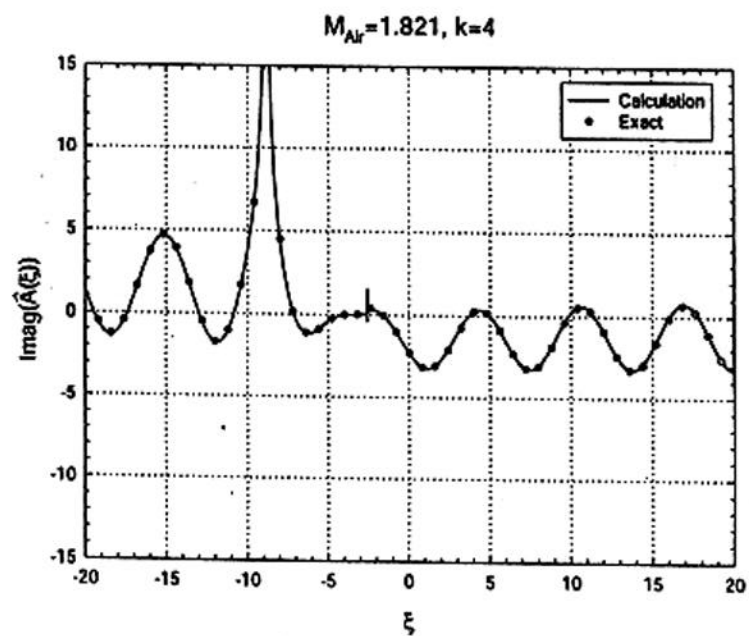
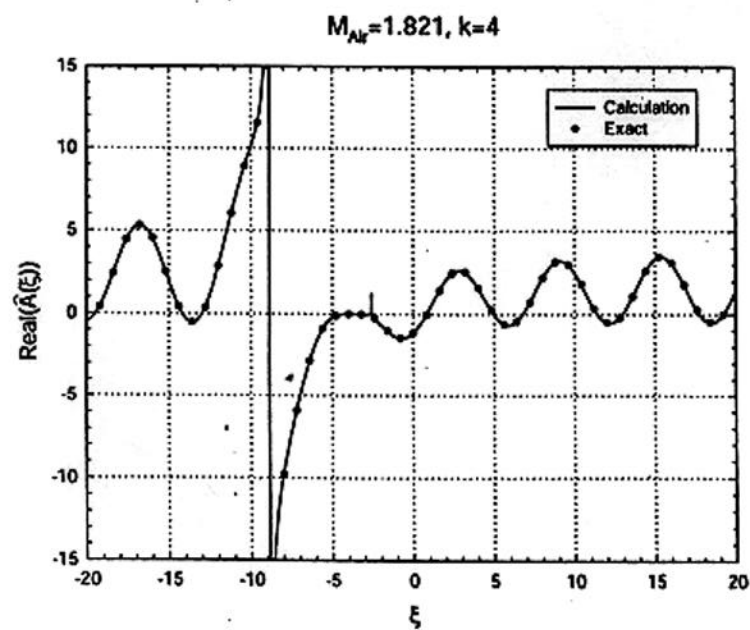


Fig. 5



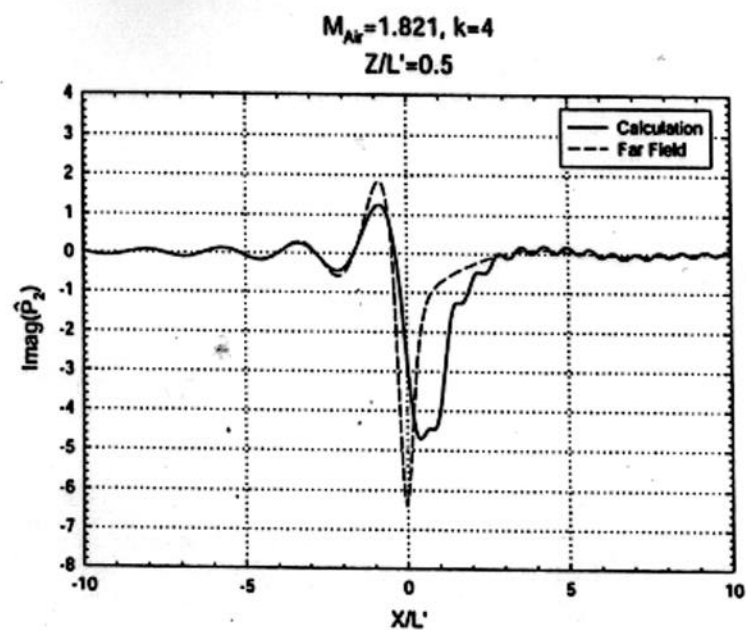
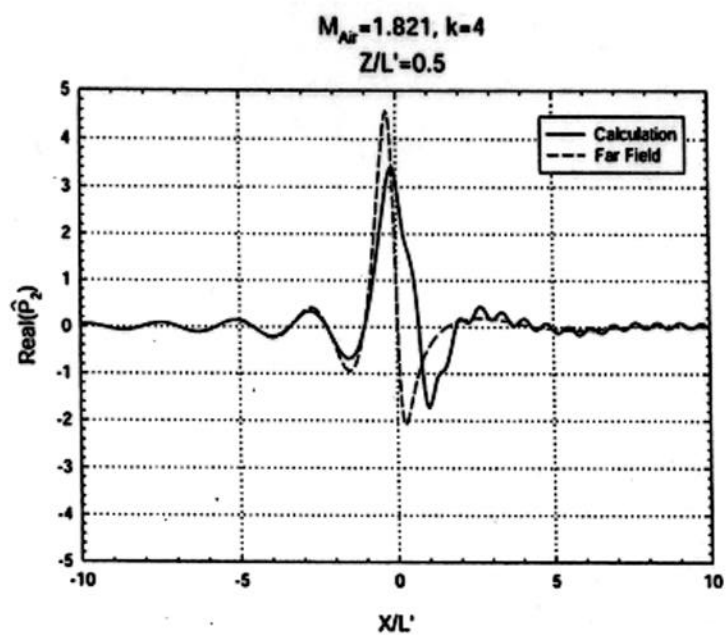


Fig. 6

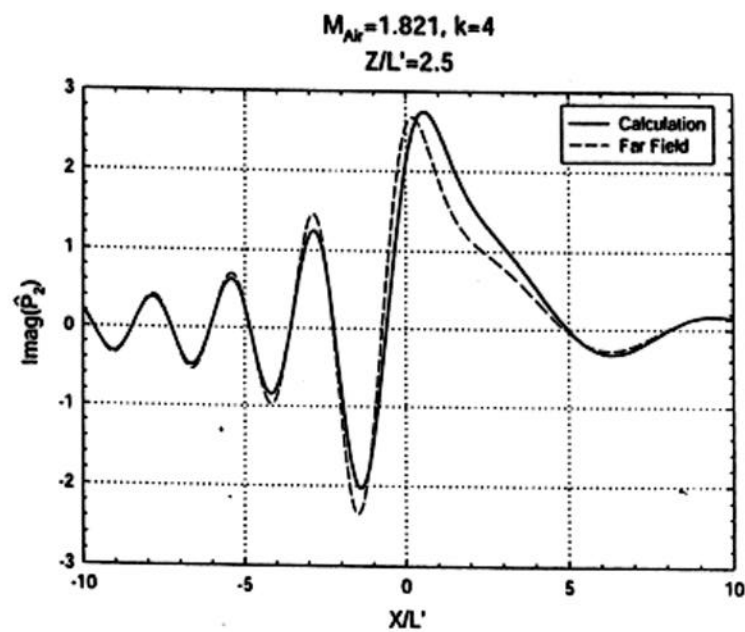
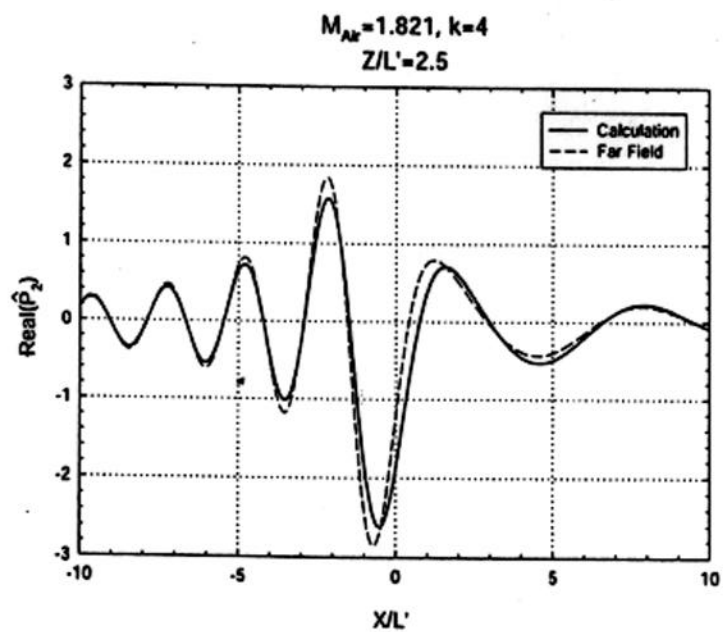


Fig. 7

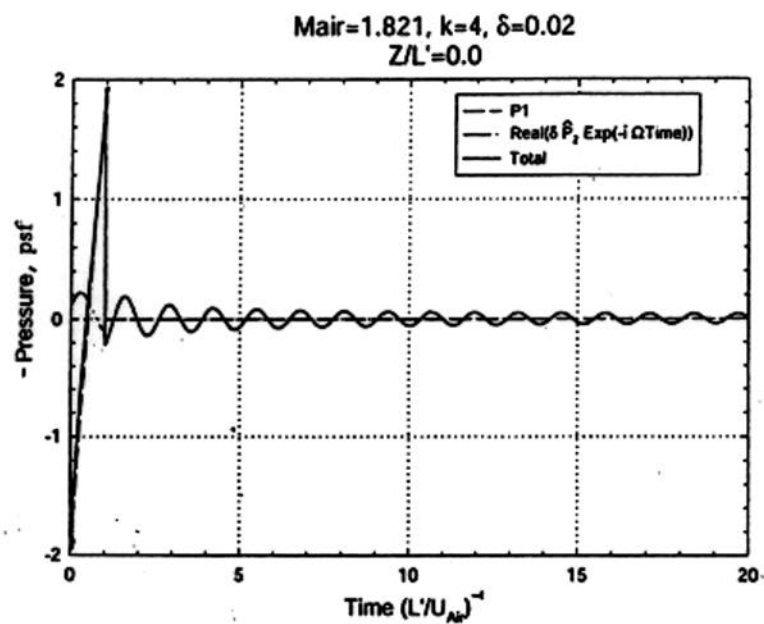


Fig. 8

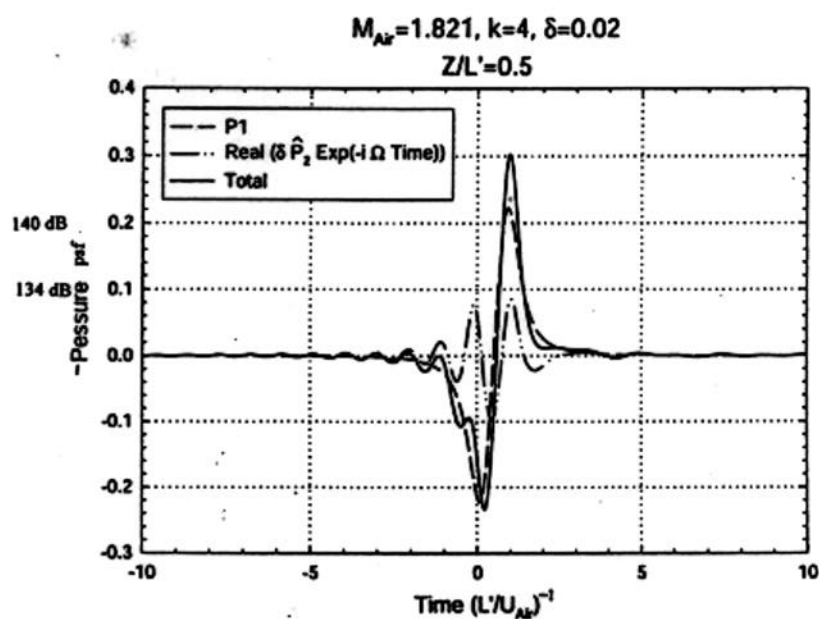


Fig. 9

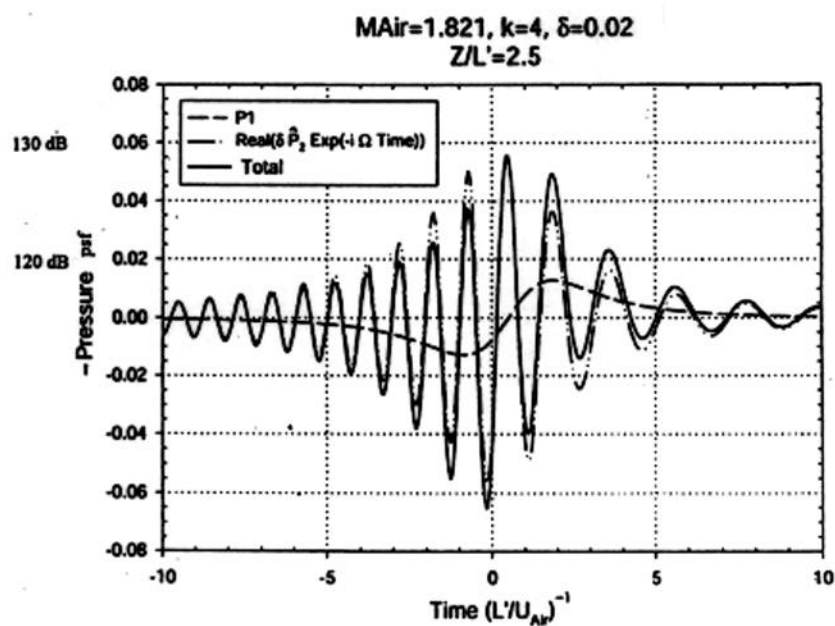


Fig. 10

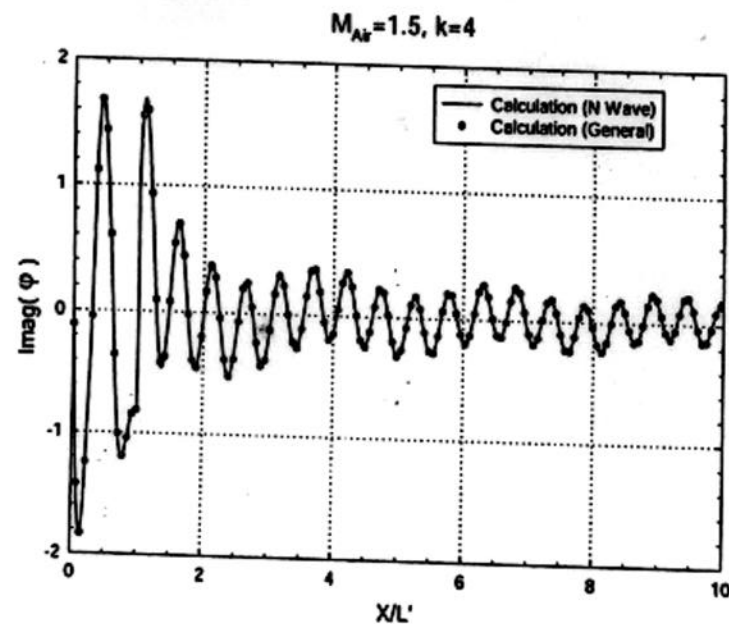
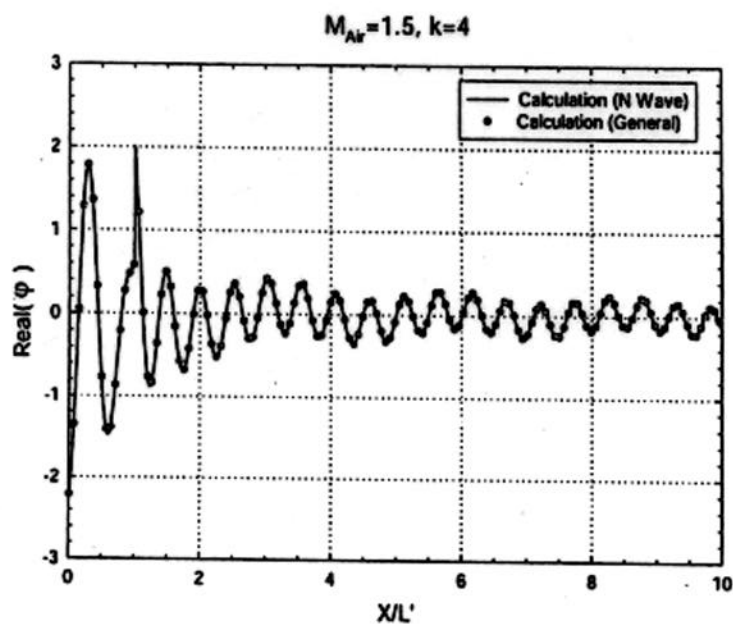


Fig. 11

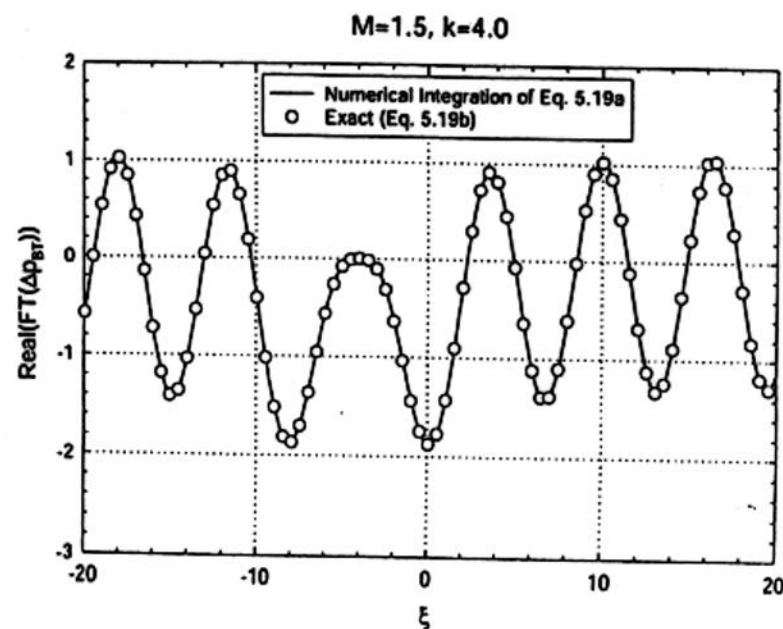
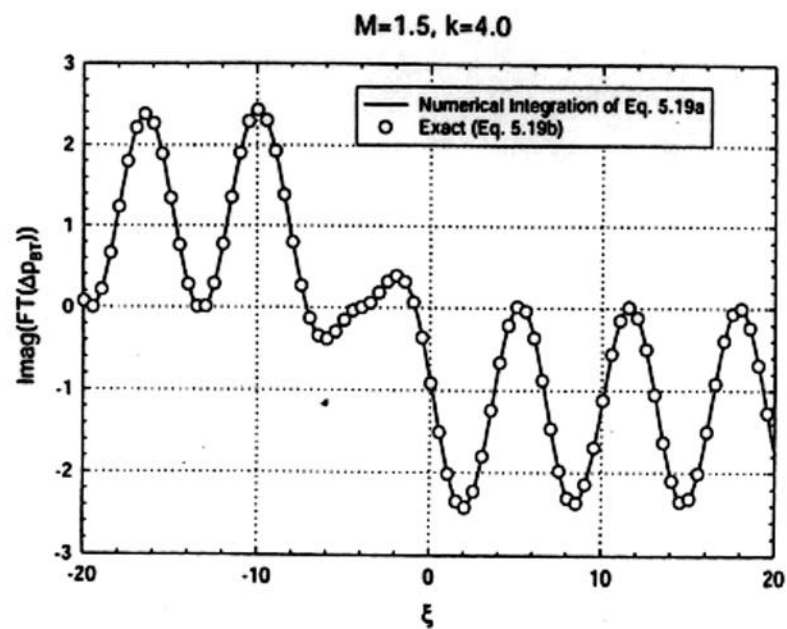


Fig. 12a

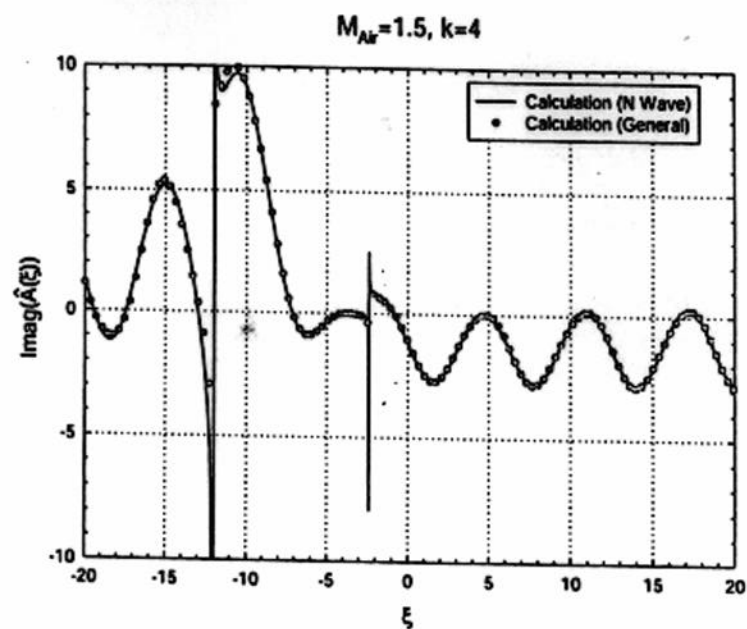
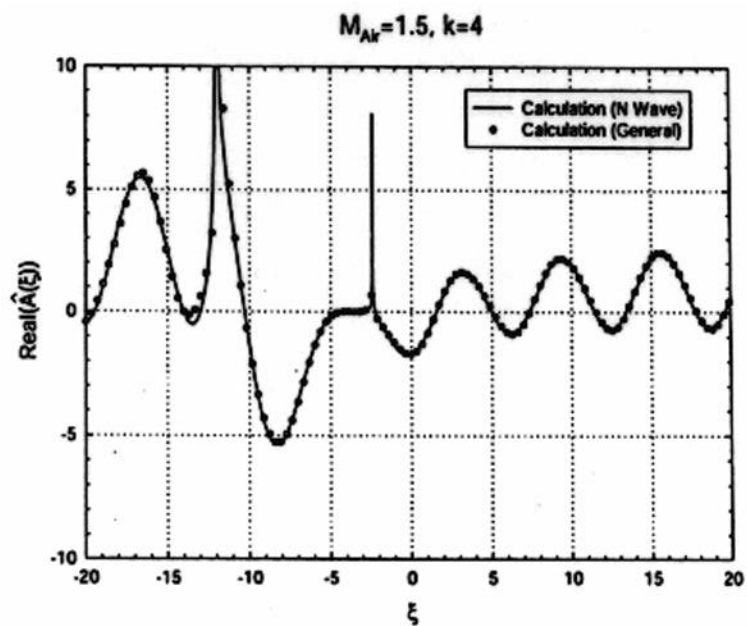


Fig. 12b

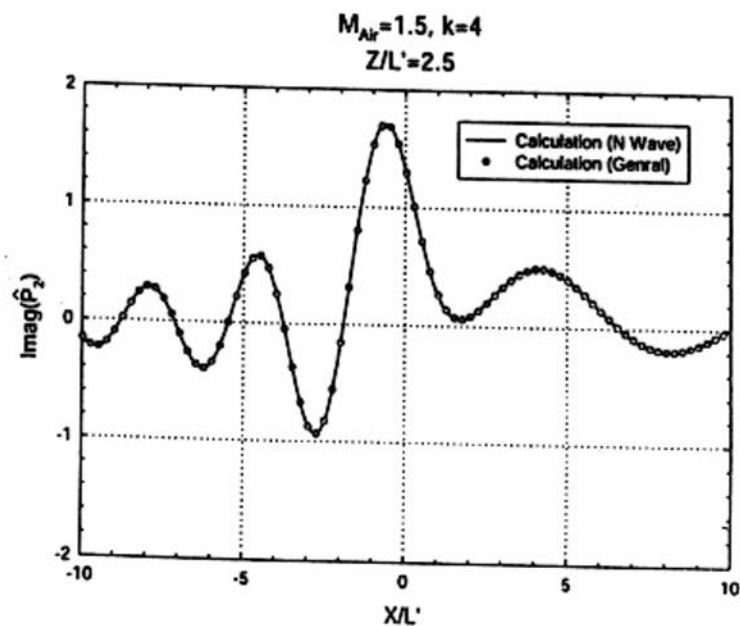
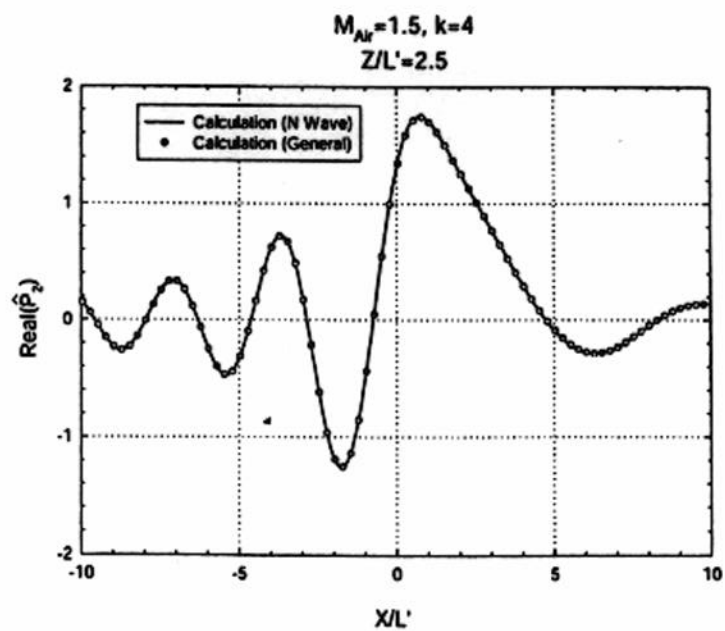


Fig. 13

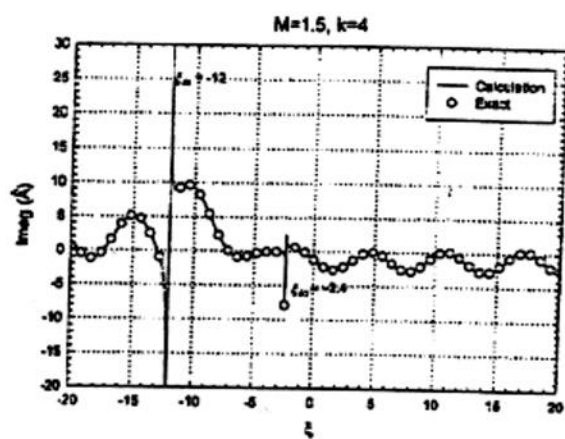
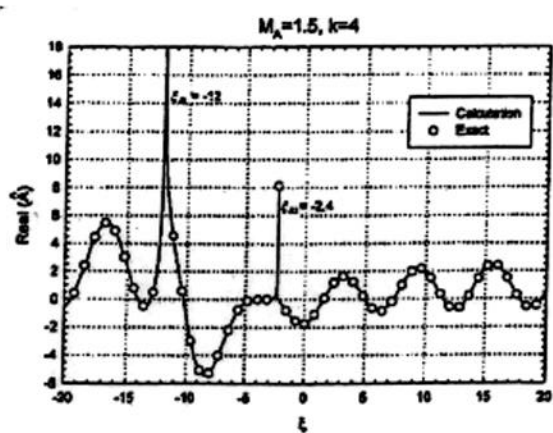


Fig. 14a

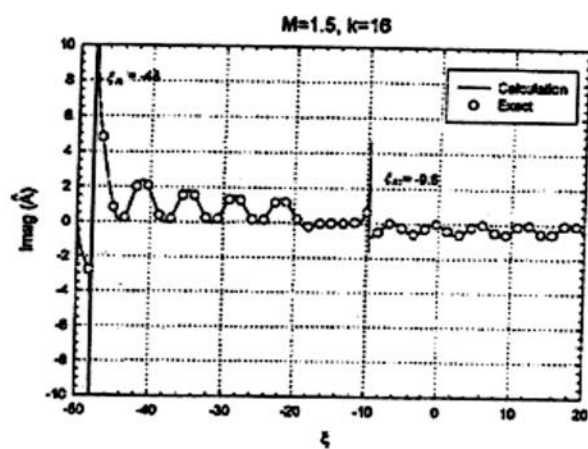
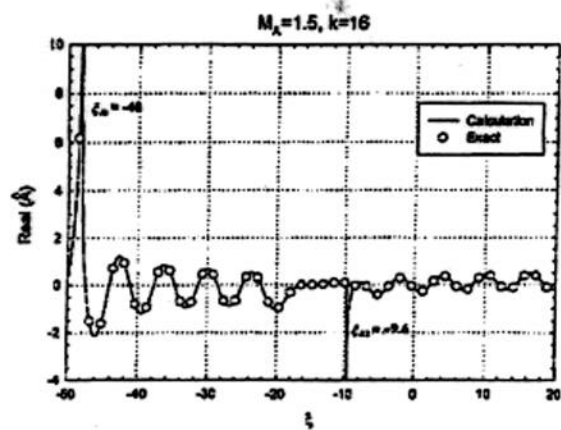


Fig. 14b

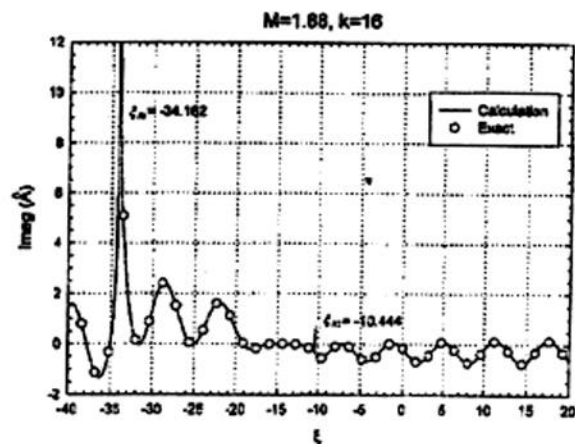
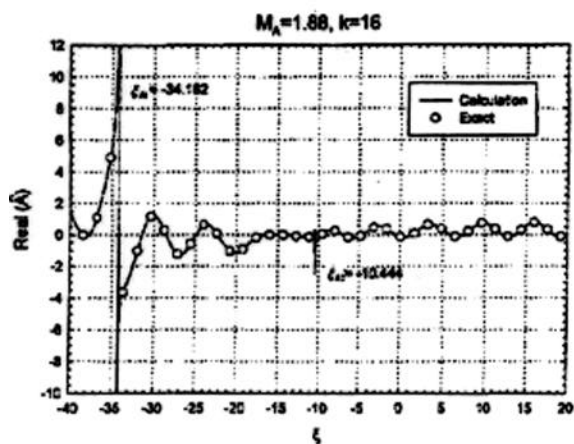


Fig. 15

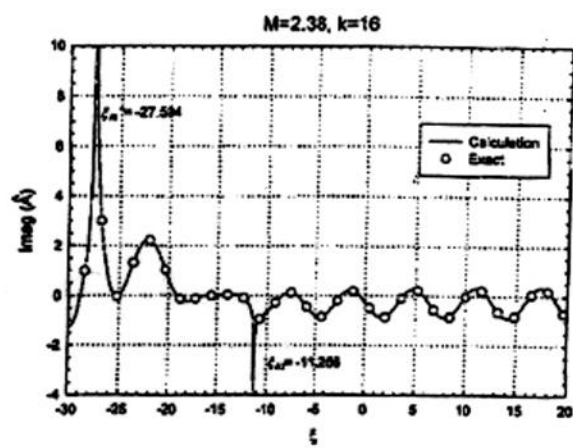
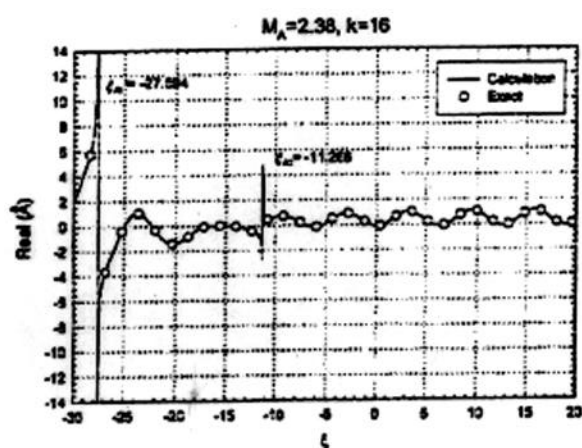


Fig. 16

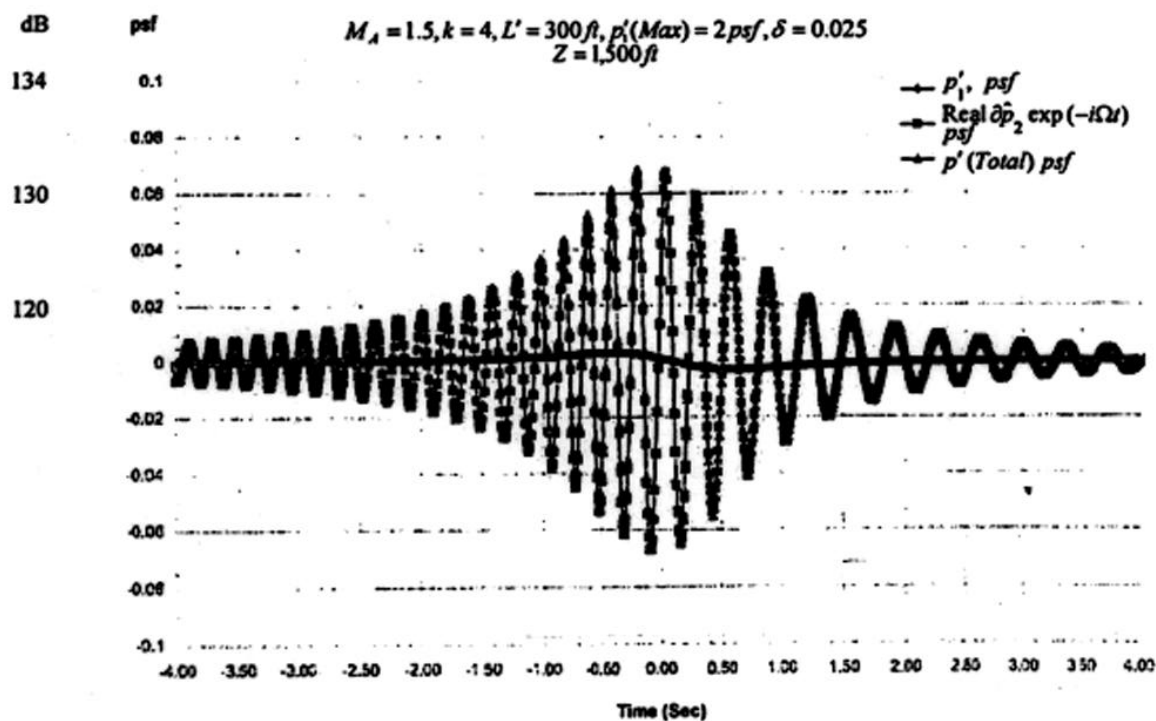
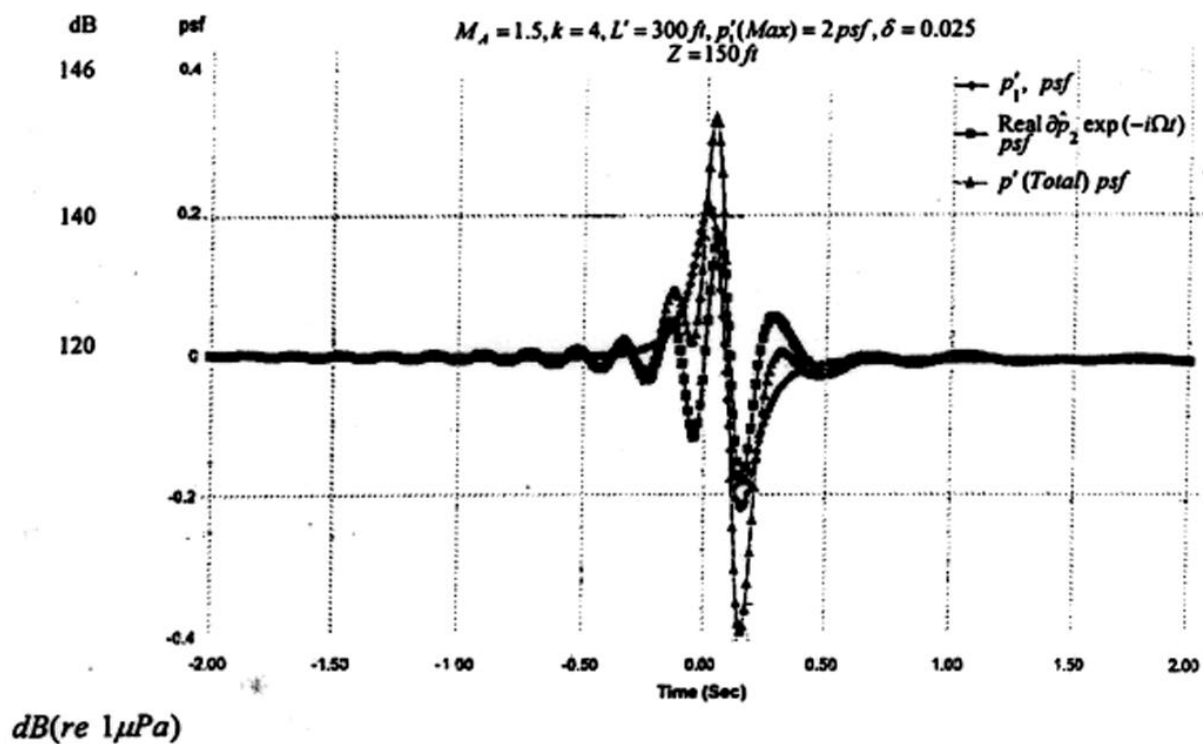


Fig. 17a

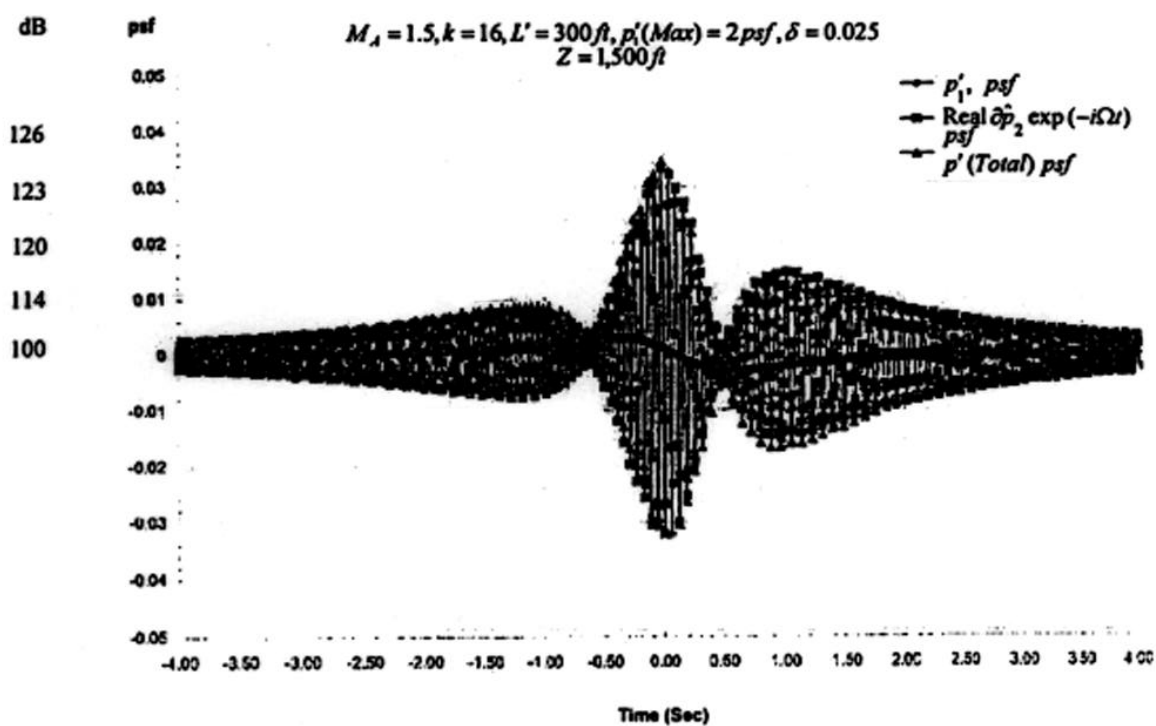
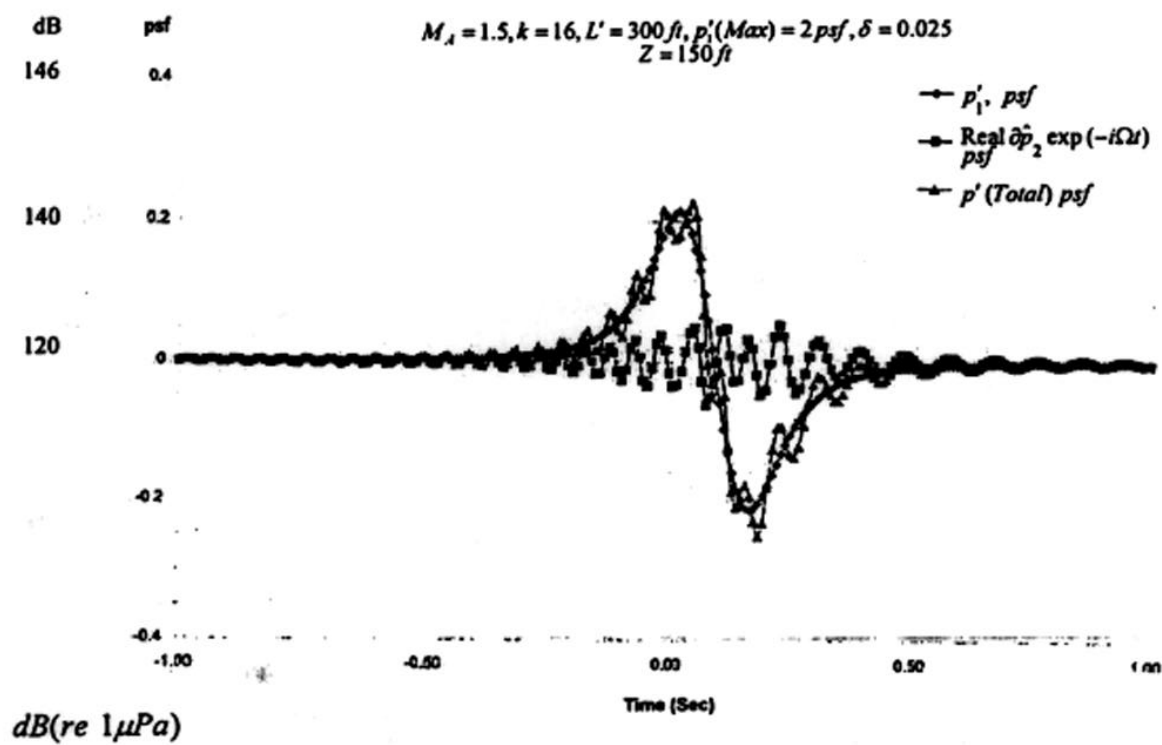
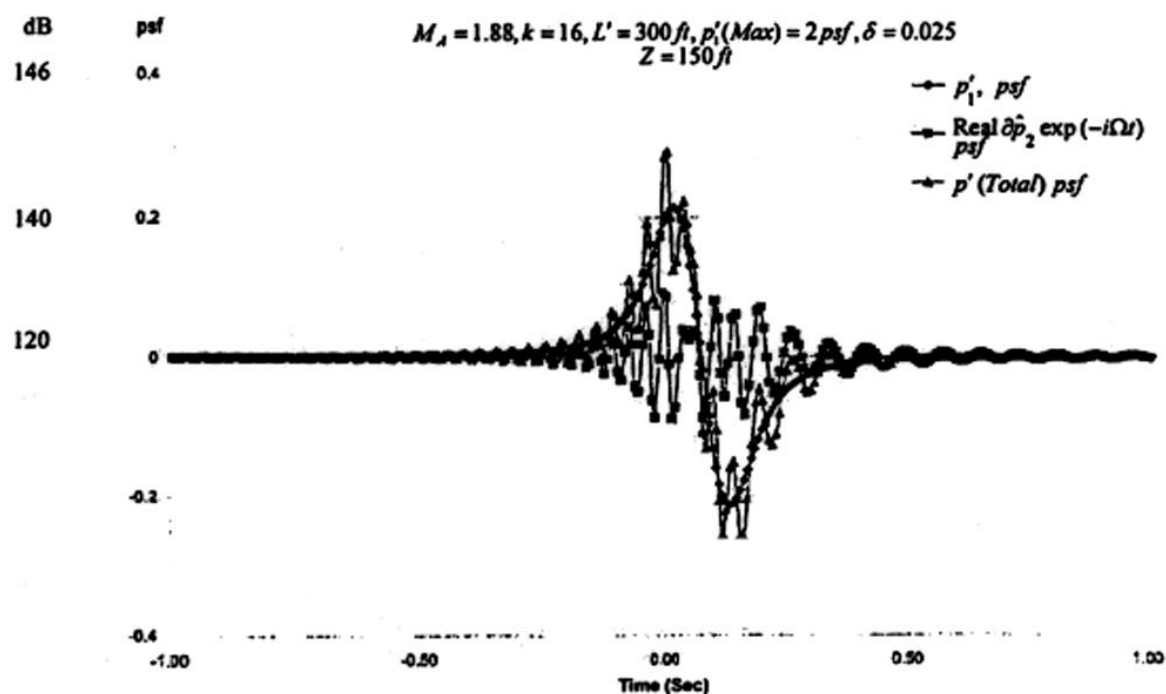


Fig. 17b





$\text{dB}(\text{re } 1 \mu\text{Pa})$

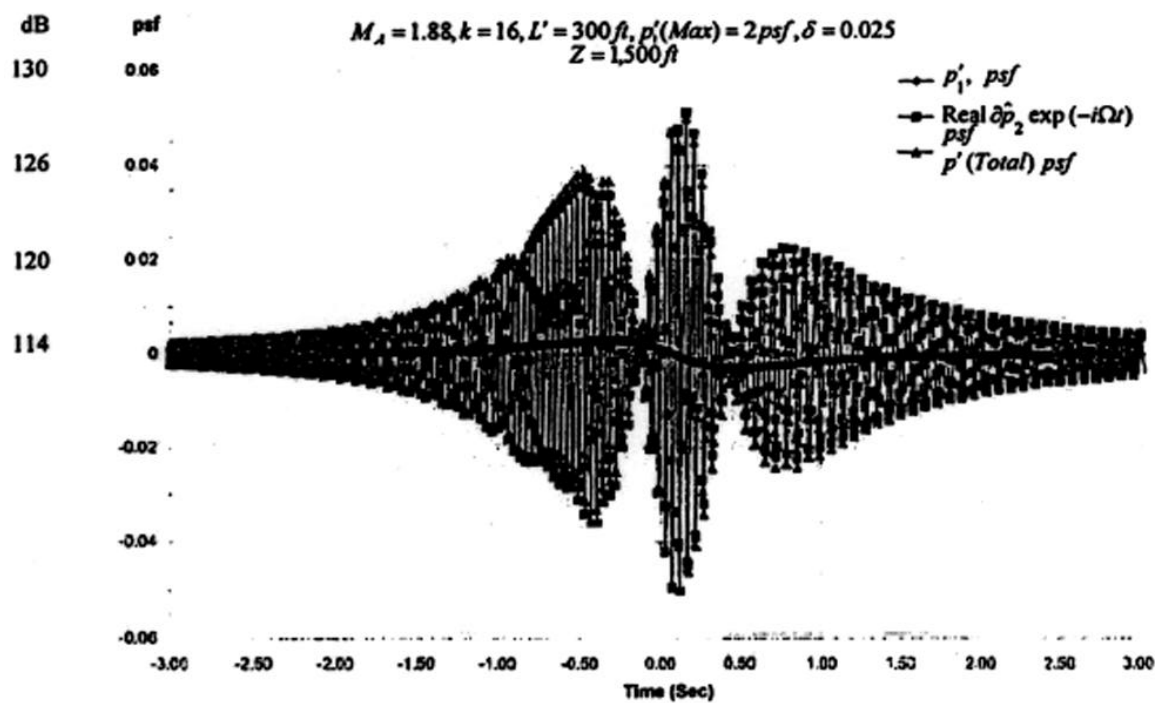


Fig. 18

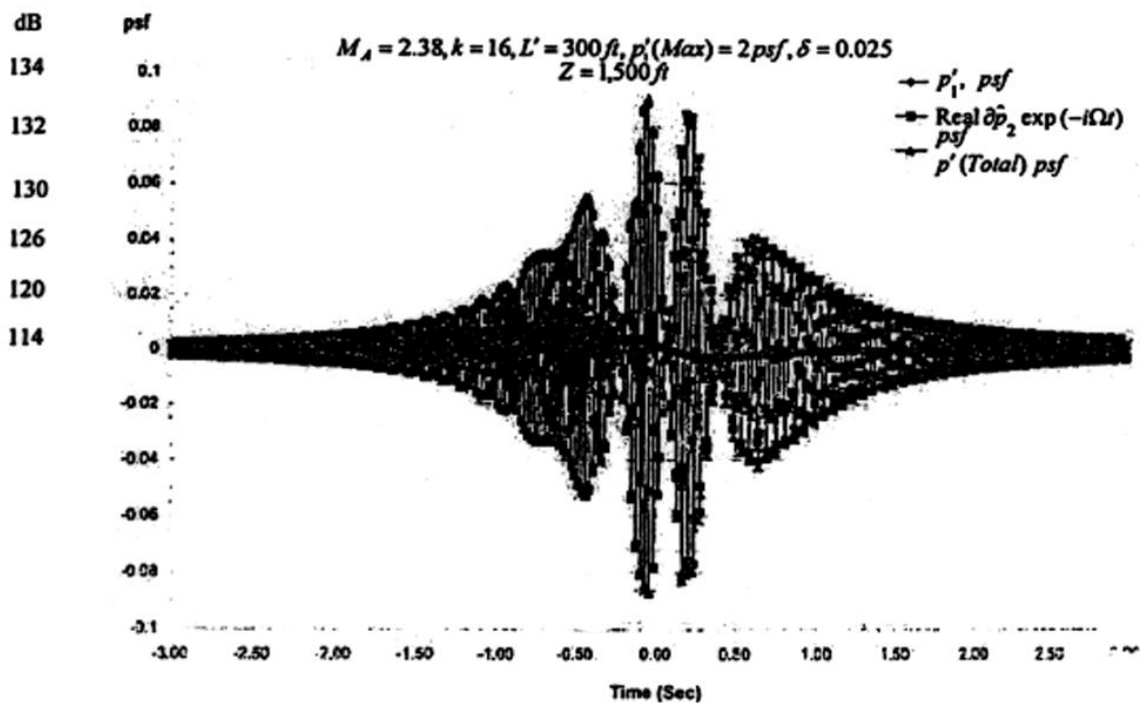
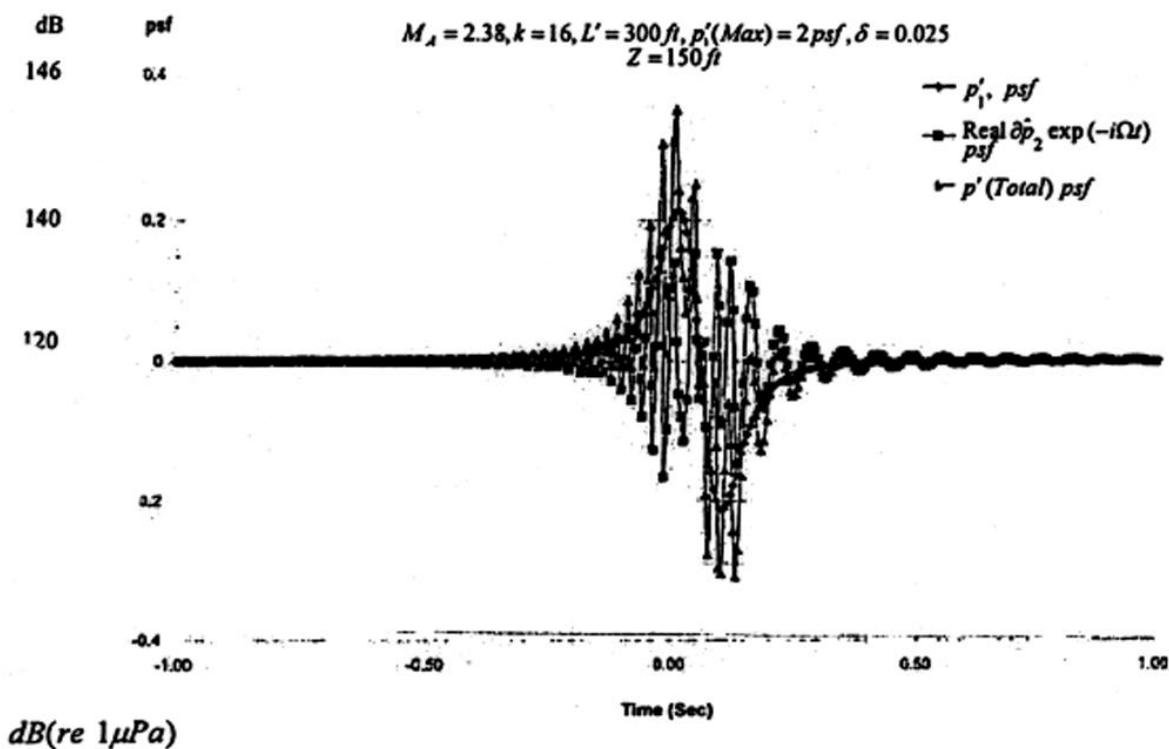


Fig. 19

$M=2.38, k=16.0$

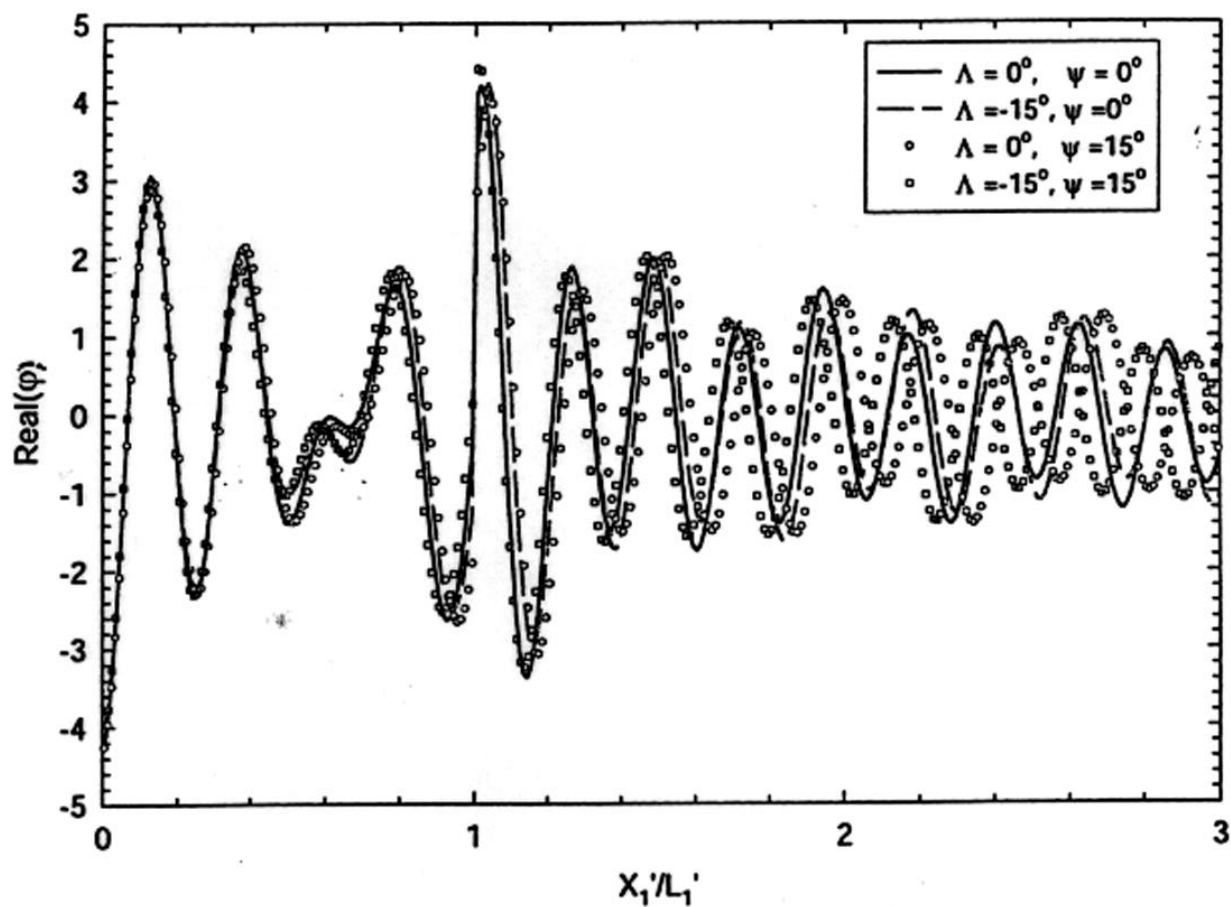
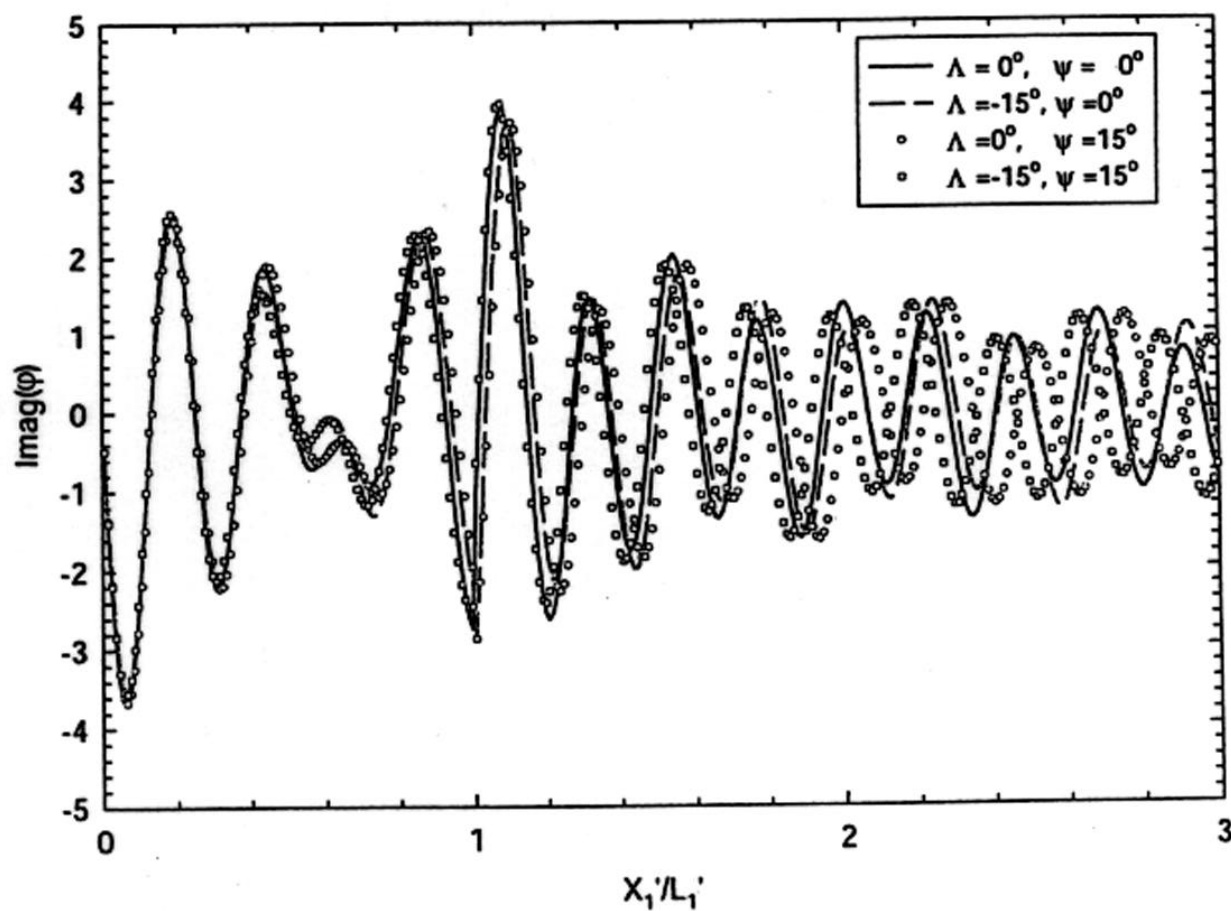


Fig. 20

$M=2.38, k=16.0$



$M=2.38, k=16.0$

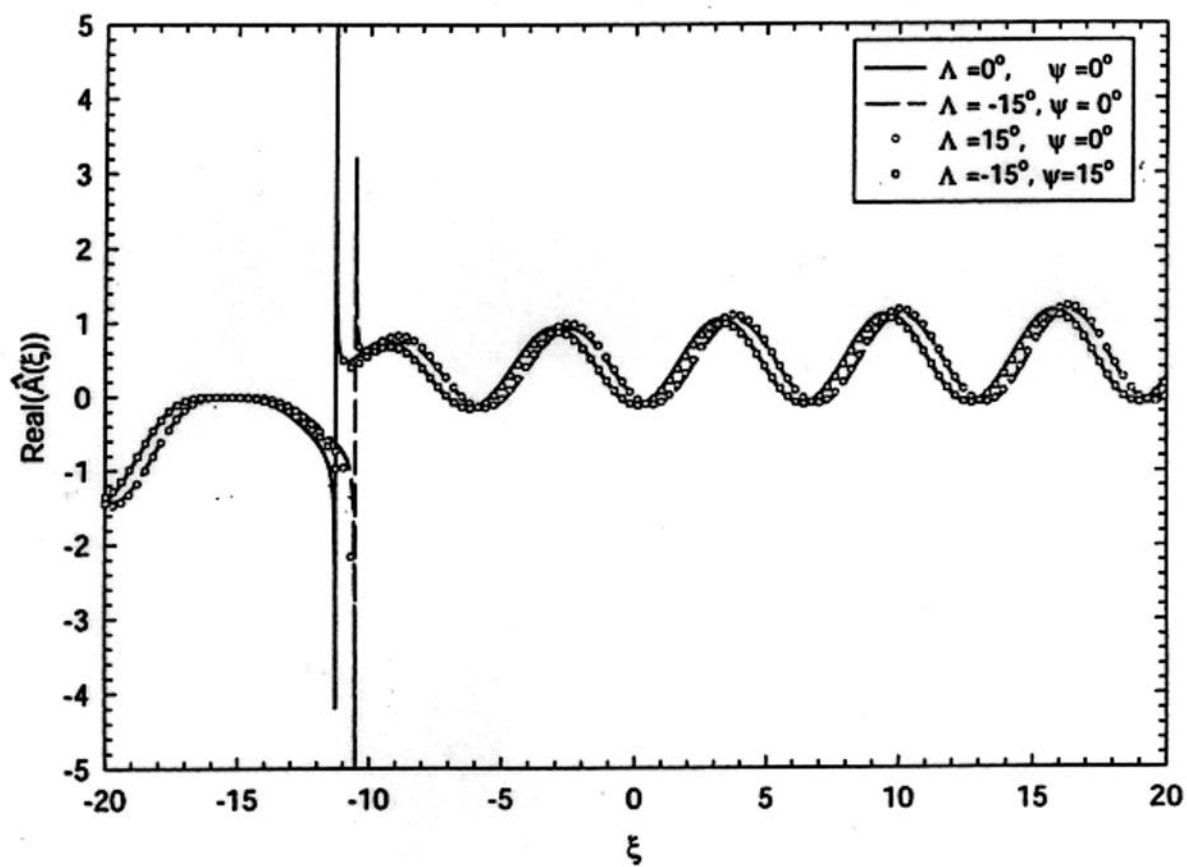
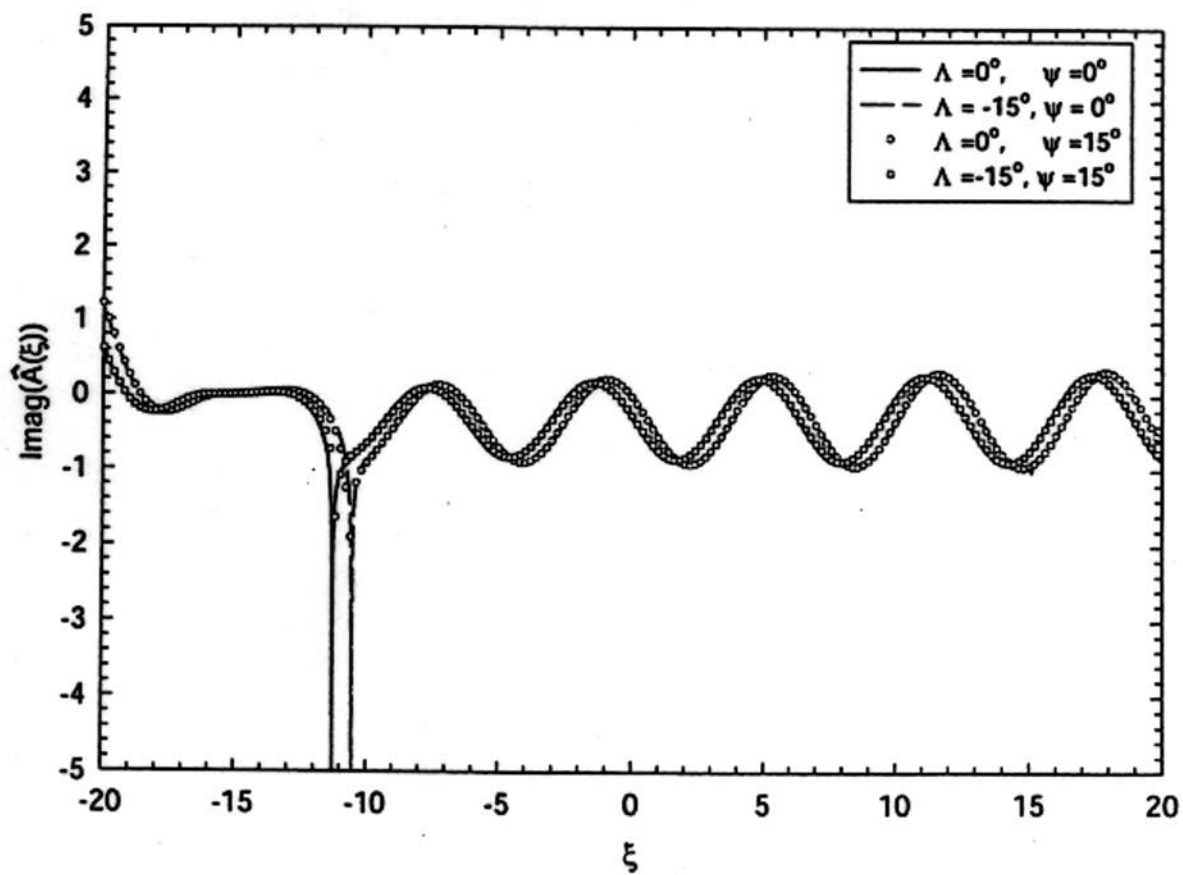


Fig. 21

$M=2.38, k=16.0$



$M=2.38, k=16.0$   
 $Z/L'=2.5$

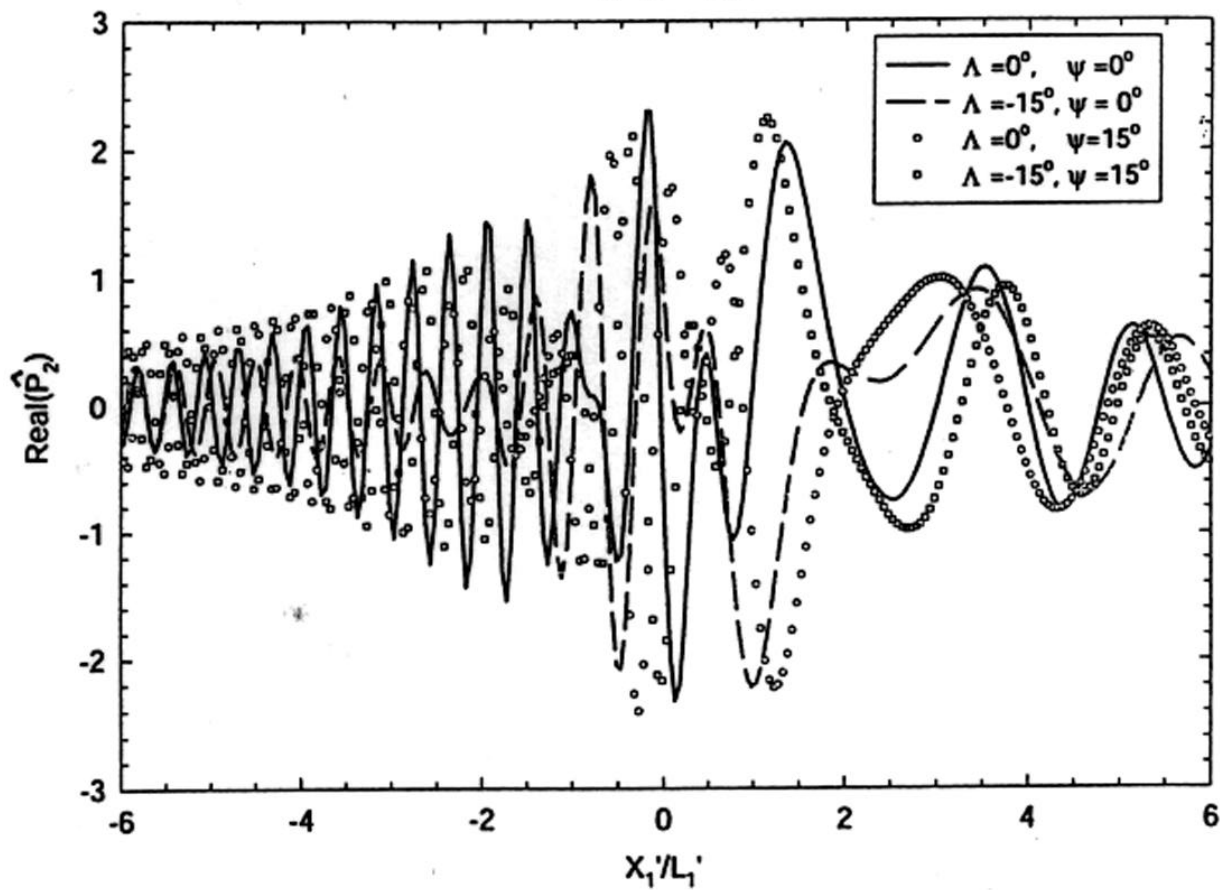
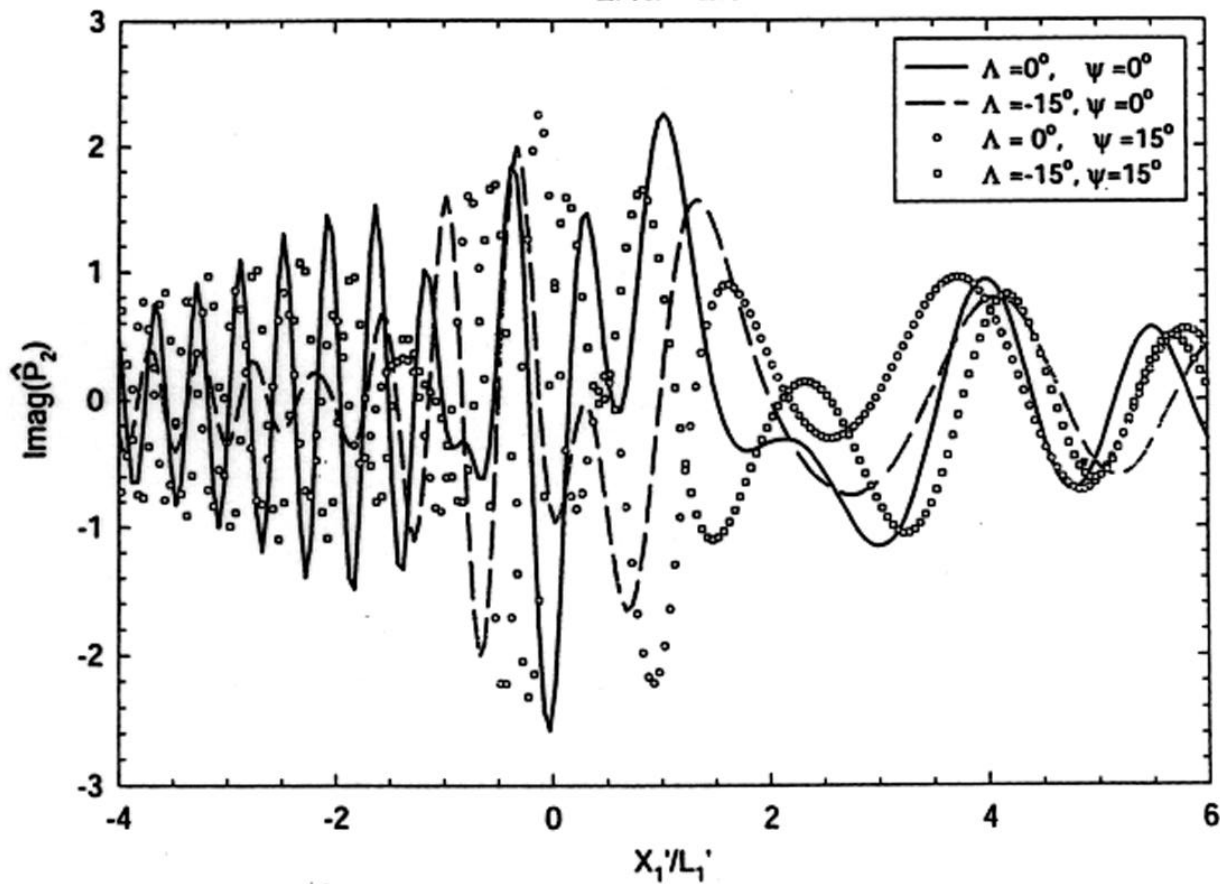


Fig. 22

$M=2.38, k=16.0$   
 $Z/L'=2.5$



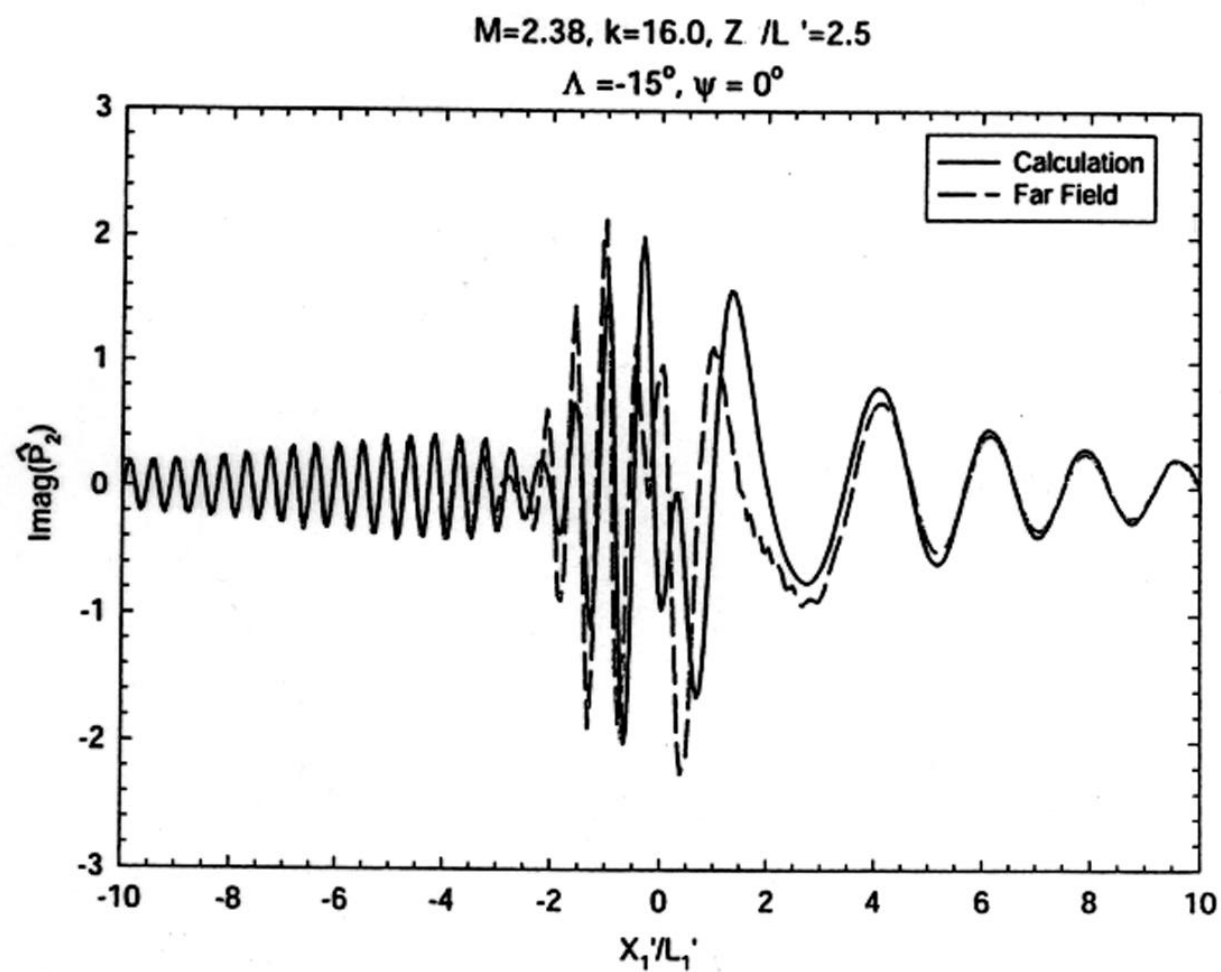
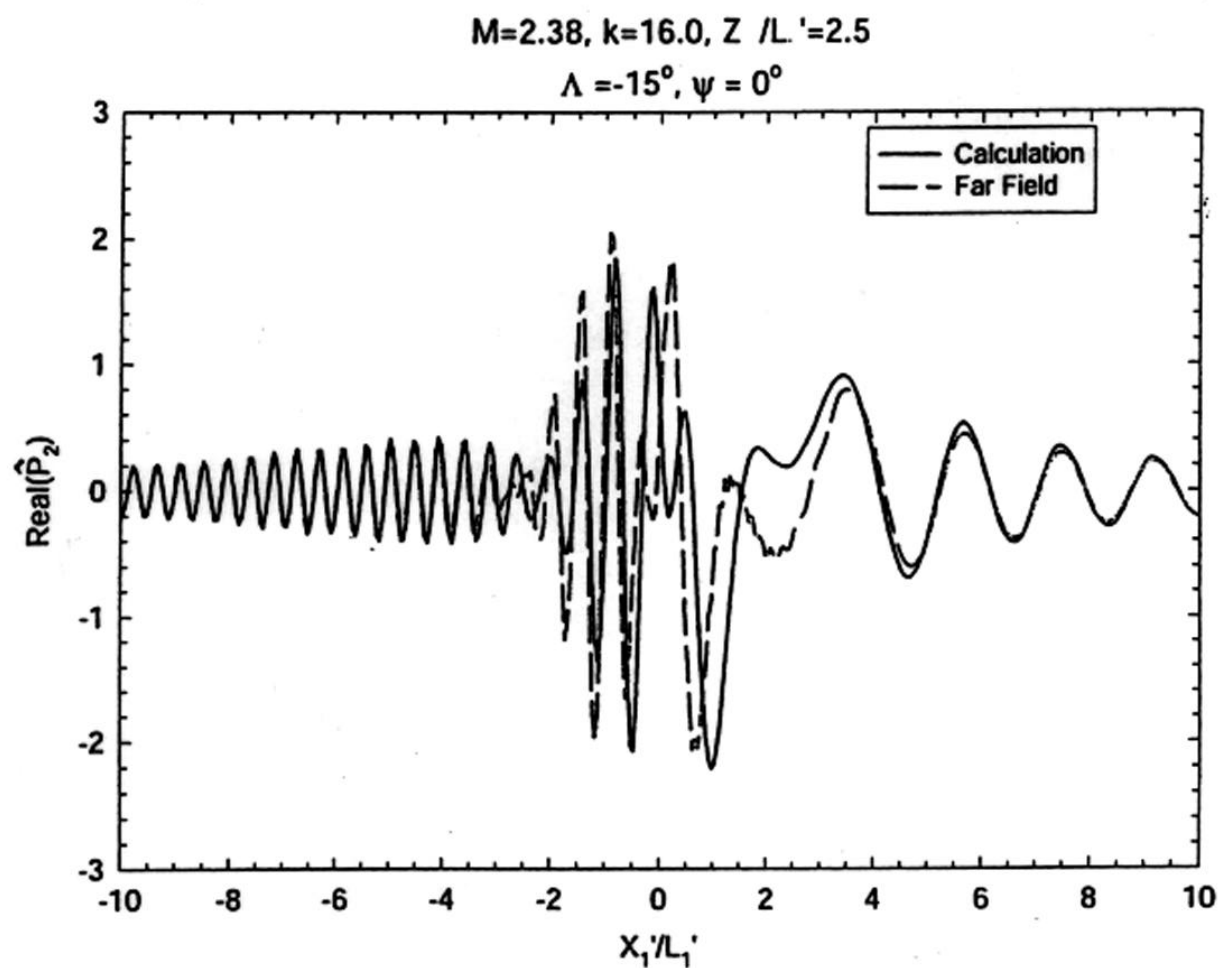


Fig. 23

$M=2.38, k=16.0$

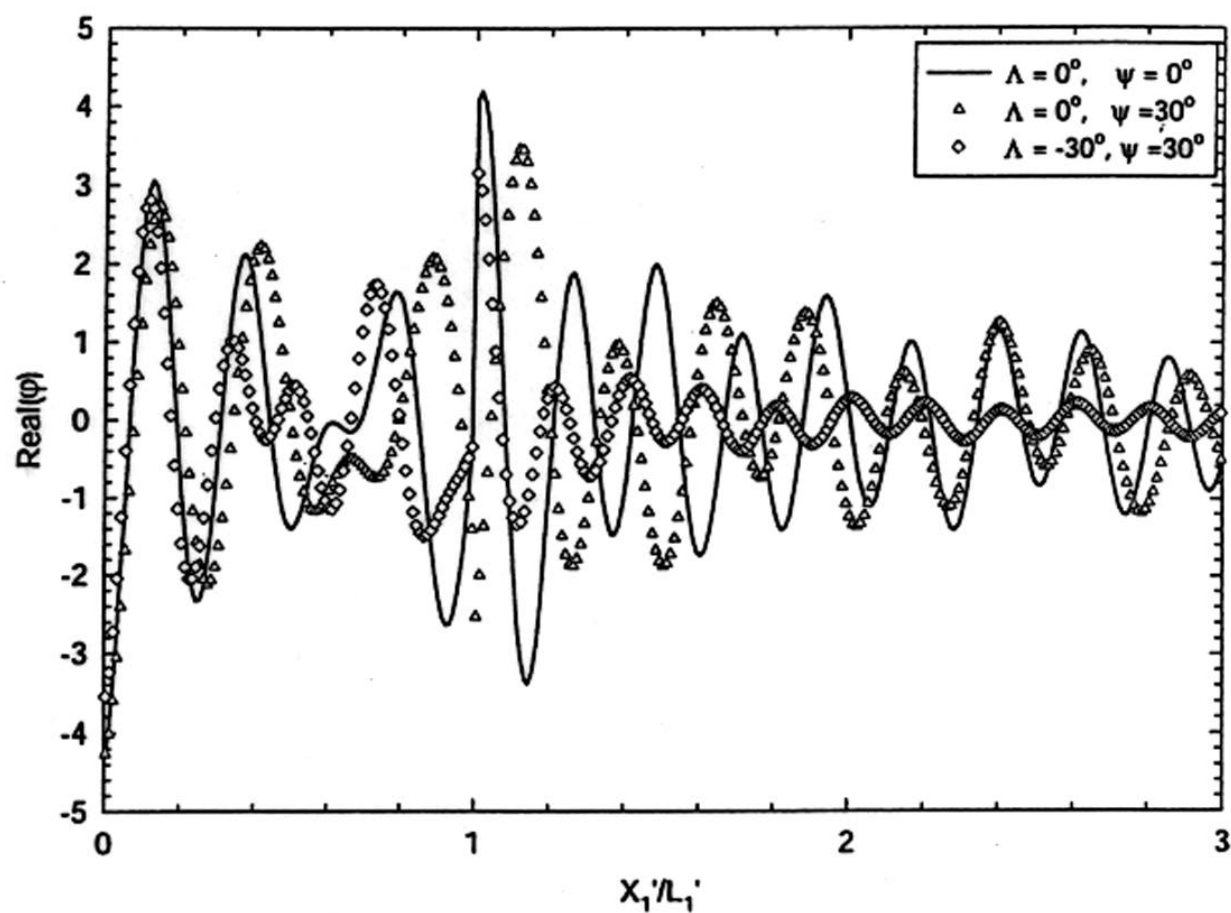
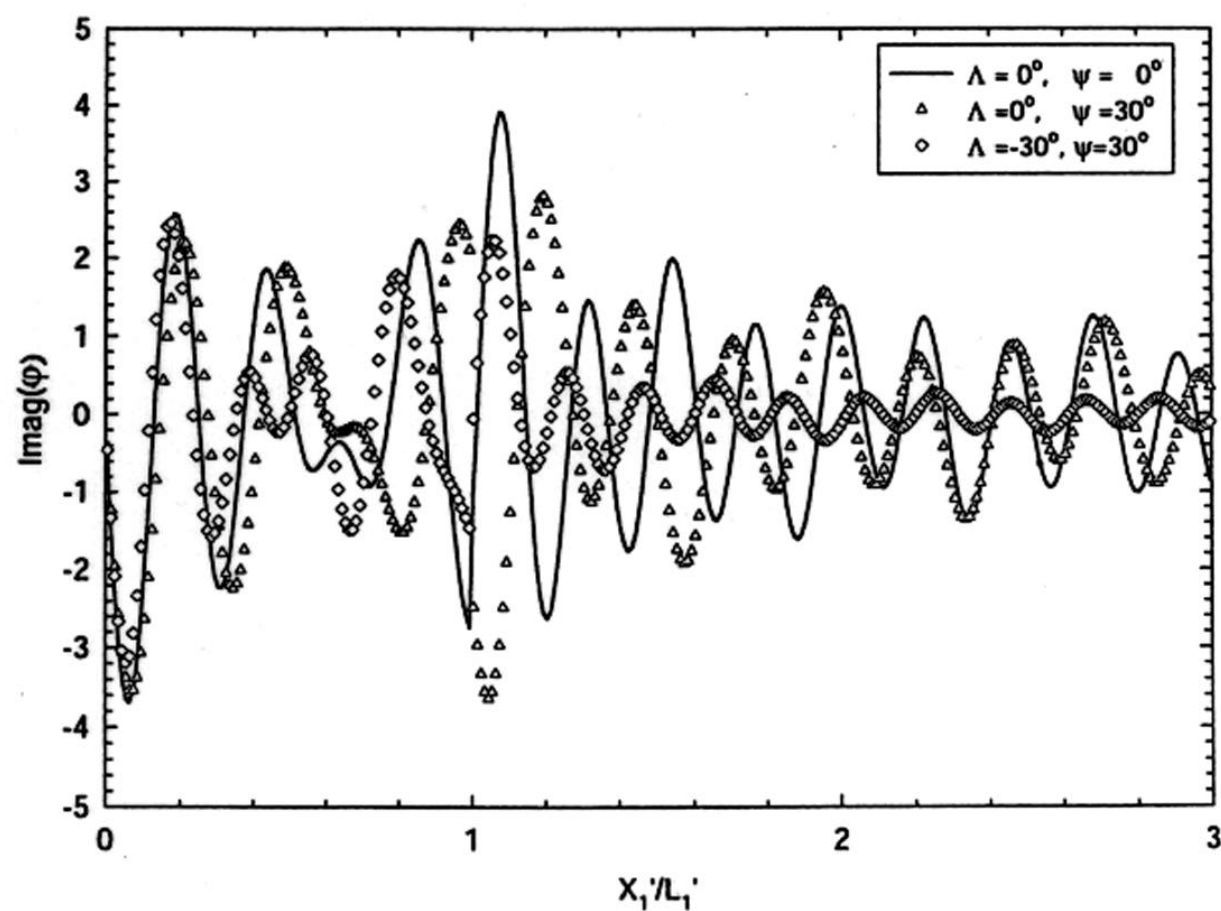


Fig. 24

$M=2.38, k=16.0$



$M=2.38, k=16.0$

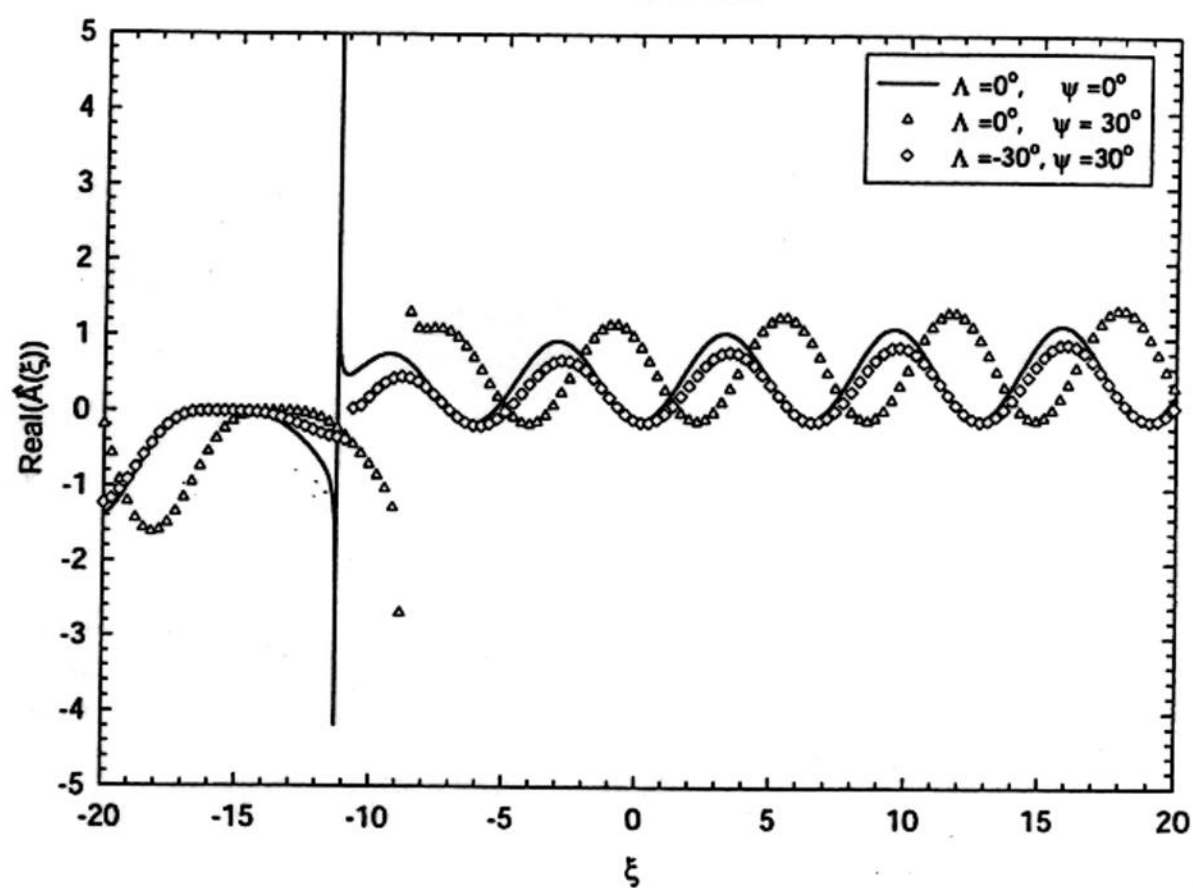
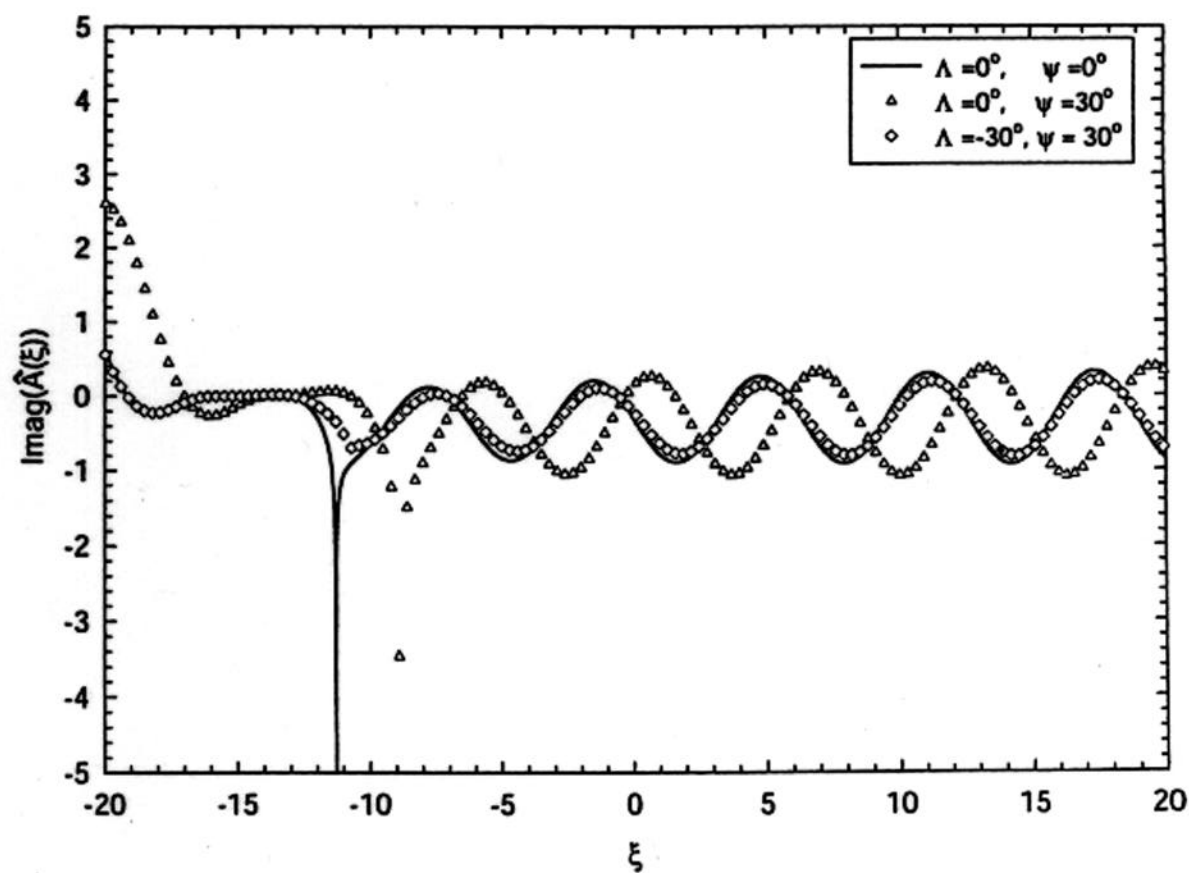


Fig. 25

$M=2.38, k=16.0$





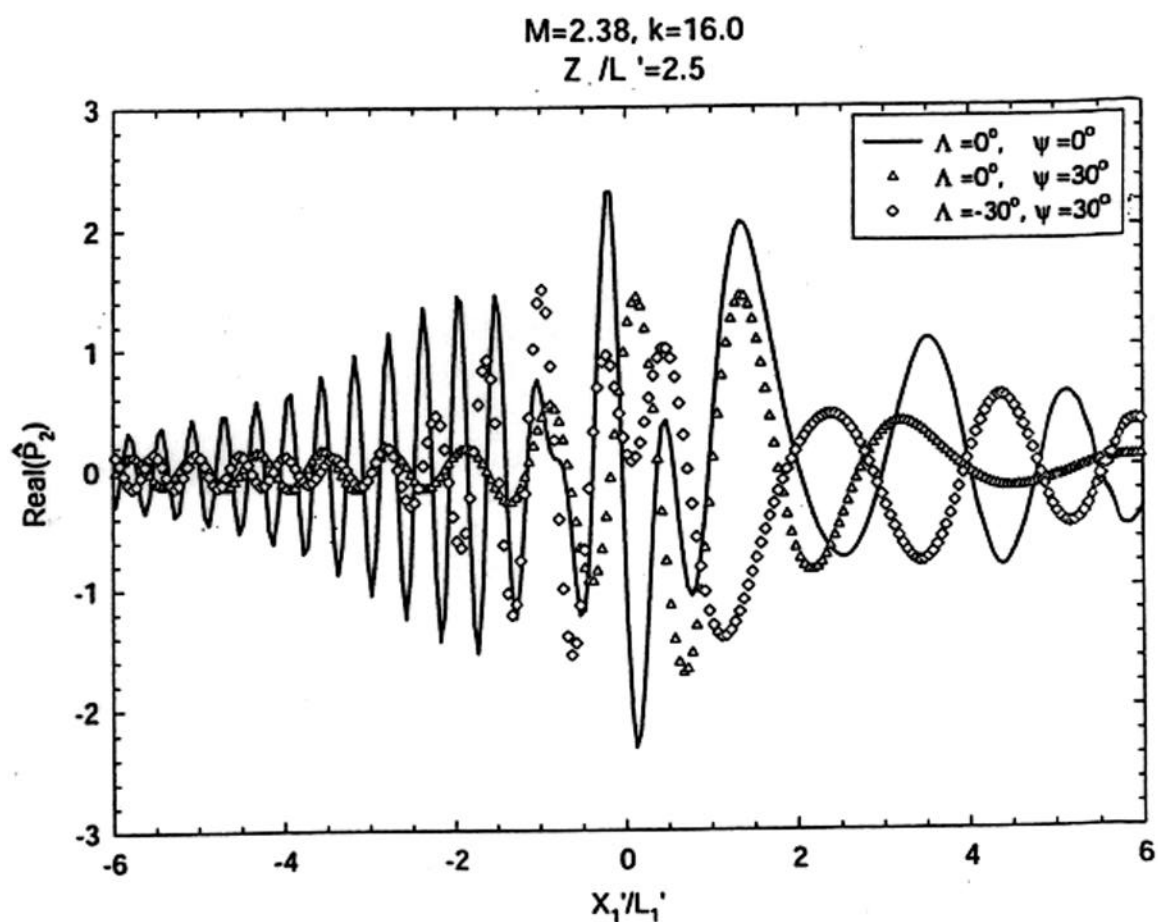
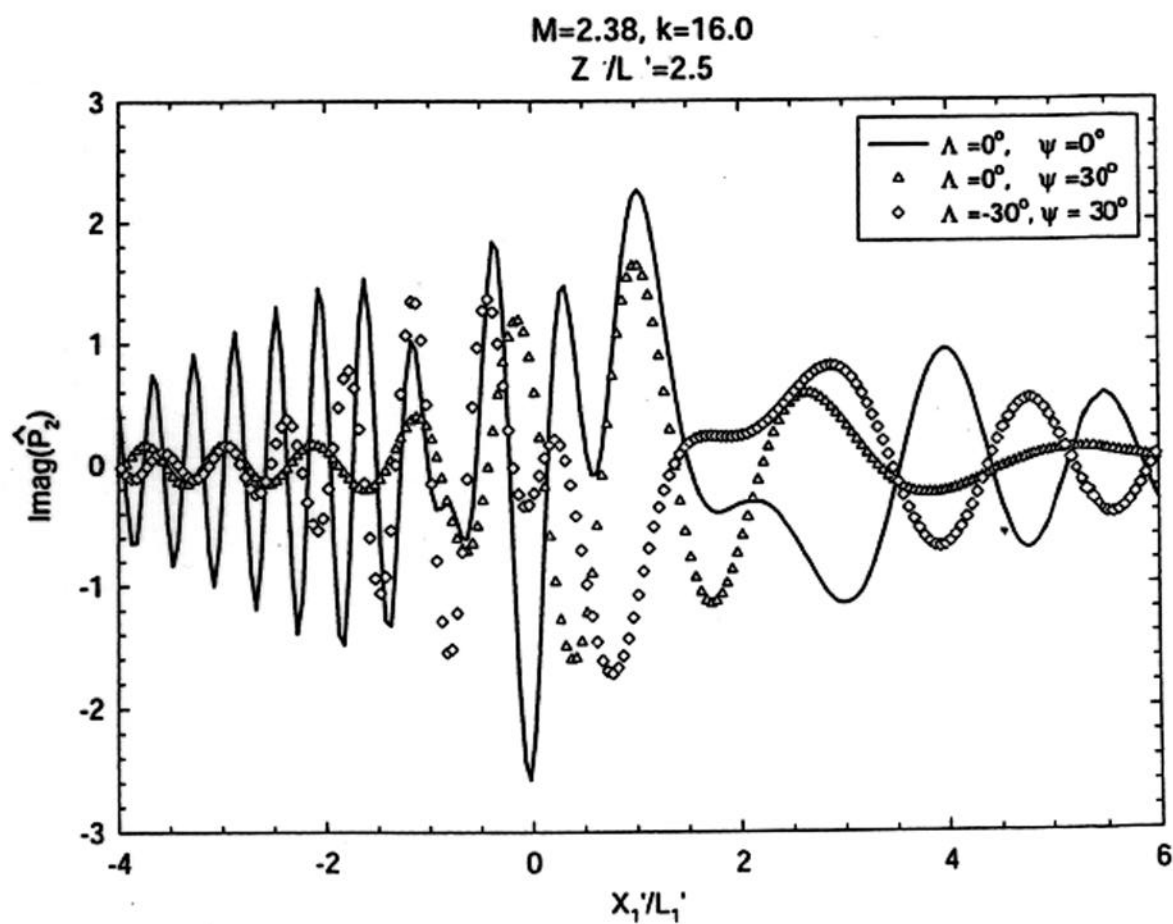


Fig. 26



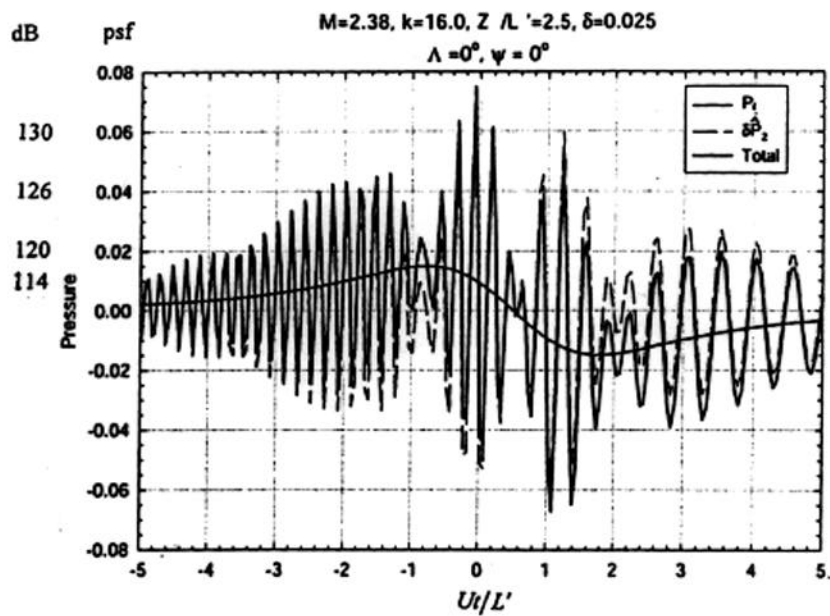


Fig. 26.Xa

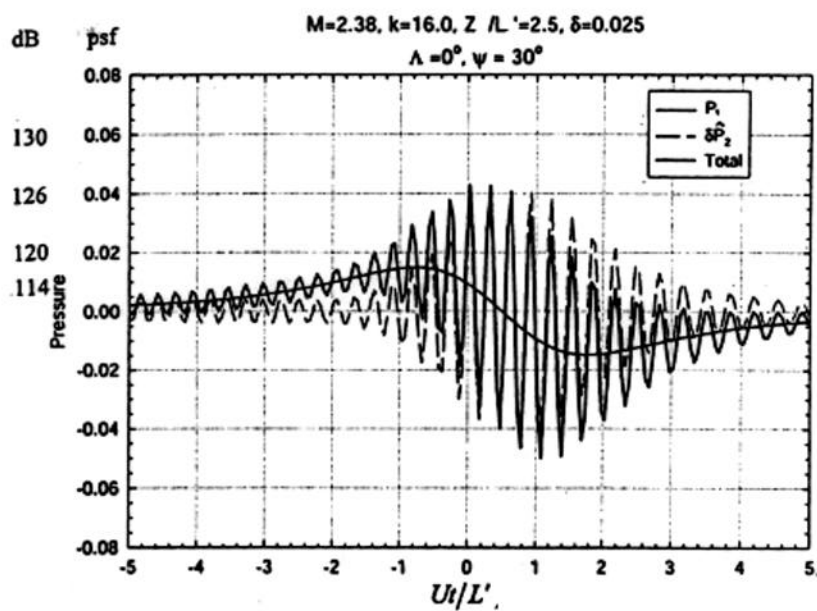


Fig. 26.Xb

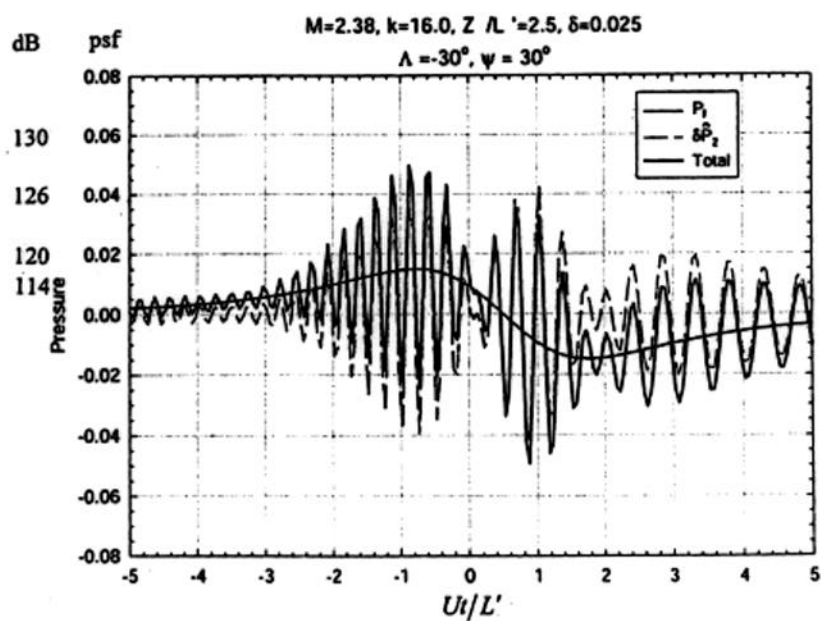


Fig. 26.Xc

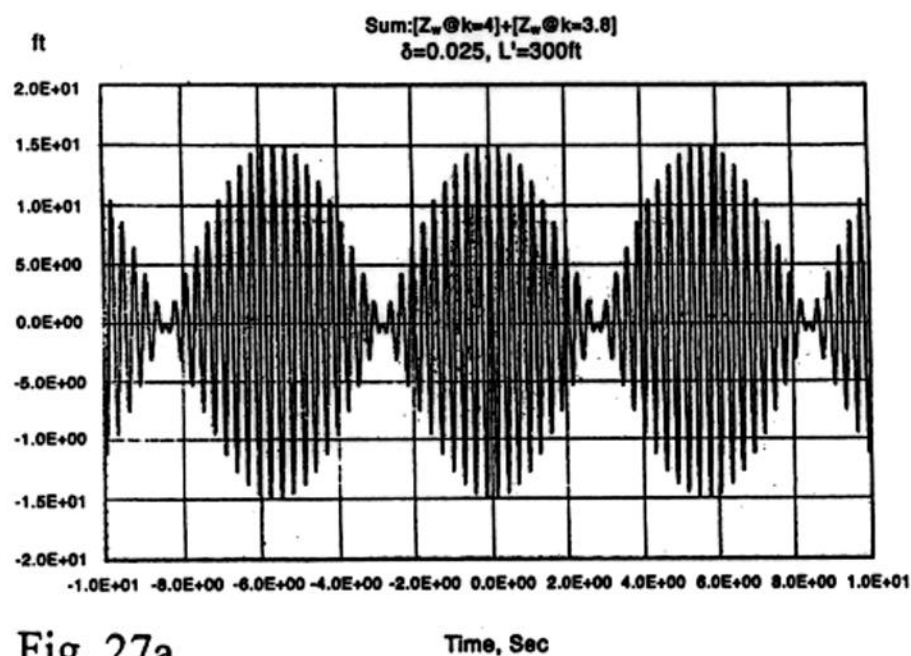


Fig. 27a

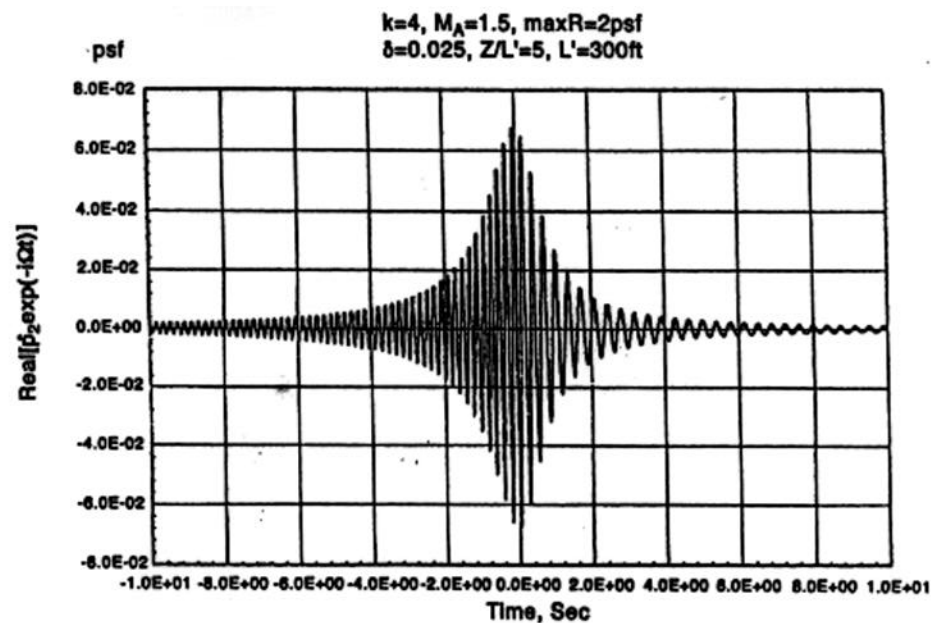


Fig. 27b

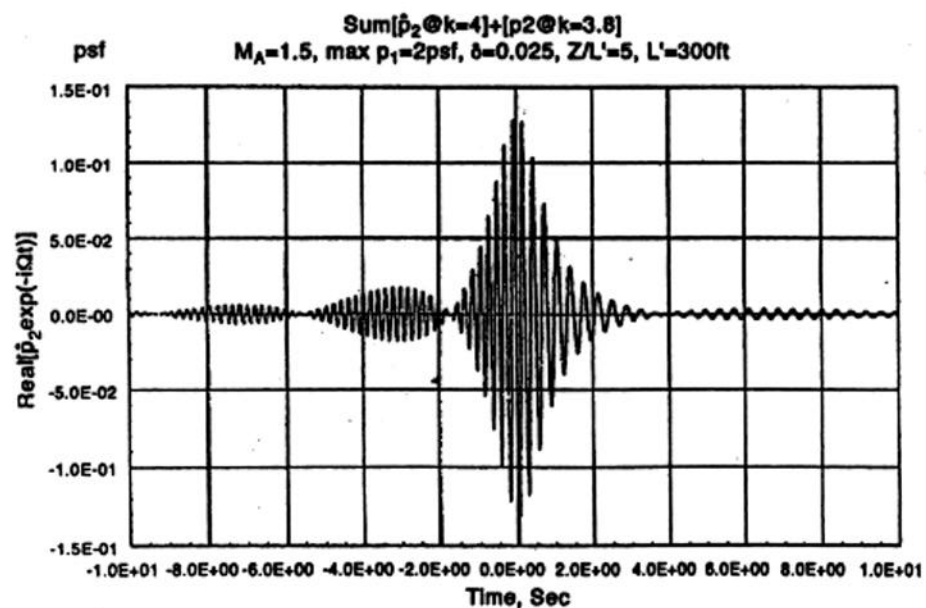


Fig. 27d

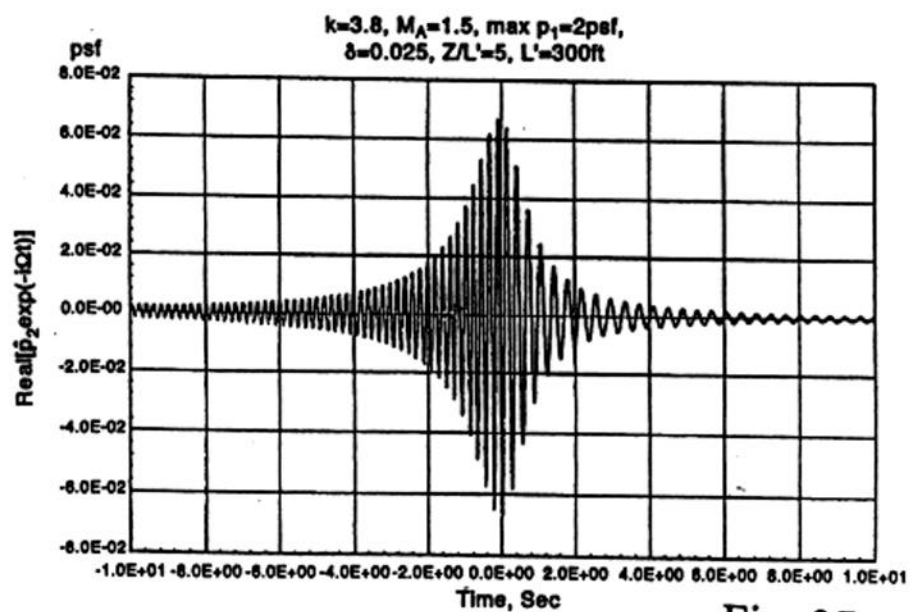


Fig. 27c

$M=2.38, k=16.0, Z_1'/L_1'=2.5, \delta=0.025, \Lambda=0^\circ, \psi=30^\circ, 0^\circ.$

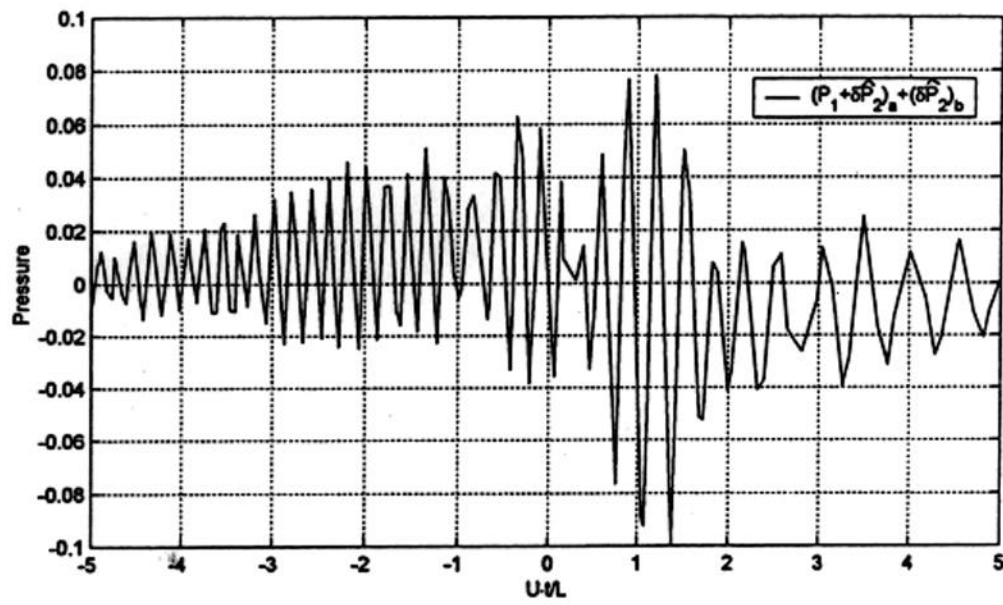


Fig. 28a

$M=2.38, k=16.0, Z_1'/L_1'=2.5, \delta=0.025, \Lambda=0^\circ, \psi=30^\circ, -30^\circ.$

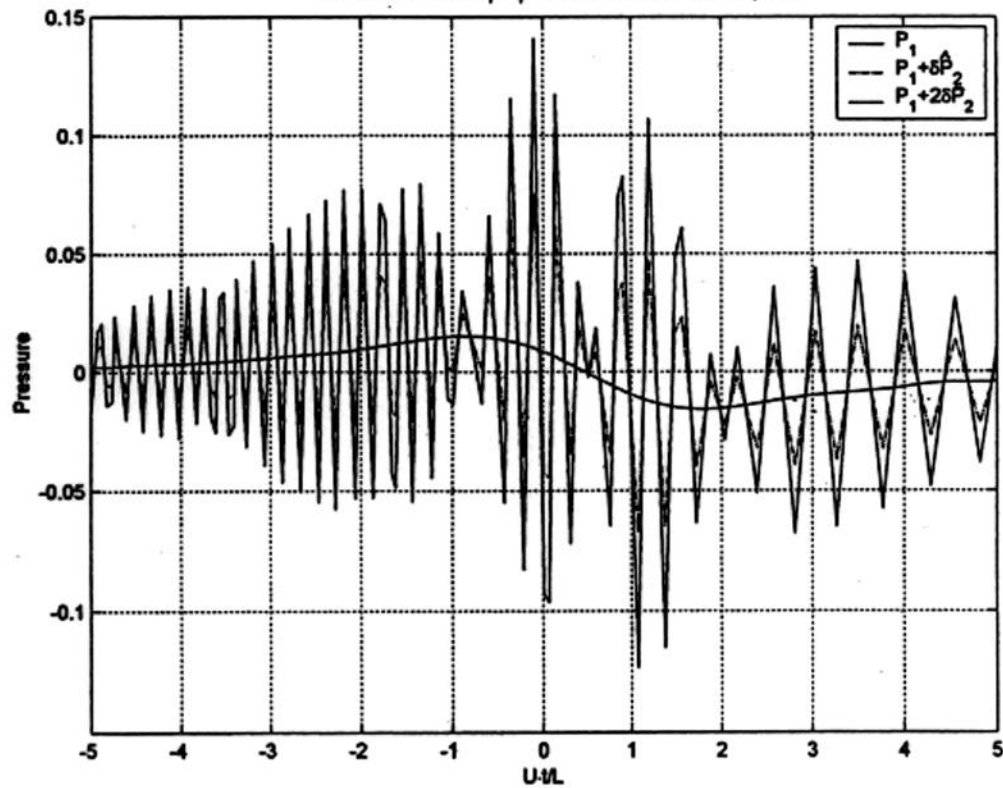
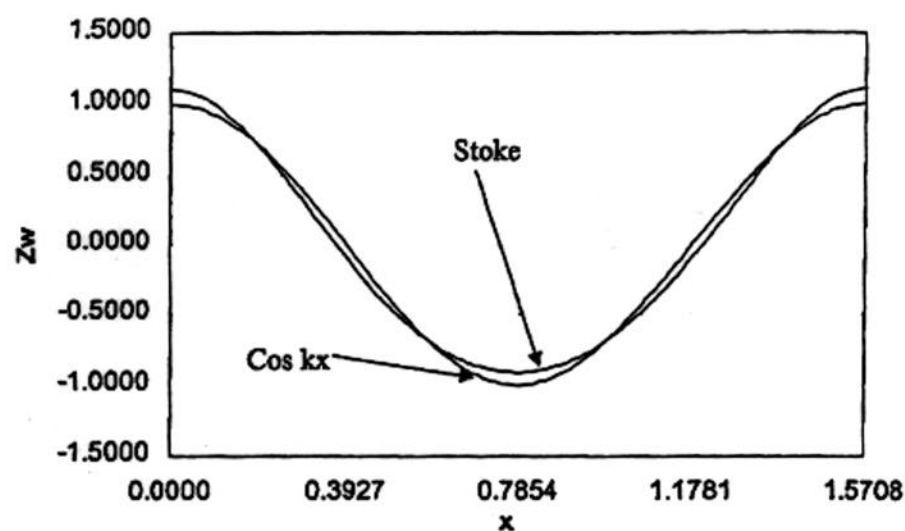


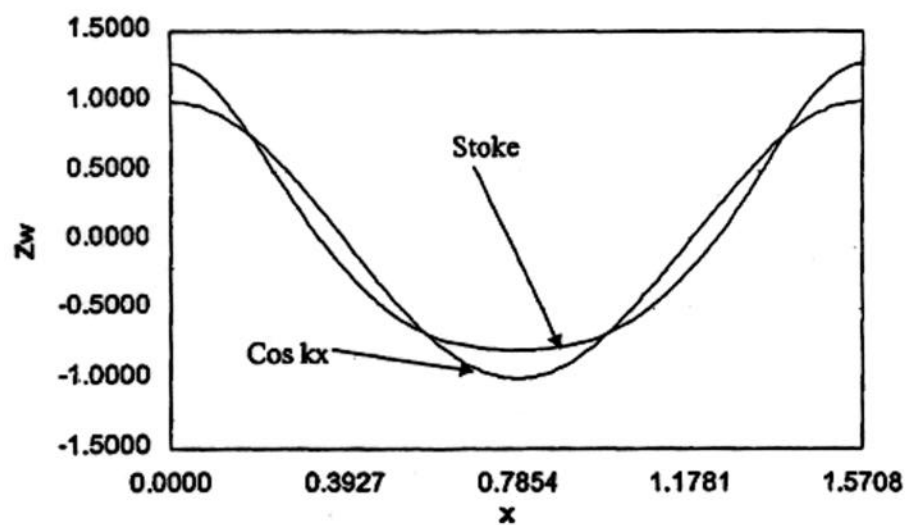
Fig. 28b

Wave Shape,  $k=4$ ,  $\delta=0.025$

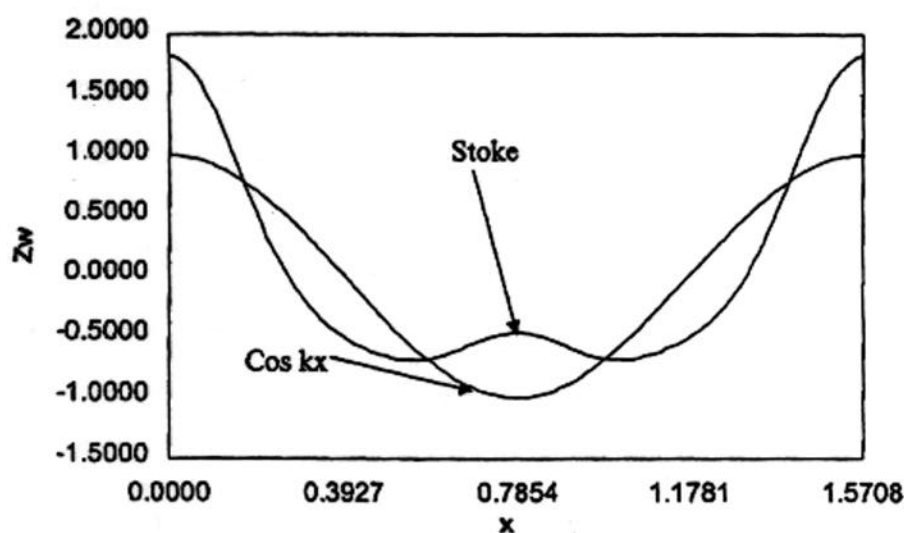
Fig. 29



Wave Shape,  $k=4$ ,  $\delta=0.05$



Wave Shape,  $k=4$ ,  $\delta=0.1$



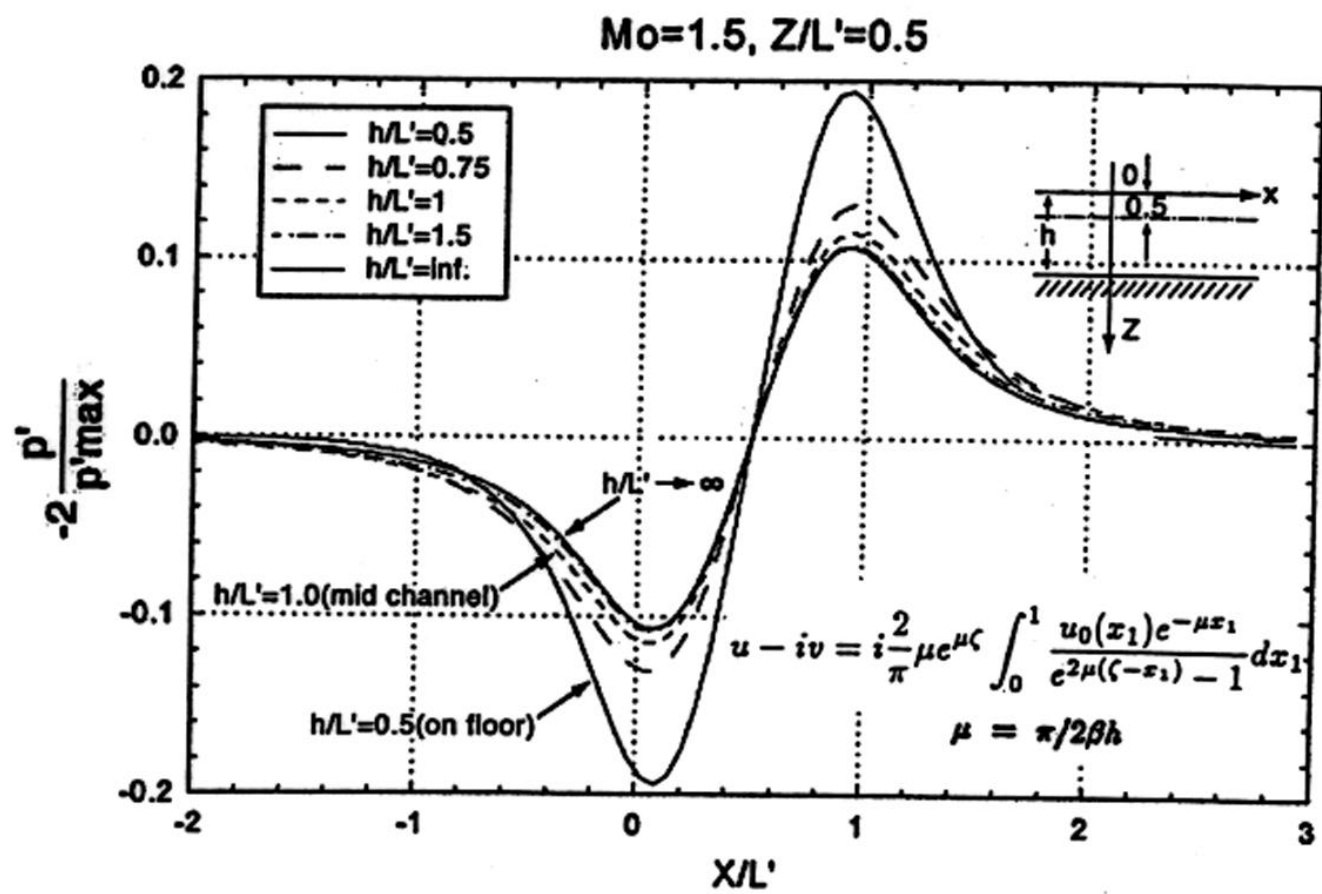


Fig. 30

Fig. 31

$$\rho_1=1 \quad \rho_2=1.91$$

$$c_1=1500 \quad c_a=331 \quad c_p=1711 \quad \underline{c_s=503}$$

$$m_1=0.331 \quad m_p=0.290 \quad m_s=0.987$$

$$\beta_1=0.944 \quad \beta_p=0.957 \quad \beta_s=0.160$$

$$D_{BW}=-15.409$$

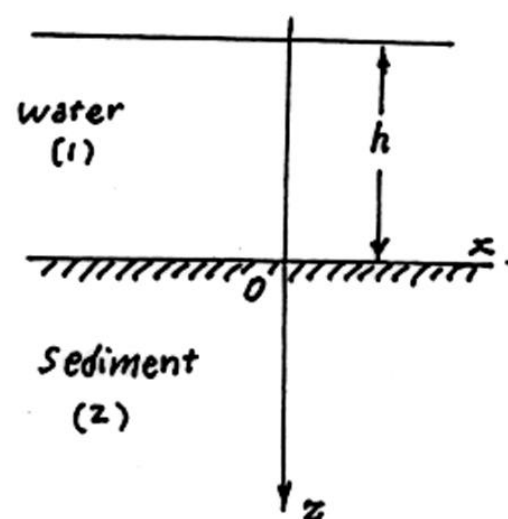
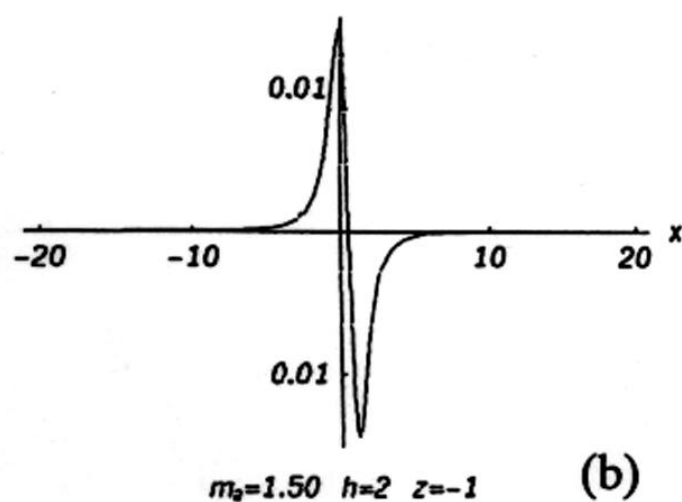
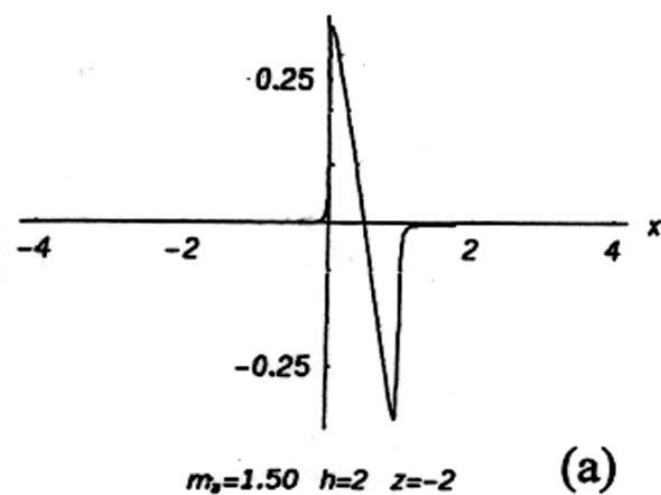


Fig. 32

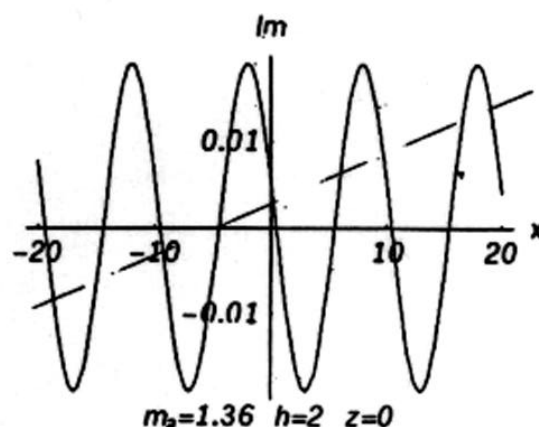
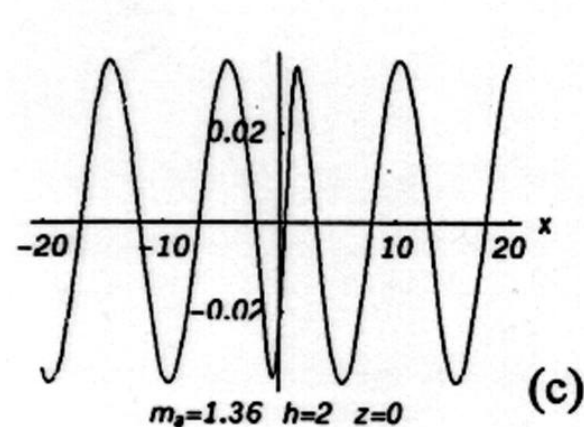
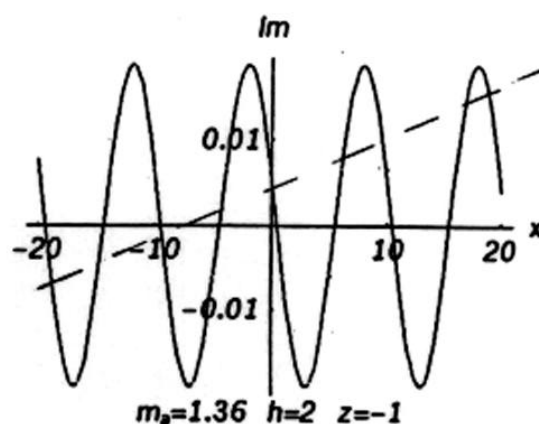
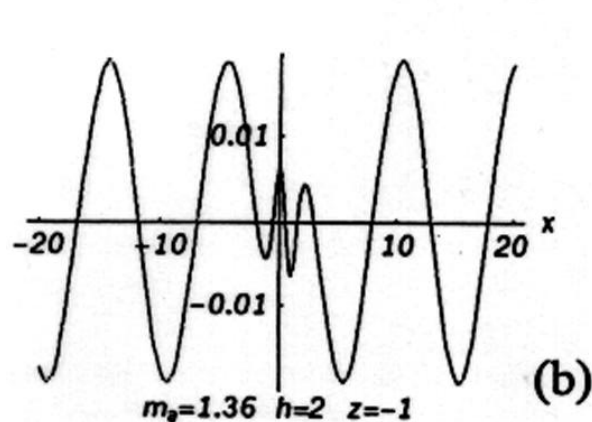
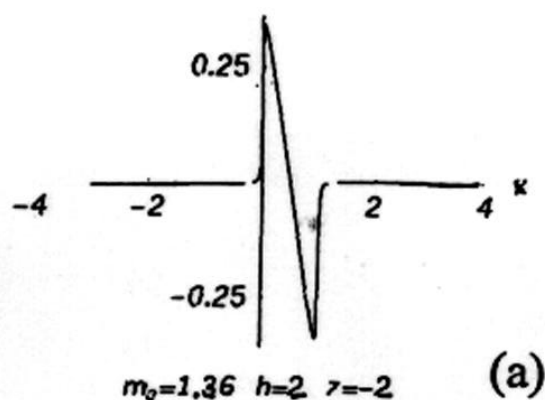
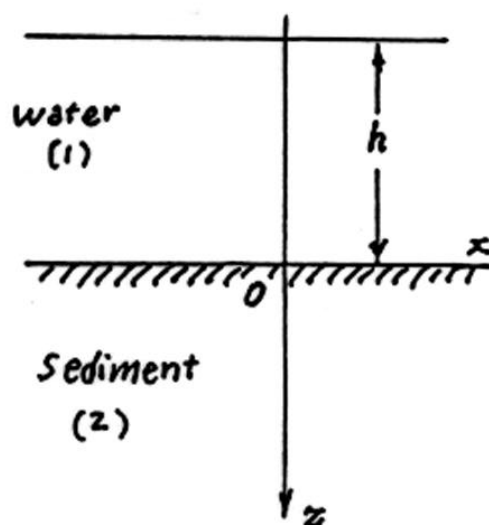
$$\rho_1=1 \quad \rho_2=1.91$$

$$c_1=1500 \quad c_a=331 \quad c_p=1711 \quad c_s=503$$

$$m_1=0.300 \quad m_p=0.263 \quad m_s=0.895$$

$$\beta_1=0.954 \quad \beta_p=0.965 \quad \beta_s=0.446$$

$$D_{BW}=-1.09$$





$$\rho_1=1 \quad \rho_2=1.91$$

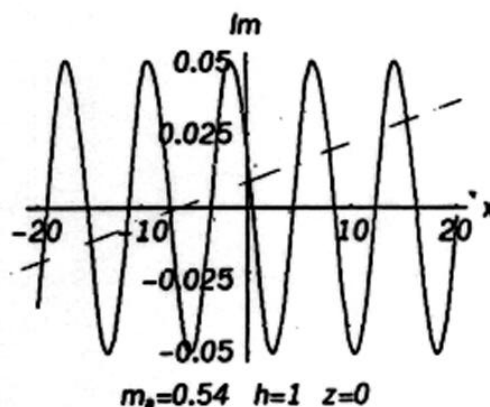
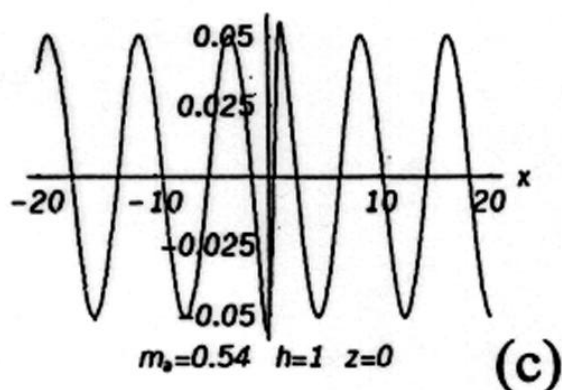
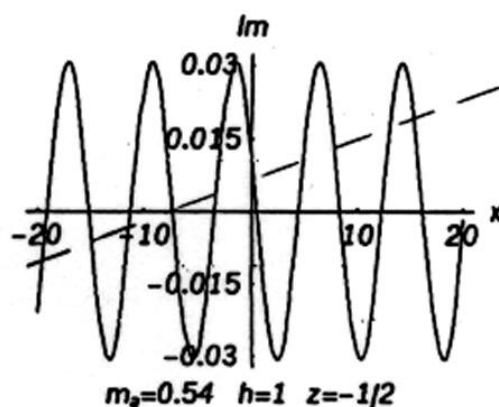
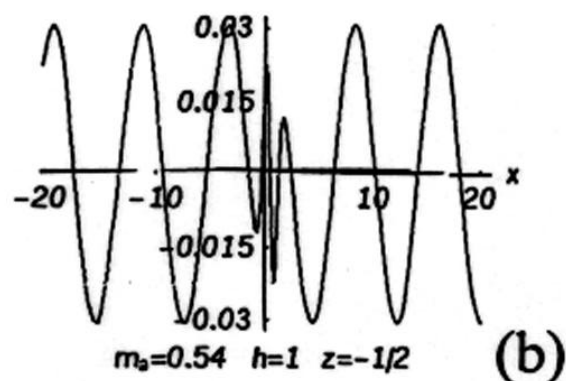
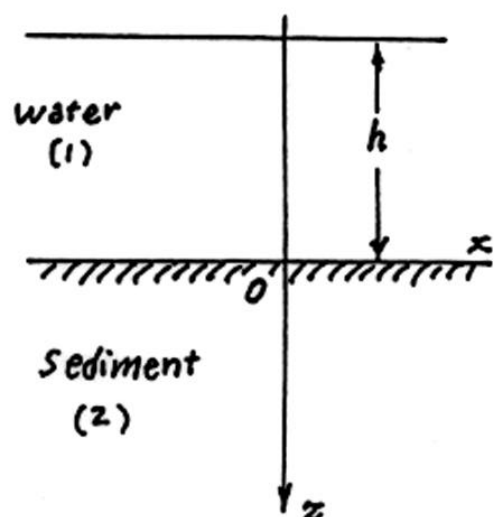
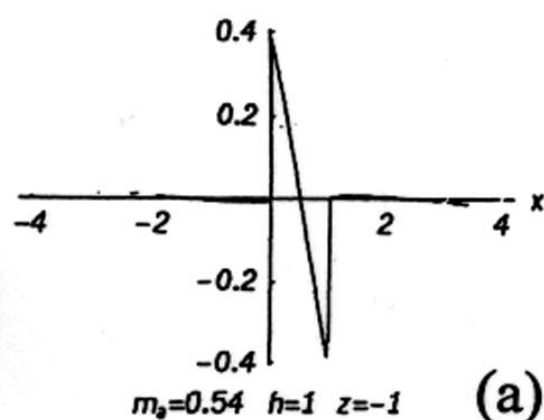
$$c_1=1500 \quad c_a=331 \quad c_p=1711 \quad \underline{c_s=195}$$

$$m_1=0.119 \quad m_p=0.104 \quad m_s=0.917$$

$$\beta_1=0.993 \quad \beta_p=0.995 \quad \beta_s=0.400$$

$$D_{BW}=-1.20$$

Fig. 33



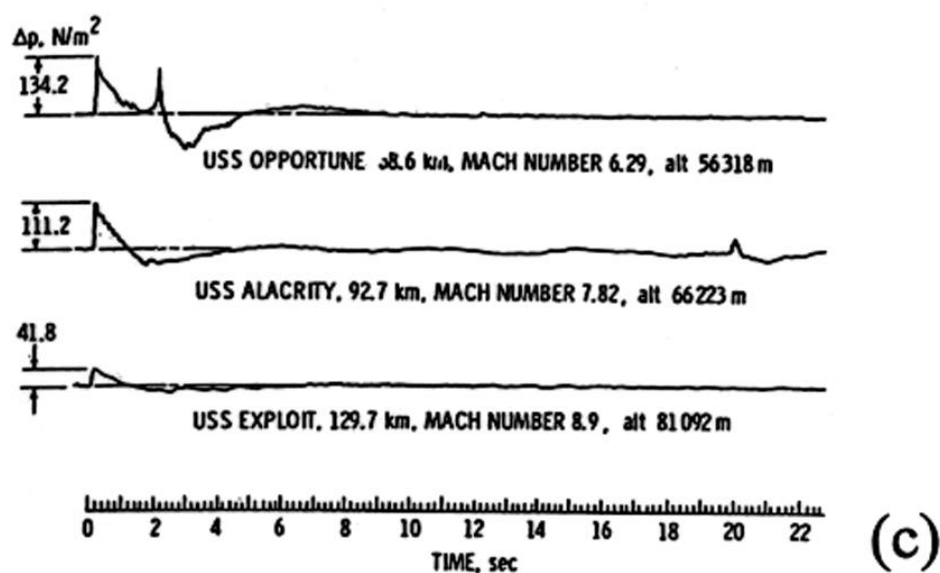
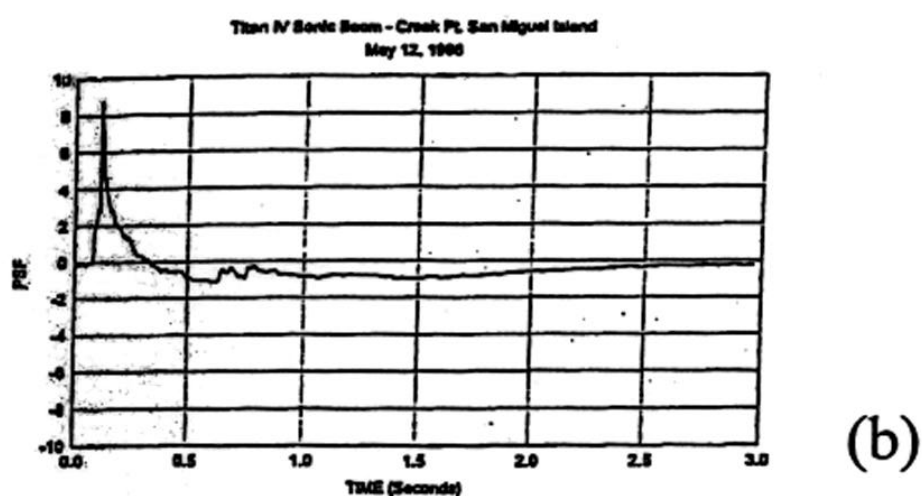
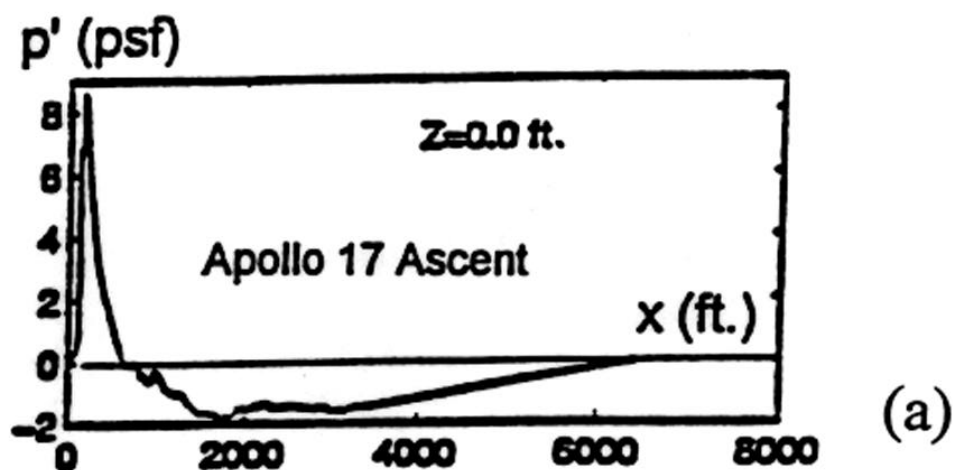


Fig. 34

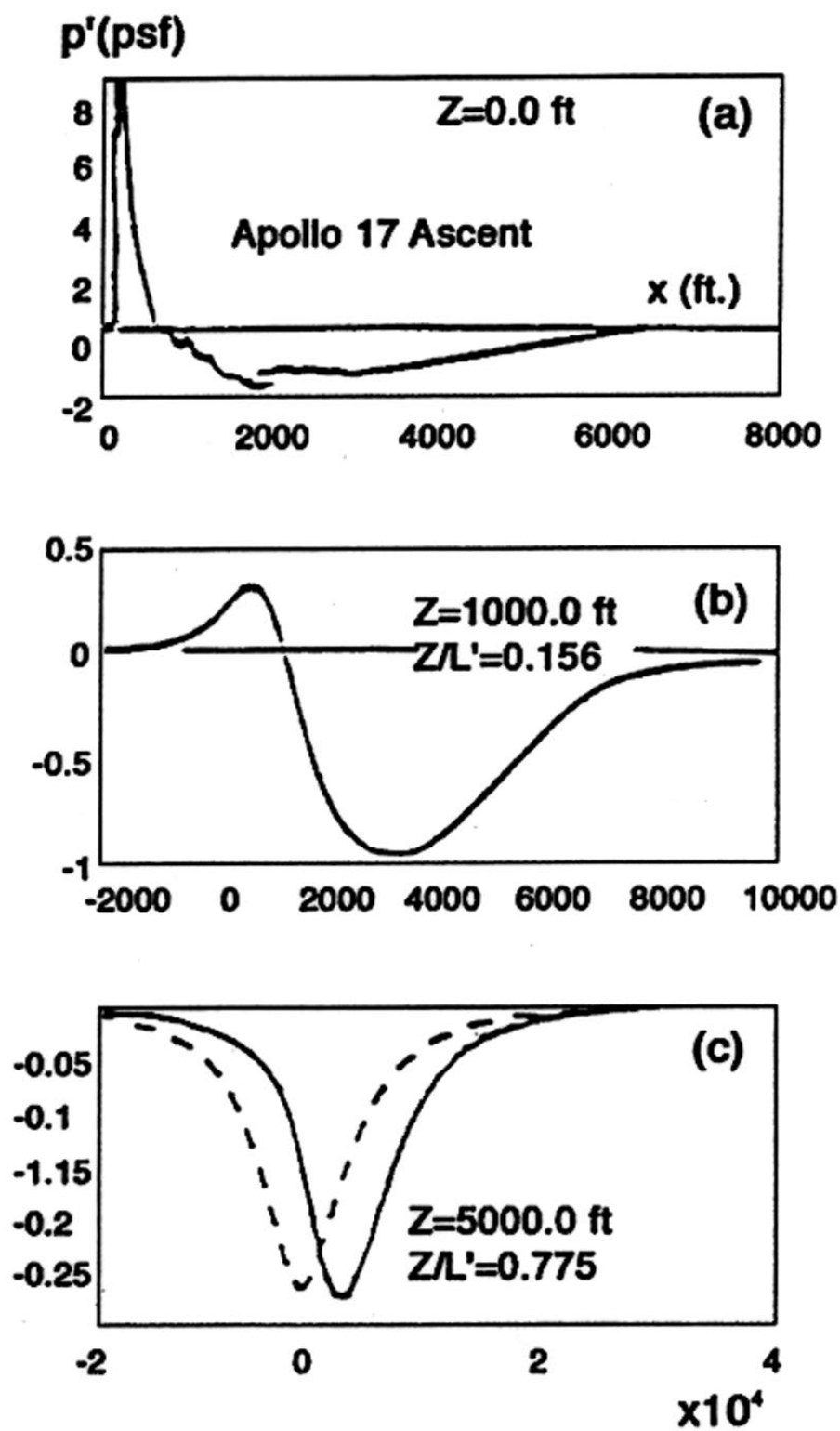


Fig. 35

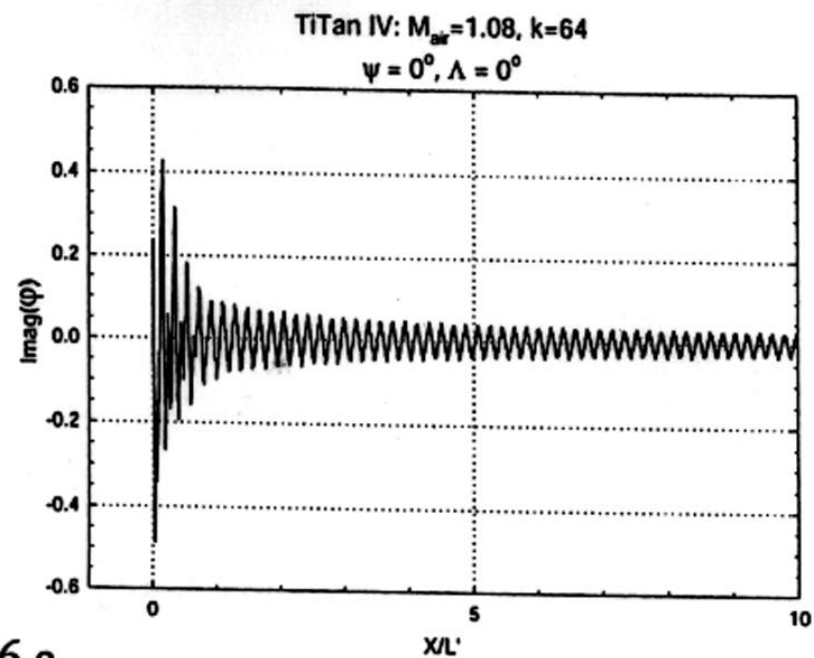
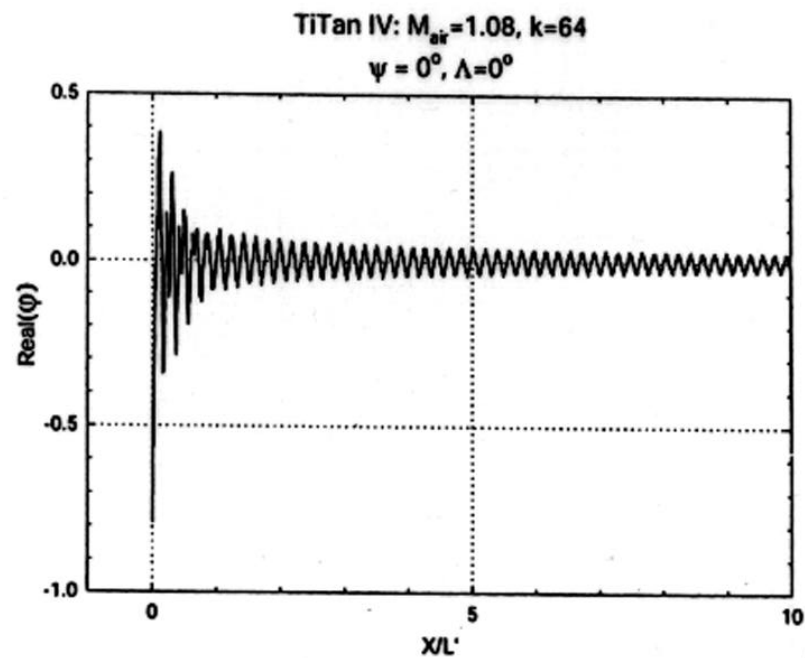


Fig. 36 a

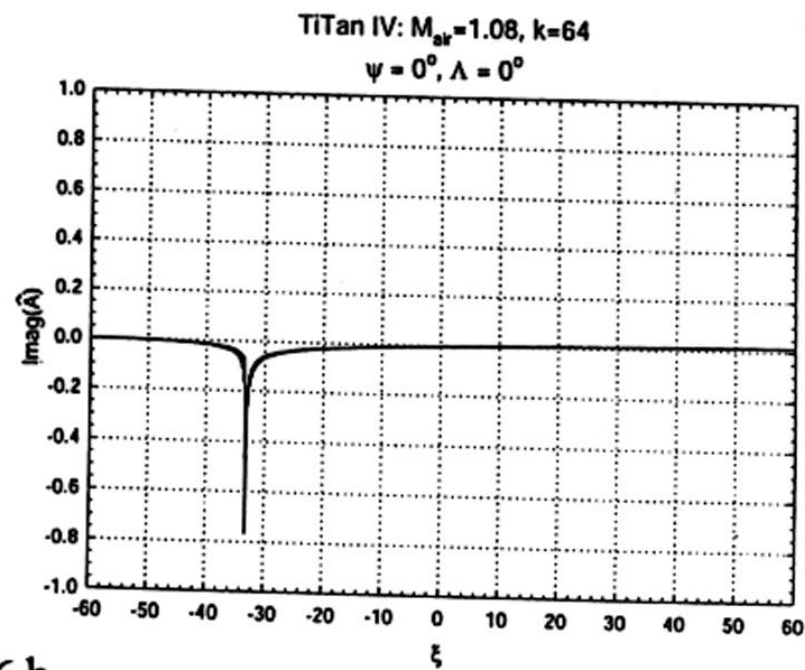
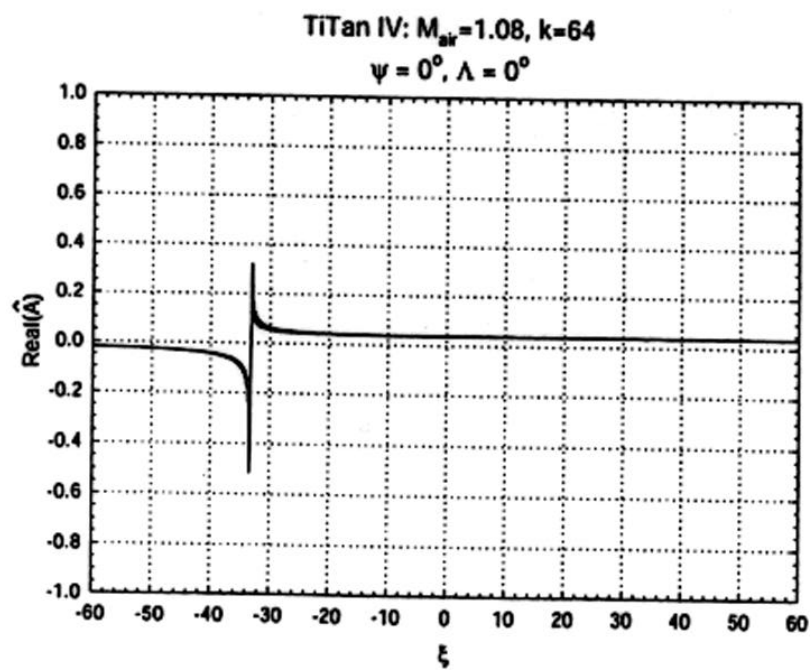


Fig. 36 b

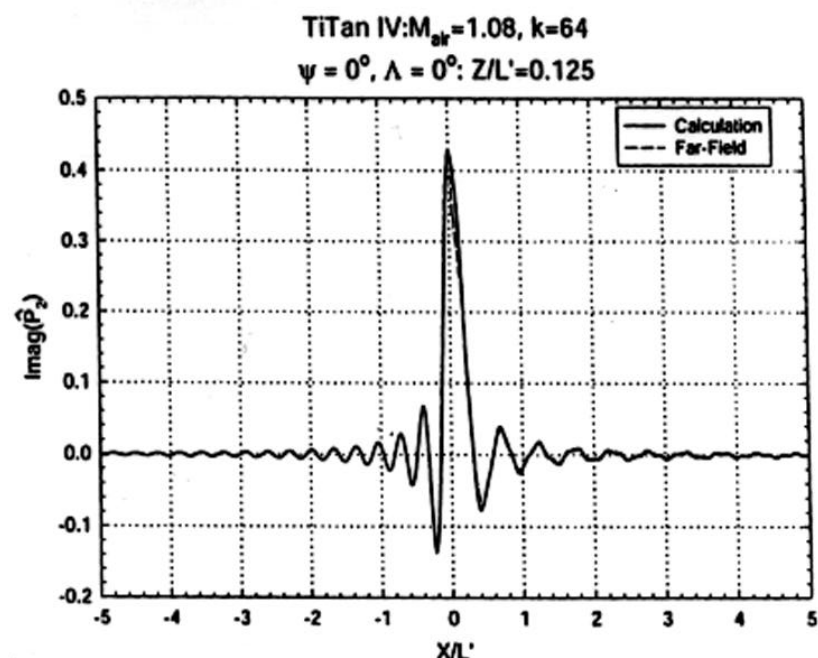
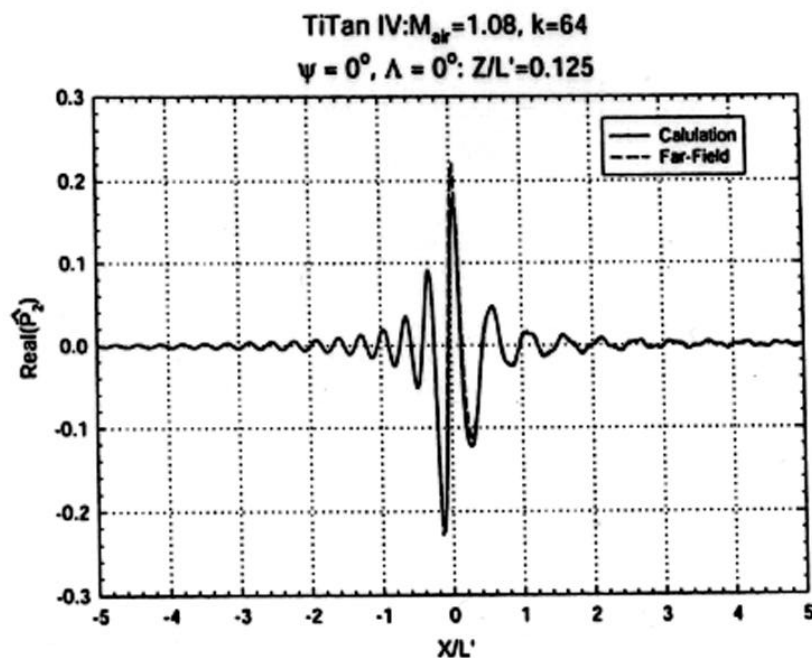


Fig. 37a

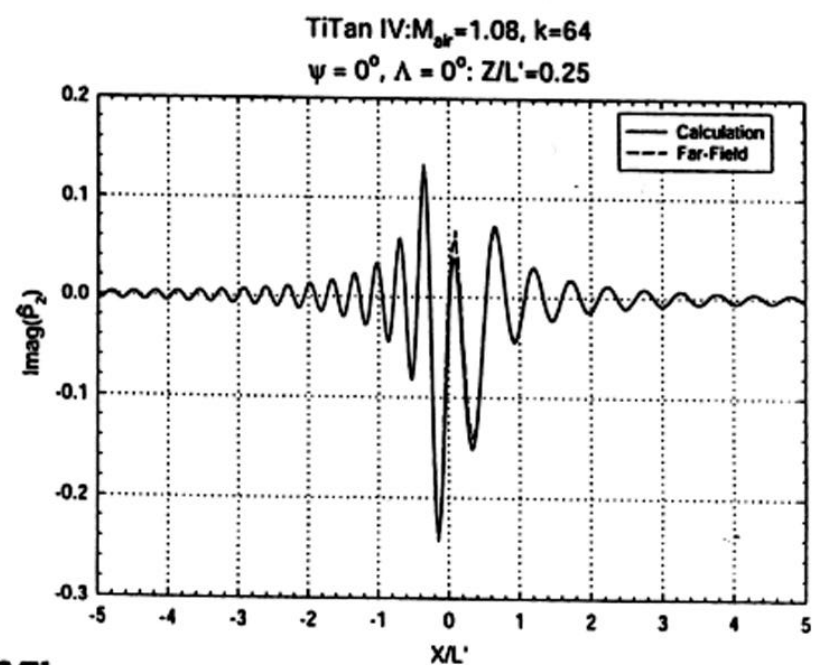
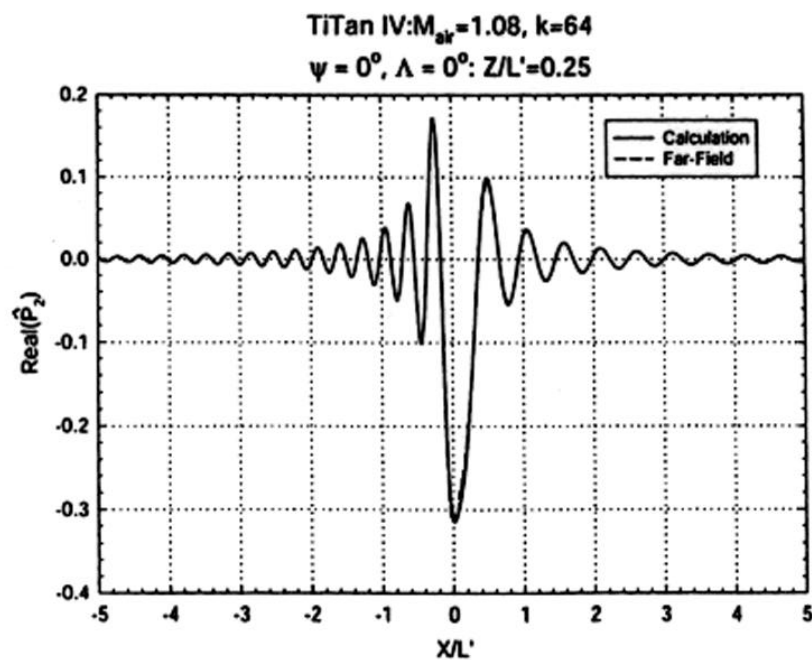


Fig. 37b

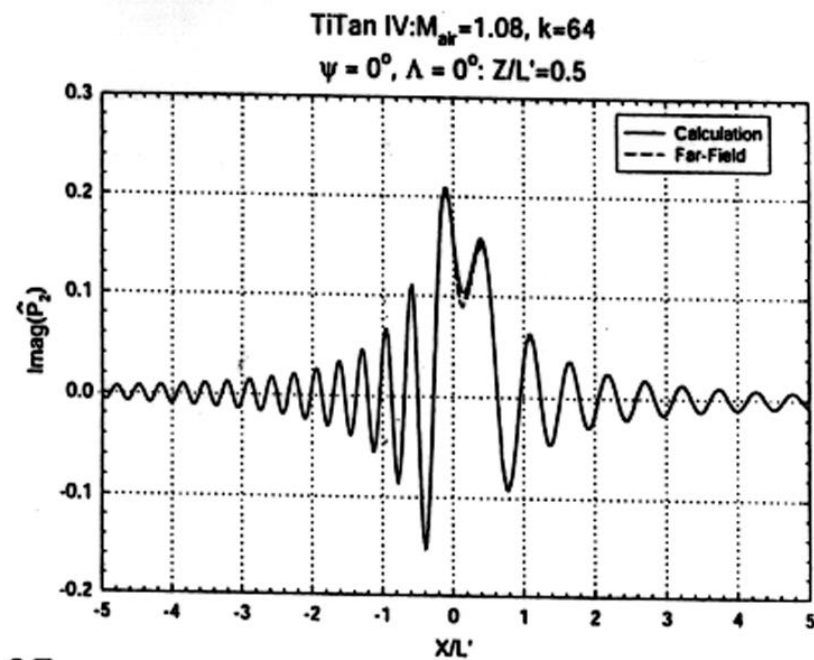
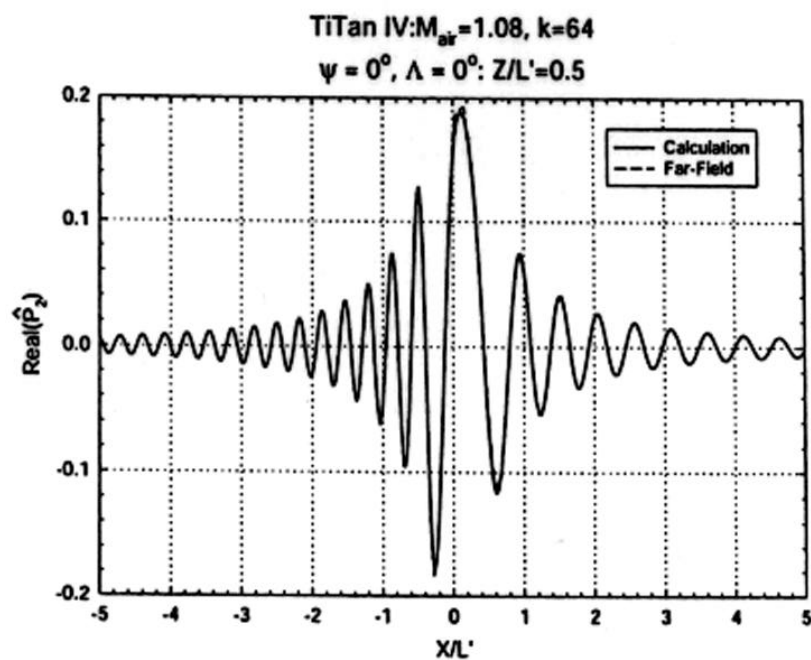


Fig. 37c

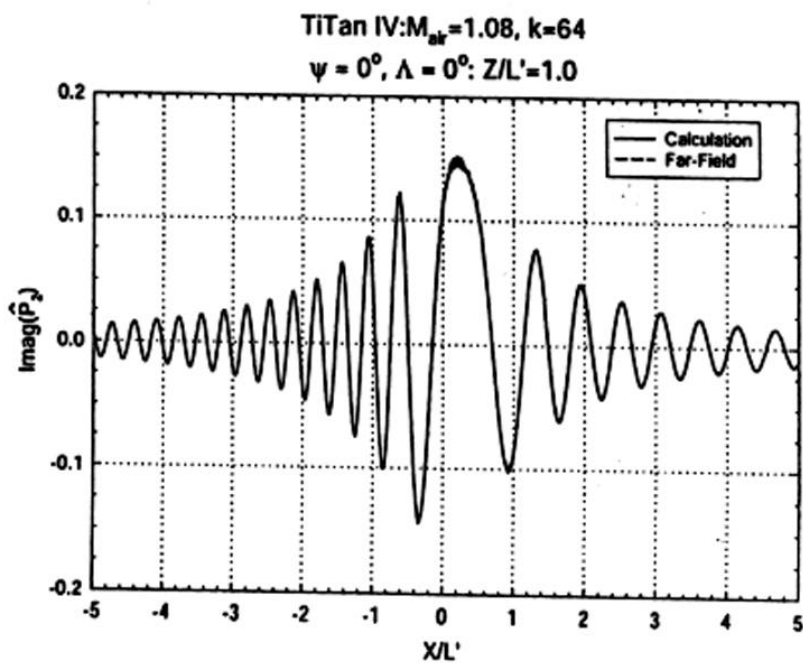
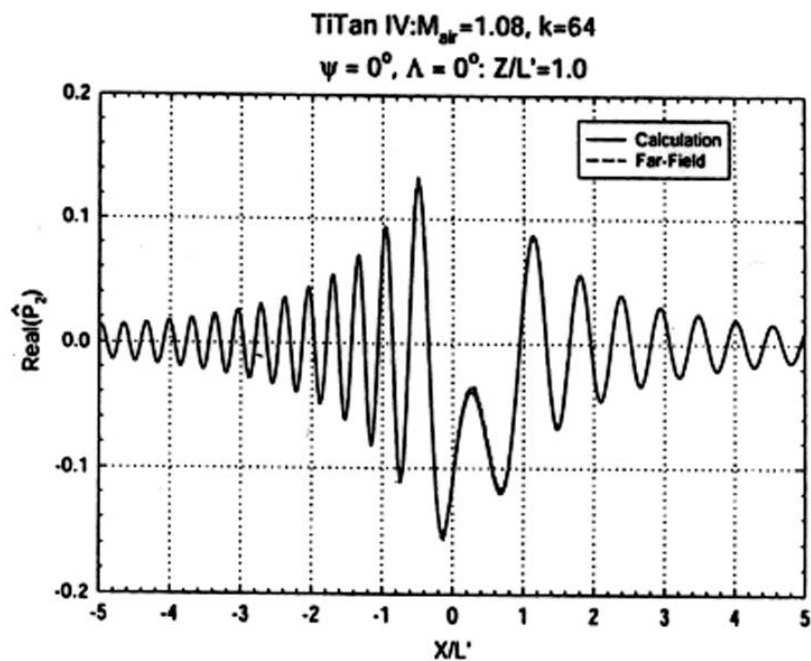
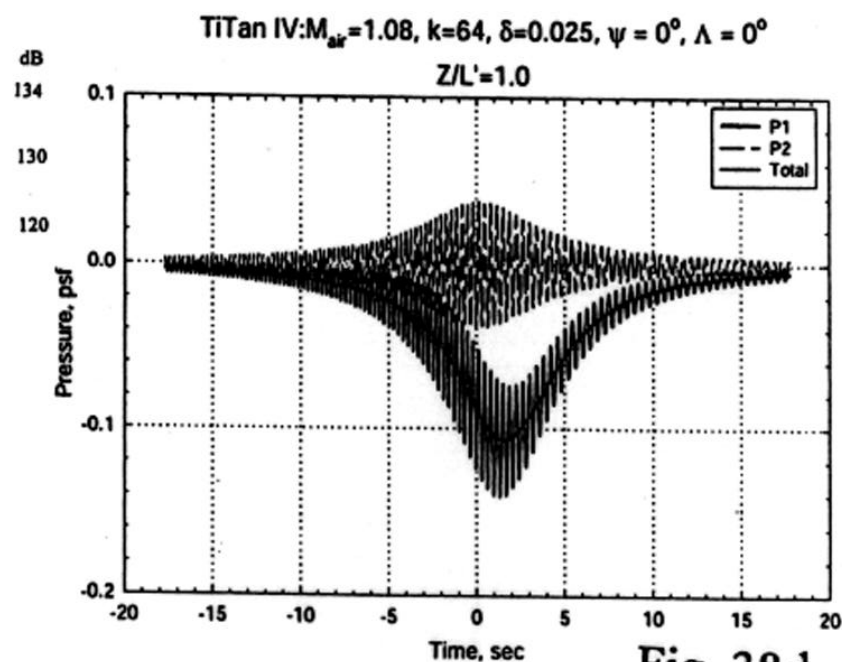
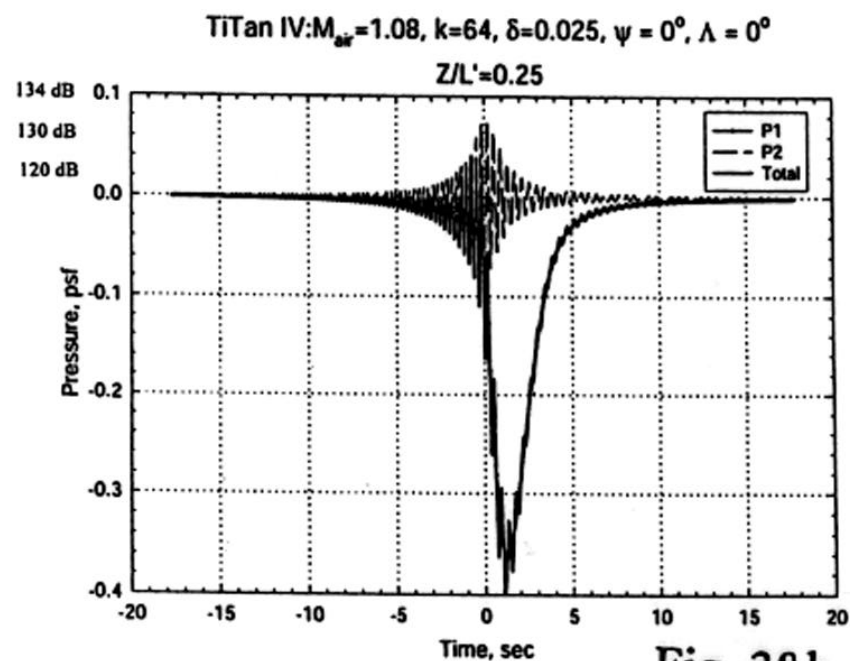
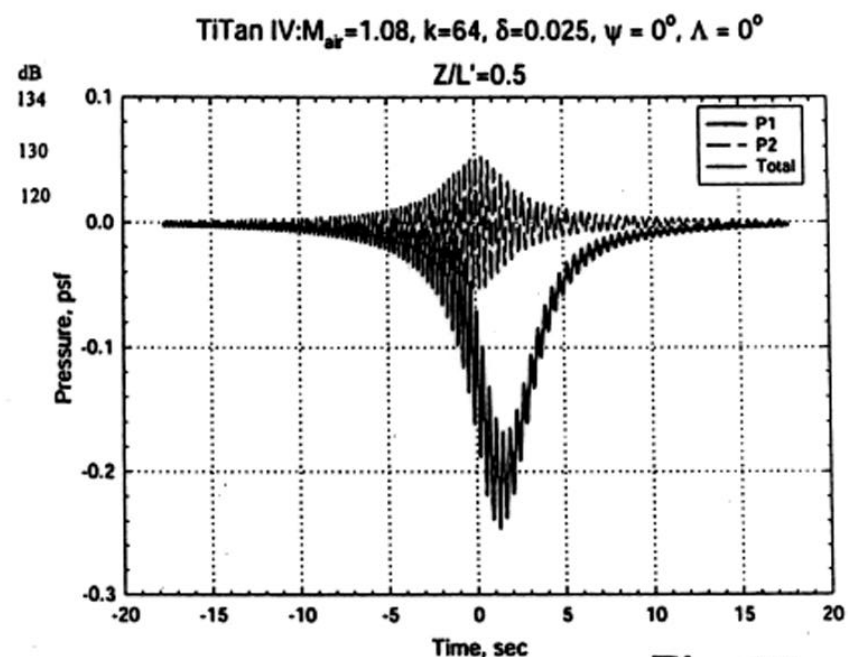
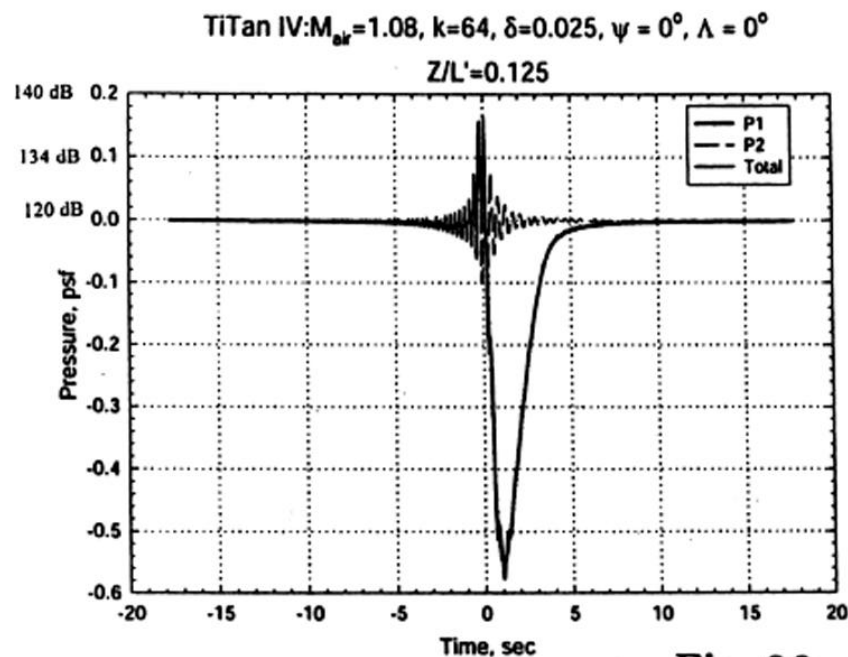


Fig. 37d



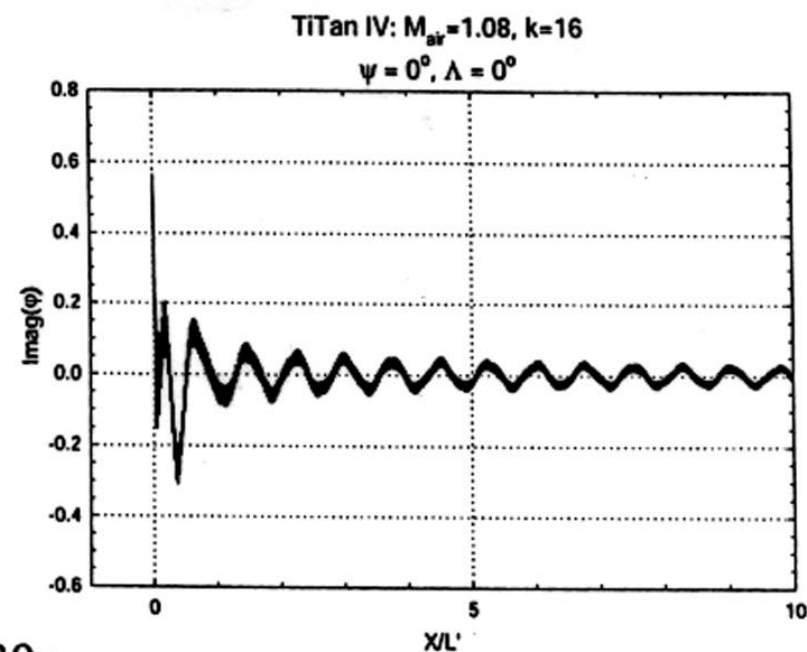
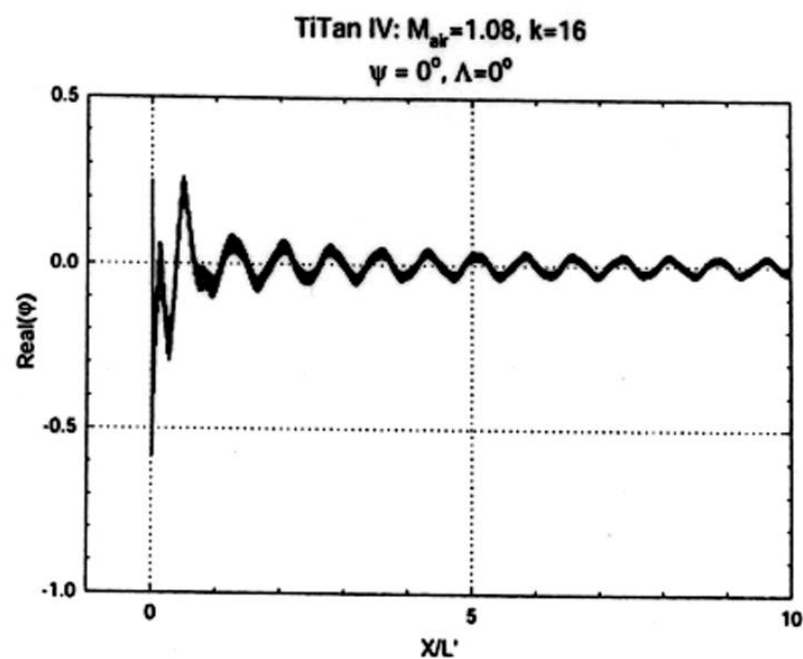


Fig. 39a

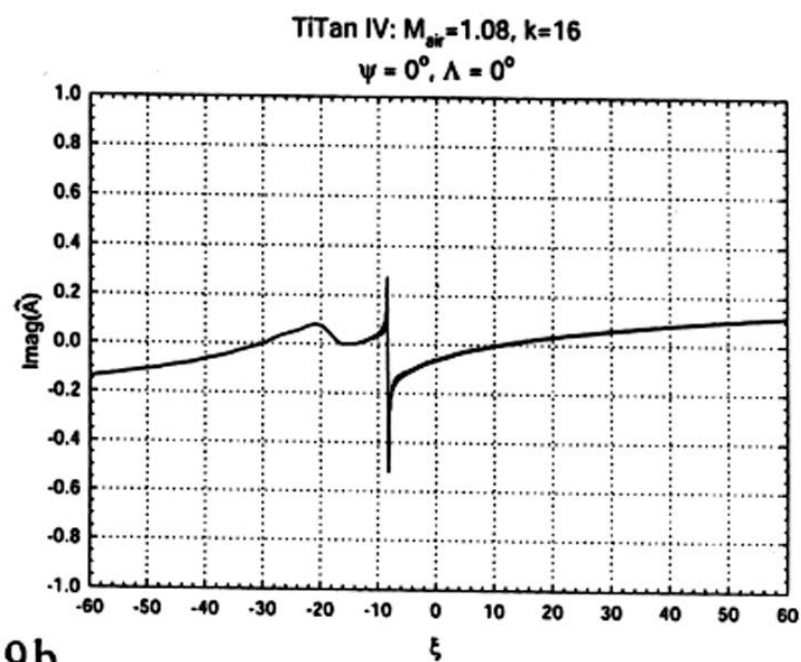
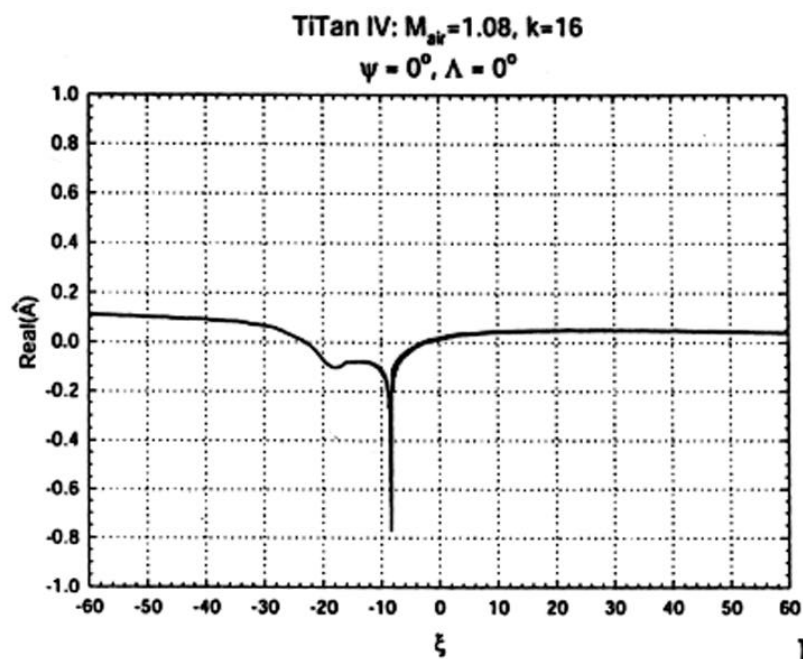


Fig. 39b



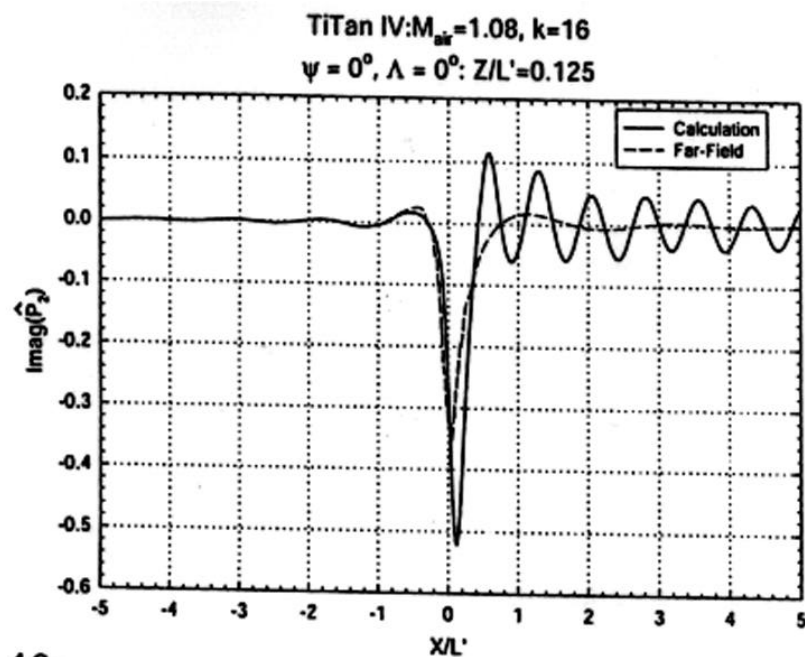
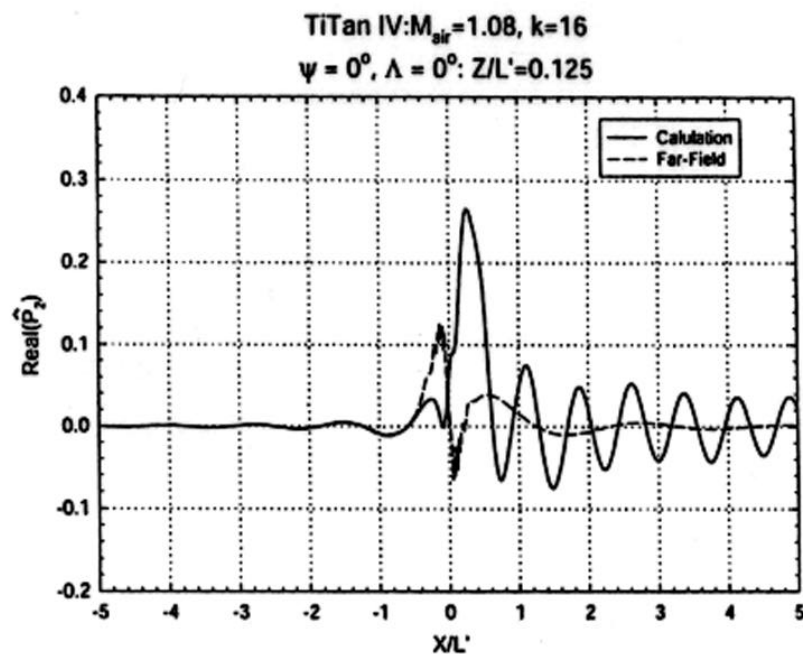


Fig. 40a

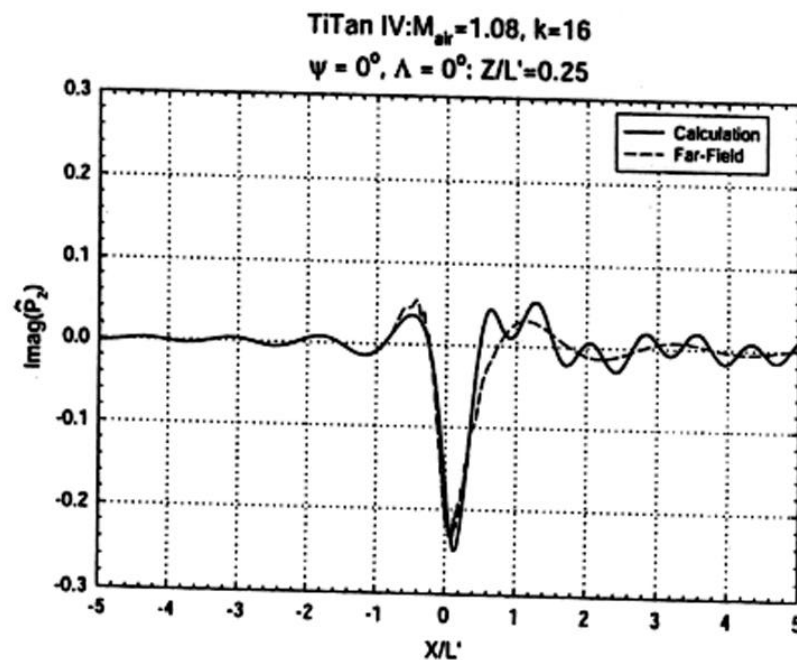
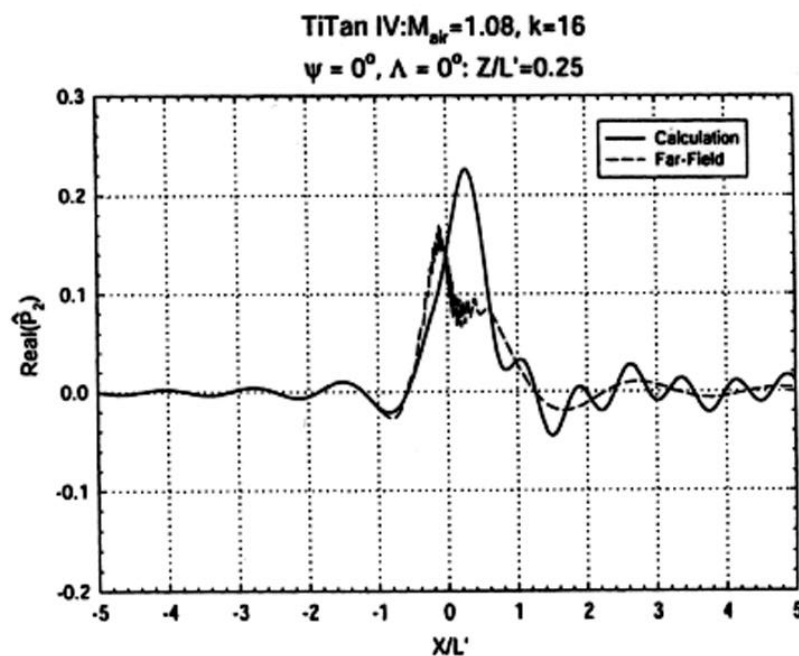


Fig. 40b

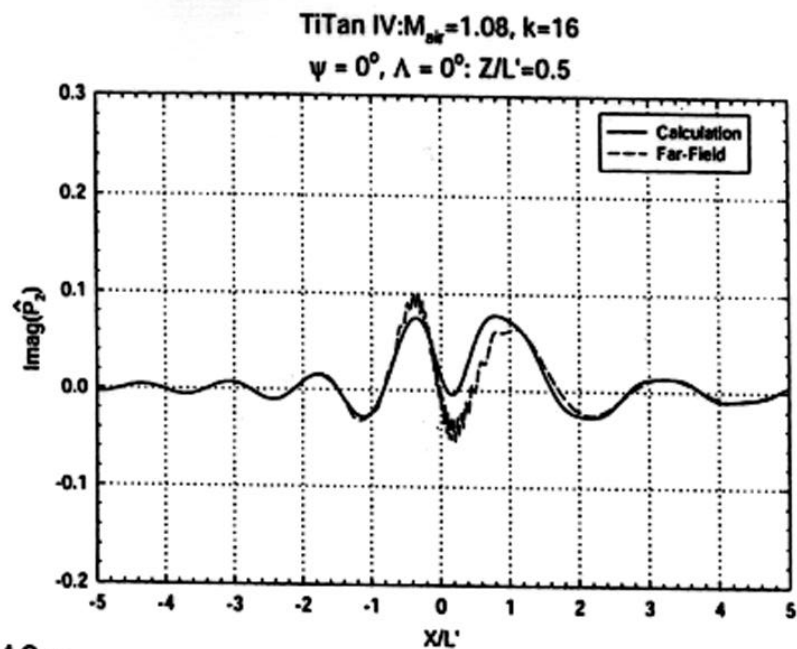
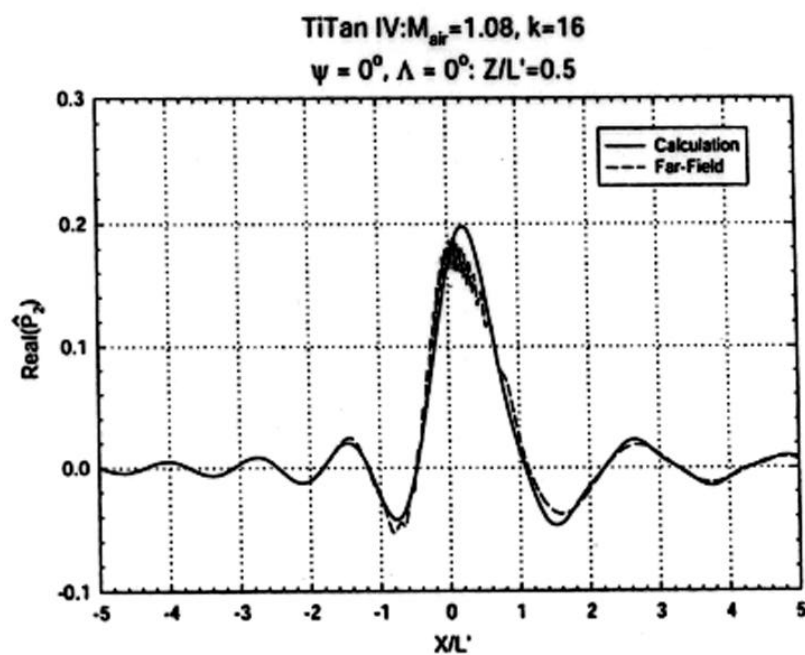


Fig. 40 c

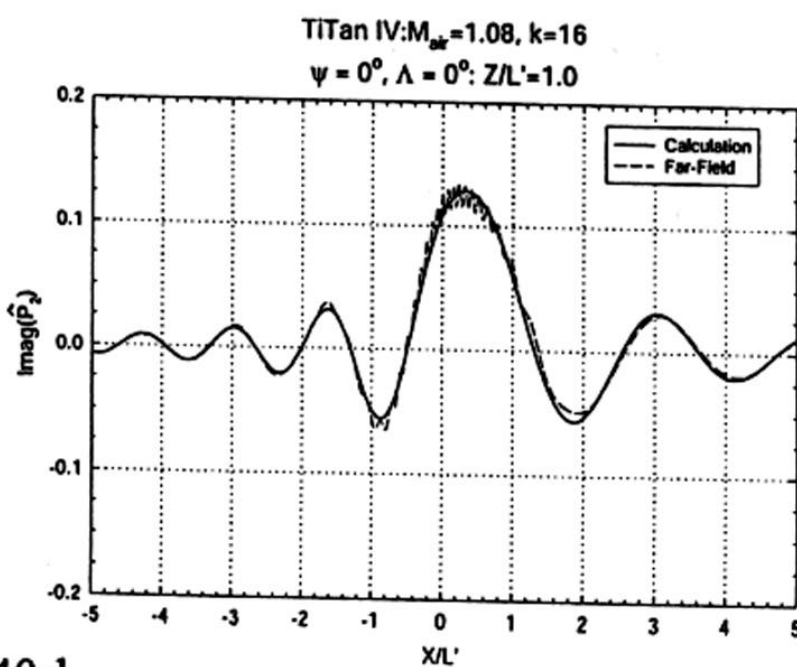
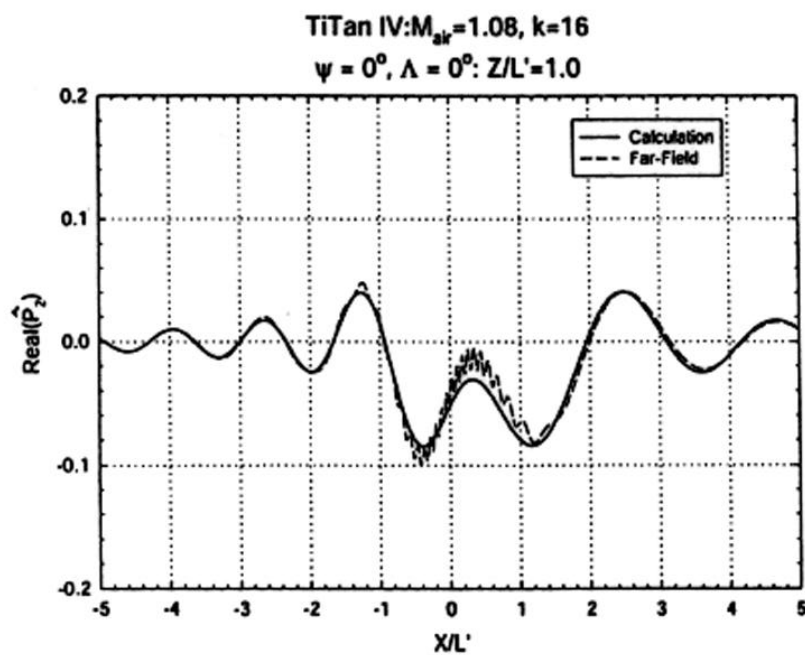


Fig. 40 d

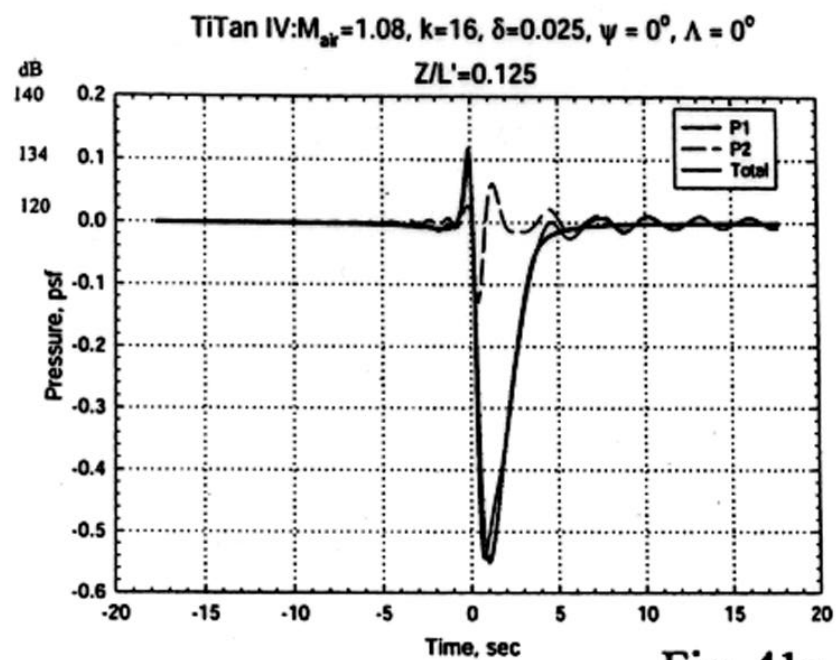


Fig. 41a

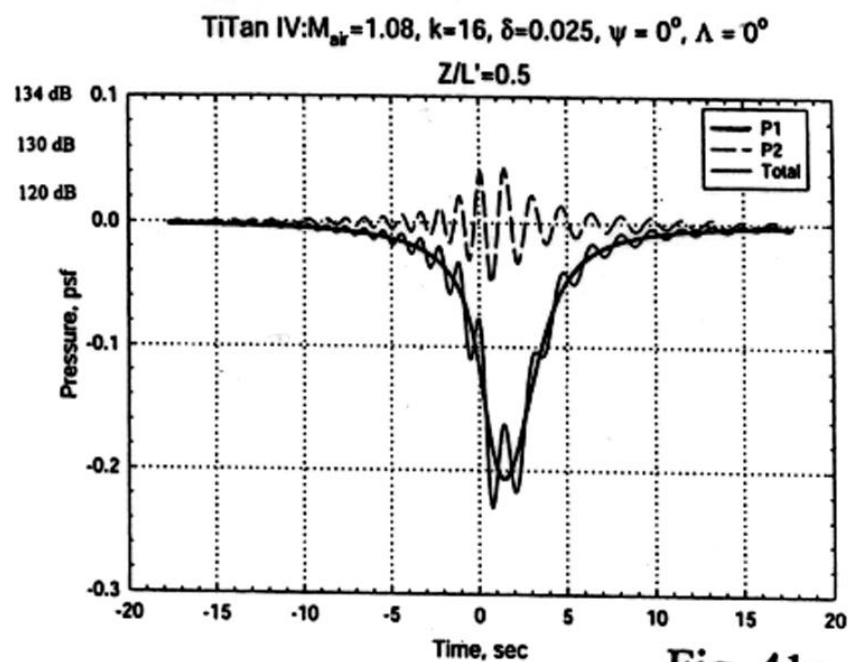


Fig. 41c

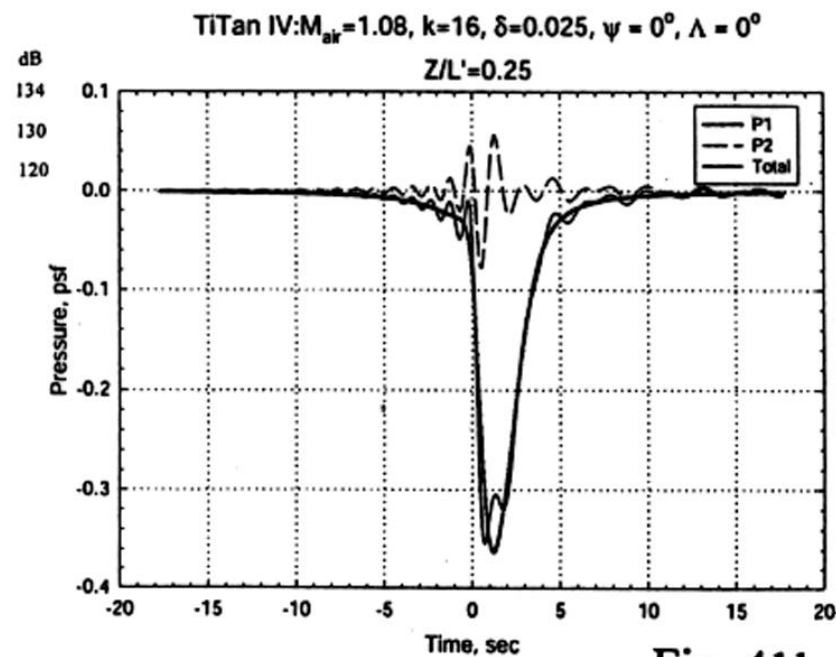


Fig. 41b

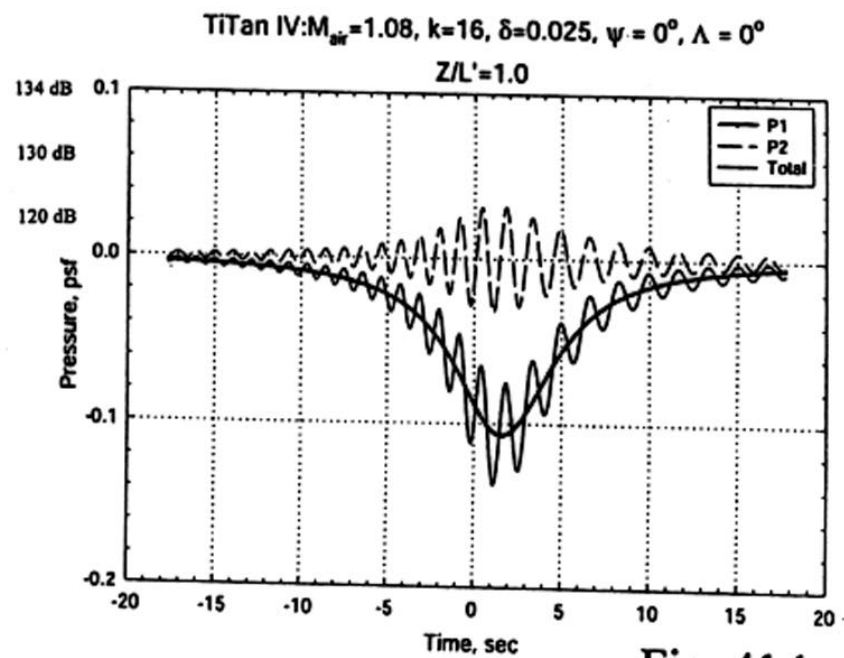


Fig. 41d

## Appendix I Surface Velocity Potential Representing Wavy Surface Response to Sonic Boom

### I.1 Surface velocity potential above water

The solution to  $\hat{\phi}_2(x; 0)$  for  $x' > 0$  is obtained in a convolution integral form involving Bessel function of the first kind, order zero

$$\hat{\phi}_2(x', 0) = -2 \frac{\delta \lambda}{B_n} \int_0^{x'} e^{ik'_1 x'_1} \left[ ik'_1 + B_n^2 \frac{d}{dx'_1} \right] f'(x'_1) \cdot e^{i(P/2B_n^2)(x_1 - x'_1)} \cdot J_0(\alpha |x' - x'_1|) dx'_1 \quad (I.1)$$

where the function  $f(\xi)$  is that in the velocity potential of the flat-ocean model

$$\phi'_1 = f(x' - B_n x') + f(x' + B_n x')$$

of which the second derivative  $f''(\xi)$  is to be treated in the Stieltjes sense, and the parameters  $\alpha$  and  $P$  are

$$\alpha \equiv k \sqrt{M_n^2 - \sin^2(\Lambda + \psi)} / B_n^2 \quad P \equiv 2k M_n^2 \cos(\Lambda + \psi). \quad (I.2a, b)$$

Note that the  $M_n^2$  in  $\alpha$  is  $M_n^2 = M_A^2 \cos \Lambda$  above the water; whereas the  $M_n^2$  in  $P$  as well as the parameter

$$Q \equiv k^2 [M_n^4 - (1 + M_n^2) \sin^2(\Lambda + \psi)] \quad (I.2c)$$

in other part of the development is  $M_A^2 \cos^2 \Lambda$  above water, and is  $M_w^2 \cos^2 \Lambda$  underwater.

With  $\hat{\phi}_2(x', 0)$ , the surface overpressure of the synchronous wavefield is determined as the real part of

$$p'_2 = -\epsilon \rho U_n e^{ik'_2 y'} e^{-i\Omega t} \left( \frac{d}{dx'} - ik' \right) \hat{\phi}_2(x', 0) \quad (I.3)$$

In the solution system developed in Part I and adopted for numerical programs, normalized quantities are used. The following table give the variables and parameters (upper row) and the corresponding scales (lower row) used in the normalization:

$x', y', z'$	$t'$	$\phi'$	$p'$	$\phi'_2$	$\lambda$	$k$	$\Omega$
$L'$	$L'/U$	$\epsilon p_A U^2$	$\epsilon \delta U L'$	$\epsilon \delta p_A U^2$	$L'$	$(L')^{-1}$	$U/L'$

### I.2 Specilization to the incident N-wave

For an incident N-wave with  $\max |f'| = 1$

$$\begin{aligned} f'(\xi) &= (2\xi - 1) \cdot 1(\xi) \cdot 1(1 - \xi), \quad 0 < x < 1 \\ &= 0 \quad x < 0, \quad x > 1 \end{aligned} \quad (I.4)$$

$$+4B_n e^{ik_1' x'} \int_0^x G(x' - x'_1) dx'_1 - 2B_n e^{i\mu \alpha x'} J_0(\alpha x'), \quad (I.5a)$$

and for  $1 < x' < \infty$ , as

$$\begin{aligned} \varphi(x, 0) = & i \frac{2k_1'}{B_n} e^{ik_1' x'} \int_0^1 (2x'_1 - 1) G(x' - x'_1) dx'_1 \\ & + 4B_n e^{ik_1' x'} \int_0^1 G(x' - x'_1) dx'_1 - 2B_n e^{i\mu \alpha x'} J_0(\alpha |x'|) - 2B_n e^{ik_1' x'} e^{i\mu \alpha (x'-1)} J_0(\alpha |x' - 1|), \end{aligned} \quad (I.5b)$$

where

$$G(\xi) \equiv e^{-i(k_1' - \mu \alpha) \xi} J_0(\alpha \xi), \quad \mu \equiv \frac{P}{2B_n^2 \alpha}. \quad (I.5c, d)$$

There are two discontinuities in the surface velocity potential at  $x' = 0$  and  $x' = 1$  which result from the transfer of the boundary condition for the  $N$ -wave.

## Appendix II Underwater Solution Details

### II.1 Sawyer's Model as Primary Wave-field Solution

Let  $p_1(x', 0)$  be the overpressure determined by the sonic boom over the *flat* interface which is related to  $f(\xi)$  of (I.1) and include the additional increase due to wave reflection. The Sawyers model yields

$$\begin{aligned} p_1(x', \bar{z}) &= \text{imag.} \frac{1}{\pi} \int_{b_1}^{b_2} \frac{p_1(x', 0) dx_1}{x_1 - \xi} \\ &= \frac{\bar{z}}{\pi} \int_{b_1}^{b_2} \frac{p_1(x', 0) dx_1}{(x'_1 - x')^2 + \bar{z}^2} \end{aligned} \quad (\text{II.1})$$

In approaching the interface  $\bar{z} \rightarrow 0$ , it yields

$$\begin{aligned} p_1(x', \bar{z}) &\sim p_1(x', 0) + \frac{\bar{z}}{\pi} \left[ -\frac{p_1(b_2, 0)}{b_2 - x'} + \frac{p_1(b_2, 0)}{b_2 - x'} \right. \\ &\quad \left. + p.v. \int_{b_1}^{b_2} \frac{p'_1(x'_1, 0) dx'_1}{x'_1 - x'} \right] \end{aligned} \quad (\text{II.2})$$

where, the "prime" on  $p_1$  refers to the derivative in  $x'$ ; here, the prescribed overpressure is recover and, in addition, the critical underwater  $p_1$  behaviour next to the interface is established. The latter in the form of  $\bar{z}(\partial p / \partial \bar{z})$ , is needed for a consistent analysis of the (secondary) effect that is crucial to the deepwater wavefield analysis.

For the N wave of (I.4), the R.H.S of (II.2) has been given explicitly in analytic form in Part I; here is the result for a slightly extended form representing an *unbalanced* incident N-wave

$$\begin{aligned} p_1(x', \bar{z}) &= \frac{1 - ax'}{\pi} \left[ \tan^{-1}\left(\frac{x'}{\bar{z}}\right) - \tan^{-1}\left(\frac{x' - 1}{\bar{z}}\right) \right] \\ &\quad - \frac{a\bar{z}}{\pi} \ln \left| \frac{(x' - 1)^2 + \bar{z}^2}{(x')^2 + \bar{z}^2} \right| \end{aligned} \quad (\text{II.4})$$

Where  $b_1$  and  $b_2$  are set equal to 0 and 1, respectively. In approaching the limit  $\bar{z} \rightarrow 0$ , it reduces to

$$\begin{aligned} p_1(x', \bar{z}) &\sim (1 - ax') [\text{sgn}(x') - \text{sgn}(x' - 1)] \\ &\quad - \bar{z} n \left[ \frac{1 - ax'}{\pi} \left( \frac{1}{x'} - \frac{1}{x' - 1} \right) + \frac{a}{\pi} \ln \left| \frac{x' - 1}{x'} \right| \right] \end{aligned} \quad (\text{II.5})$$

for the unbalanced N wave (II.3)

### II.2 Response Under A Wavy Ocean

The solution underwater responding to sonic boom (3.7) over surface wave train of (3.2 b) is described by the inverse Fourier transorm of the product  $\hat{A}(\xi)\sigma(\xi, \bar{z})$  [cf. (3.14)], where  $\sigma(\xi, \bar{z})$  is  $e^{\frac{1}{2}\pi} p(i|\bar{K}|^{1/2}\bar{z})$  for

$$\xi_1 < \xi < \xi_2$$

and becomes evanescent and attenuates in an exponential manner for  $\xi$  outside of this range, and  $\hat{A}(\xi)$  is the Fourier transform of the second-order overpressure *underwater* at the *reference* surface  $z=0$ , which consist of two parts

$$p'_{2w}(x', 0) = p'_{2A}(x', 0; t) - \bar{z}_w \left( \frac{\partial p'_1}{\partial \bar{z}} \right)_{ow} \quad (\text{II.6})$$

### Appendix III Large- $x'$ Expansion Of Surface Velocity Potential $\varphi$

In order to assure adequate accuracy in the numerical evaluation of the surface velocity potential  $\varphi$  for large  $x'$ , an expansion for  $x' \gg 1$  based on the  $J_0$  behaviour for the large argument was made:

$$\varphi \sim C_{11}e^{i\alpha(\mu+1)}(x')^{-1/2} + C_{21}e^{i\alpha(\mu-1)}(x')^{-1/2} \quad (\text{III.1})$$

where,

$$C_{11} = i\frac{2k}{B}(2B_{21} - A_{11}) + 4BA_{11} - B\sqrt{\frac{2}{\pi}}\frac{e^{-i\pi/4}}{\alpha^{1/2}}(1 + e^{i\kappa_1})$$

$$C_{21} = i\frac{2k}{B}(2B_{21} - A_{21}) + 4BA_{21} - B\sqrt{\frac{2}{\pi}}\frac{e^{-i\pi/4}}{\alpha^{1/2}}\{1 + e^{i\kappa_2}\}$$

$$A_{11} = \frac{1}{2}\sqrt{\frac{2}{\pi}}e^{-i\pi/4}\frac{e^{i\kappa_1}}{i\alpha^{1/2}\kappa_1}$$

$$A_{21} = \frac{1}{2}\sqrt{\frac{2}{\pi}}e^{i\pi/4}\frac{e^{i\kappa_2}}{i\alpha^{1/2}\kappa_2}$$

$$B_{11} = \frac{1}{2}\sqrt{\frac{2}{\pi}}e^{-i\pi/4}\left(\frac{-1}{\alpha^{1/2}\kappa_1^2}\left[e^{i\kappa_1}(i\kappa_1 - 1) + 1\right]\right)$$

$$B_{21} = \frac{1}{2}\sqrt{\frac{2}{\pi}}e^{i\pi/4}\left(\frac{-1}{\alpha^{1/2}\kappa_2^2}\left[e^{i\kappa_2}(i\kappa_2 - 1) + 1\right]\right)$$

$$\kappa_1 = -\alpha(\mu + 1), \quad \kappa_2 = -\alpha(\mu - 1)$$

Related to this is the asymptotic expansions of  $\hat{A}(\xi)$  near the two singularities at

$$\xi = \kappa_1, \kappa_2$$

associated with the Fourier Transform of the Bessel function  $J_0(\alpha x)$ :

$$\hat{A}(\xi) \sim C_{11}\sqrt{\frac{\pi}{2}}\frac{1}{|xi - \kappa_1|^{1/2}}[1 + i \operatorname{sgn}(\xi + \kappa_1)], \quad |\xi - \kappa_1| \ll 1; \quad (\text{III.2a})$$

$$\sim C_{21}\sqrt{\frac{\pi}{2}}\frac{1}{|xi - \kappa_2|^{1/2}}[1 + i \operatorname{sgn}(\xi + \kappa_2)], \quad |\xi - \kappa_2| \ll 1; \quad (\text{III.2b})$$

These behaviours also effect the accuracy in numerical evaluation of  $\hat{A}(\xi)$ . Both (III.1) and (III.2) were utilized in implementing the numerical calculation of  $\varphi$  and  $\hat{A}$  in earlier code development to help ascertain the accuracy level affected by the integration step size in  $x'_1$  and in  $\xi$ .

For this purpose, it suffices to set  $\Lambda = \psi = 0$  with which  $\mu = M_A$  simply.



## Appendix IV Extension to General, Periodic Surface Wave Trains; Synchronous Solution for High $k$ Re-Examined

For the purpose of establishing the validity and properties of the underwater wavefield solution for a periodic surface-wave train under  $kz \gg 1$ , a knowledge of the solution behaviour for high  $k$  will be utilized. This behaviour will be more carefully examined in Section IV.1; The result furnishes also a rational basis for explaining the behaviour found at small  $\bar{z}$  in the numerical solutions obtained for high  $k$ .

Convergence of the Fourier series for the periodic surface-wave train will be investigated in Section IV.2. The inverse square-root attenuation behaviour will be established in Section IV.3 for the *spatial* average of  $p'$  under  $k\bar{z} \gg 1$ . Solution behaviour for surface wave-train generated from continuous  $k$ -spectra are examined in Section IV.4 with an analytical model.

### IV.1 Synchronous solution of $p_2$ at high $k$ and low $k$ .

We shall examine the  $p_2$  behaviour for an incident N-wave for which explicit expression can be analytically studied; the examination is further simplified by restricting to the non-aligned case directly under the flight track,  $\Lambda = \psi = 0$ . The limitation to the N wave should not be considered too restrictive, because our results do not indicate a critical dependence on the parameters characterizing the incident N-waves and its shock-like discontinuities.

#### (1) $\hat{A}$ Behaviour at $k \gg 1$

The function  $\hat{A}(\xi)$  in the integral solution for  $p_2$ , (3.14) is composed of two main parts according to Part I, (6.1)

$$\hat{A}(\xi; k) = -i \frac{2\pi}{k} (\xi + k) FT\varphi(x', 0) + FT\Delta(P_{BT}) \quad (IV.1)$$

where the function  $\hat{A}$  has been written above as  $\hat{A}(\xi; k)$  to amplify its dependence on the parameter  $k$ . It can be simplified to a form in terms of a rescaled Fourier variable

$$\bar{\xi} \equiv \xi/k \quad (IV.2)$$

and large  $k$ , subject to error of  $O(k^{-2})$ ,

$$\hat{A}(\xi; k) = \hat{A}(\bar{\xi}; k) = D_{\infty}(\bar{\xi}) \frac{1 + e^{ik(1+\bar{\xi})}}{k} \quad (IV.3a)$$

where

$$D_{\infty}(\bar{\xi}) = 2\sqrt{2\pi} \left[ \frac{1 - B_n^2(1 + \bar{\xi})}{B_n \sqrt{R_1 R_2}} + i\beta_n \operatorname{sgn}(1 + \bar{\xi}) \right] \quad (IV.3b)$$

with

$$\bar{R}_1 \equiv R_1/k = \bar{\xi} - \xi_{A1}, \quad \bar{R}_2 \equiv R_2/k = \bar{\xi} - \xi_{A2} \quad (IV.3c, d)$$

$$\xi_{A1} = -\frac{M_{nA}}{B_n^2} (M_{nA} + 1), \quad \xi_{A2} = -\frac{M_{nA}}{B_n^2} (M_{nA} - 1) \quad (IV.3e, f)$$



therefore the (integrable) singularities at  $\bar{R}_{12} = \bar{\xi} + 1 = 0$ , occurs only in the  $\xi$ -ranges corresponding to the evanescent domain, outside of the interval  $[\bar{\xi}_1, \bar{\xi}_2]$  of relevance. The  $k$  dependencies of  $|\hat{p}_2|$  at high  $k$  in the form of  $k^{-1}$  is note worthy. In passing, a similar  $k^{-1}$  dependence is also found for  $k \ll 1$ , subject to errors of the unit order,

$$\hat{A}(\bar{\xi}, k) \sim \frac{D_o(\bar{\xi})}{k} \quad (\text{IV.5a})$$

where

$$D_o(\bar{\xi}) = i8\sqrt{2\pi}/B_n \sqrt{\bar{R}_1 \bar{R}_2} \quad (\text{IV.5b})$$

Therefore,

$$k\hat{A} = O(1) \neq 0 \quad (\text{IV.6})$$

(ii) *The  $\hat{p}_2$  for a high  $k$*

Interference of neighbouring wave component affects strongly the underwater  $\hat{p}_2$  behaviour for a high  $k$  as for a large  $\bar{z}$ . In fact, the parameter controlling this interference effects turns out to be simply the product  $k\bar{z}$ . The expression of  $\hat{p}_2$  as the inverse transform of  $\hat{A}\sigma$ , after re-normalized with  $\bar{\xi} \equiv \xi/k$  replacing  $\xi$  in (3.14) and applying (IV.3), reads

$$\begin{aligned} \hat{p}_2 &= \frac{1}{\sqrt{2\pi}} \int_{\bar{\xi}_1}^{\bar{\xi}_2} D_\infty(\bar{\xi}) [1 + e^{ik(1+\bar{\xi})}] \exp[ik\bar{\xi}(|\bar{K}|^{\frac{1}{2}} - \bar{\xi}\eta)] d\bar{\xi} \\ &= \frac{e^{ik}}{\sqrt{2\pi}} \int_{\bar{\xi}_1}^{\bar{\xi}_2} D_\infty(\bar{\xi}) e^{i[|\bar{K}|^{1/2} - \bar{\xi}(\eta - \frac{1}{2})]k\bar{z}} d\bar{\xi} + \frac{1}{\sqrt{2\pi}} \int_{\bar{\xi}_1}^{\bar{\xi}_2} D_\infty(\bar{\xi}) e^{i[|\bar{K}|^{1/2} - \bar{\xi}\eta]k\bar{z}} d\bar{\xi} \end{aligned} \quad (\text{IV.7})$$

Except for the omission of the factor  $(1 + e^{ik(1+\bar{\xi})})$  in the limiting form of  $k\hat{A}$  in (IV.3), the second integral may be regarded the same as that analyzed earlier for large  $\bar{z}$ ; the argument  $(|\bar{K}|^{\frac{1}{2}} - \bar{\xi}\eta)k\bar{z}$  is identifiable with  $g(\xi)z$  in Part I, (5.23a); whereas, the argument under the exponent in the first integral differs from  $g(\xi)z$  by only the addition of the term  $(\bar{\xi}/\bar{z})k\bar{z}$  or  $\xi$ . The  $\xi$ -value at the stationary phase for the second integral is thus the same as that in the analysis for a high  $\bar{z}$ , fixed  $k$ , namely  $\xi_*(\eta)$  in (3.16d); the stationary  $\xi$ -value for the first integral differs from  $\xi_*$  but is seen readily to be one with a displaced  $\eta$ :

$$\xi_{**} = \xi_* \left[ \eta - \frac{1}{\bar{z}} \right] = \xi_* \left[ \frac{z-1}{\bar{z}} \right], \quad (\text{IV.8a})$$

The result for  $k\bar{z} \gg 1$  thus gives

$$\hat{p}_2 \sim \frac{e^{-i\frac{\pi}{4}}}{\sqrt{k\bar{z}}} \frac{D_\infty(\bar{\xi}_*)}{\sqrt{|h''_*|}} e^{i[h_*(\eta - \frac{1}{\bar{z}})k\bar{z}]} + \frac{D_\infty(\bar{\xi}_{**})}{\sqrt{|h''_{**}|}} e^{ik(1+\bar{\xi}_{**})} e^{i[h_{**}(\eta - \frac{1}{\bar{z}})k\bar{z}]} \quad (\text{IV.8b})$$

where  $h(\bar{\xi}) = |\bar{K}|^{1/2}$  and the subscripts \* and \*\* refer to  $\xi_*$  and  $\xi_{**}$  respectively. Accordingly the result for a large  $k\bar{z}$  differs noticeably from the deep water result only in the range of small  $\eta$  or simply  $z' = O(1)$ . This furnishes the basis for explaining the agreement of the far-field (large  $z$ ) result with the numerically exact calculation at a rather small depth ( $\bar{z} \ll 1$ ) under a large  $k$ .

#### IV.2 Fourier-series representation of a periodic surface-wave train.

Consider a *non-monochromatic*, periodic form (3.18)

$$Z_w = F(\chi) = F(\chi + 2\pi) \quad (\text{IV.9})$$

where  $\chi$  is the argument  $k_1x + k_2y - \Omega t = k'_1x'_2 + k'_2y'_2 - \Omega t$  of (3.2). Here, the wave-length  $\lambda = 2\pi/k$  with  $k \equiv \sqrt{k_1^2 + k_2^2} = \sqrt{k'^2_1 + k'^2_2}$  corresponds to the period  $2\pi$  in  $\chi$  and will be the fundamental wave-length in a fourier expansion of  $F(\chi)$ :

$$F(\chi) = C_0 + \sum_{n=1}^{\infty} [C_n e^{i\chi n} + C_{-n} e^{-i\chi n}] \quad (\text{IV.10a})$$

For the continuous surface  $Z_w$  considered, the coefficient  $C_n$  diminishes with increasing  $n$  no slower than

$$C_n = O\left(\frac{1}{n^2}\right) \quad (\text{IV.10b})$$

which allows also finite numbers of slope discontinuities within each period (Pipe 1946, Churchill 1941) and assures the series' absolute convergence.

The time-dependent underwater wavefield can be constructed from the sum of synchronous solutions for the (individual) monochromatic surface-wave train  $C_n e^{i\chi n}$

$$p' = \sum_{-N}^N C_n p_n \quad (\text{IV.11a})$$

with

$$p_n = \hat{p}_2(x'; \bar{z}; kn) e^{-iknt} \quad (\text{IV.11b})$$

where  $kn$  replace  $k$  in the synchronous solution for the  $n$ th mode. In (IV.11) and below, we limit the consideration to that of  $\Lambda = \Psi = 0$ . The serious solution (IV.11) generated from  $\hat{p}_2$  for the sinusoidal surface component is expected to satisfy the prescribed value on the interface  $\bar{z}$ . The answer to the questions on the validity of  $p'$  and its dependence on  $k$  and  $\bar{z}$  must rests on the convergence of the series (IV.11). This will depend on behaviour of the individual synchronous solution corresponding to a large wave number  $nk$ .

### IV.3 Convergence of series solution

#### (i) Series Convergence On The Interface

We shall examine the convergence of the series solution (IV.11) on the interface  $z = Z_w$  or its analytical equivalence at  $\bar{z}$ . The  $\hat{p}_2(x', 0; k)$  for the synchronous solution furnishes by the time dependent wave-field *abovewater* is given by (3.6b) once the surface velocity potential  $\hat{\phi}_2(x', 0; h)$  is obtained. The latter is determined from a convolution integral in Part I, (5.8a). After rescaling the variables in a manner consistent with (3.3 a,b), it can be shown that  $\hat{\phi}_2(x', 0; k)$  vanishes with increasing  $k$  as  $1/k$ . Eq. (3.6 b) then indicates that, for  $|k| \gg 1$

$$|\hat{p}_2(x; 0; k)| = |\hat{p}_2(kx; 0; k)| = O(1) \neq 0 \quad (\text{IV.12})$$

being independent of  $k$ . Therefore the  $p_n$  in (IV.11b) is bounded and the series (IV.11a) converges absolutely, as does the series (IV.10a).

(ii) *Solution Convergence Underwater at  $|k|\bar{z} \ll 1$  and  $k\bar{z} = O(1)$*

We next examine the convergence of the  $p'$  series underwater for  $k\bar{z} = O(1)$  including  $|k|\bar{z} \ll 1$ . The latter is more general than  $\bar{z} \gg 1$ . The solution of interest is given as an inverse Fourier transform of the product of  $\hat{A}(\xi; k)$  and  $\sigma(\xi, \bar{z}; k)$  with (3.13a). The function  $\hat{A}(\xi; k)$  is the Fourier transform of  $\hat{p}_2(x', 0; k)$  and may be inferred to vanish with an increasing  $k$  as

$$\hat{A}(\xi; k) \equiv \hat{A}(\bar{\xi}; k) = O\left(\frac{1}{k}\right) \quad (\text{IV.13})$$

This is borne out by the result from the exact solution for the incident N-waves, (IV.3). On the other hand, the exponential argument  $|\bar{K}|^{1/2}$  defining  $\sigma$  in (3.13b) can be expressed as

$$|\bar{K}|^{1/2}\bar{z} = k\bar{z}\sqrt{-\bar{\xi}^2 + (\bar{P}\bar{\xi} + \bar{Q})/\beta_n^2} = h(\bar{\xi})k\bar{z} \quad (\text{IV.14})$$

[cf.(3.11b) for definition of  $\bar{k}$ ] Thus  $\sigma$  approaches unity for  $k\bar{z} \ll 1$  and is of unit order in  $k\bar{z} = O(1)$ ; therefore

$$\hat{A}\sigma = O\left(\frac{1}{k}\right) \quad (\text{IV.15})$$

for large  $k$ , as  $k\bar{z}$  is finite. Rescaling the variable of the inverse Fourier transform (3.14) confirms that in the domain  $k\bar{z} = O(1)$ , including  $k\bar{z} \ll 1$ ,

$$\hat{p}_2(x, \bar{z}; k) = O(1) \quad (\text{IV.16})$$

which may indeed match the order of  $\hat{p}_2(x, 0; k)$ . Therefore  $p_n$  in (IV.11) will be bounded for all  $n$ , and by virtue of the coefficient's dependence on  $n$ , (IV.10 b), the  $p'$  series will converge (absolutely) in the domain  $k\bar{z} = O(1)$ . In passing, we recall that singularities in  $\hat{A}(\bar{\xi}; k)$  exist but are integrable and can not affect the foregoing conclusion. It may also be noted that the series (IV.11) for  $p'$  underwater is expected to converge much faster than the series (IV.10) for the surface shape, owing to the additional factor  $1/\sqrt{n}$  contributed by the  $k$  dependence of the  $\hat{p}_2$  shown in (IV.8b).

(iii) *More Explicit Results:  $k\bar{z} \gg 1$*

For  $k\bar{z} \gg 1$ , the result of  $\hat{p}_2$  obtained for large  $k$  may be used to furnish an explicit expressions for all  $p'_n$ s in the series (IV.11). A conclusion as to how  $|p'|$  may depend on  $k$  and  $\bar{z}$  cannot be drawn immediately, since an exponential dependence on  $k\bar{z}$  also appears in each term of this series. The structure of the  $\hat{p}_2$  obtained for large  $k\bar{z}$  in (IV.8b) suggests that  $p'$  series (IV.11) may be summed in parts as

$$p' = \frac{e^{i\frac{\pi}{4}}}{\sqrt{k\bar{z}}} \left[ \frac{D_{\infty}(\xi_*)}{\sqrt{|h'|_*}} \sum_{-\infty}^{\infty} \frac{C_n}{\sqrt{n}} e^{i\Theta_1 kn} + \frac{D_{\infty}(\xi_{**})}{\sqrt{|h'|_{**}}} \sum_{-\infty}^{\infty} \frac{C_m}{\sqrt{m}} e^{i\Theta_2 km} \right] \quad (\text{IV.17})$$

with

$$\Theta_1 = (h_* - \eta\xi_*)\bar{z} - t, \quad \Theta_2 = (h_{**} - \eta\xi_{**})\bar{z} + 1 + \xi_{**} - t \quad (\text{IV.18})$$

The mean square of  $p'$  with respect to time over the fundamental period  $2\pi/k$  is, using overbars to represent complex conjugates,

$$|p'_{MS}|^2 \equiv \frac{k}{2\pi} \int_t^{t+2\pi/k} (p' \bar{p}') dt = \frac{1}{|k\bar{z}|} \left( \frac{|D_\infty|^2}{|h''|_*} + \frac{|D_\infty|^2}{|h''|_{**}} \right) \sum_{-\infty}^{\infty} \frac{|C_n|^2}{n} + \frac{\Pi(\eta, k)}{|k\bar{z}|} \quad (\text{IV.19a})$$

$$\Pi(\eta, k) \equiv \frac{|D_\infty(\xi_*)| |\bar{D}_\infty(\xi_{**})|}{|h''_* h''_{**}|^{1/2}} \sum_{n,m} \frac{C_n \bar{C}_m}{|nm|^{1/2}} \left[ \frac{k}{2\pi} \int_0^{2\pi/k} e^{i(\Theta_1 n - \Theta_2 m)kt} dt \right] + \text{c.c} \quad (\text{IV.19b})$$

where c.c stands for the complex conjugate

Note that without the last term, the mean square of  $p'$  would be inversely proportional to  $|k\bar{z}|$ . To see how  $\Pi$  depends on  $k$ , consider  $|x'| \gg 1$ , for which  $\xi_{**} \sim \xi_*$ ; and

$$k[\Theta_1 n - \Theta_2 m] = (h_* - \eta \bar{\xi}_*) h \bar{z} (n - m) - (1 + \bar{\xi}_*) k - (n - m) t k.$$

The term inside the square brackets of  $\Pi$  now becomes  $\exp(-i(1 + \bar{\xi}_*)kn)$  therefore, for  $x' = 0$ ,

$$\Pi(\eta, k) = 2 \frac{|D_\infty(\xi_*)|^2}{|h''_*|} \sum_{-\infty}^{\infty} \frac{|C_n|^2}{|n|} \cos[(1 + \bar{\xi}_*)kn] \quad (\text{IV.20})$$

Owing to the dependence of  $\Pi(\eta, k)$  on  $k$  shown, the RMS of  $p'$  for a periodic surface-wave train can not readily follow the inverse square root rule  $p' \propto (k\bar{z})^{-1/2}$  without additional consideration. In fact this  $k$  dependence couldnot be neglected with the help of the 'destructive interference' effect of the neighbouring  $\bar{\xi}_*(\eta)$  on the  $\Pi((\bar{\xi}_*, k))$ . This can be seen from the (spatial) averaged value of  $\Pi$  taken over entire  $x'$ -range (excluding  $x'=O(1)$ ) at a fixed depth  $\bar{z}$ , corresponding to  $-\infty < \eta < \infty$ , or  $\bar{\xi}_1 < \bar{\xi} < \bar{\xi}_2$

$$\begin{aligned} \langle \Pi \rangle &\equiv \frac{1}{\bar{\xi}_2 - \bar{\xi}_1} \int_{\bar{\xi}_1}^{\bar{\xi}_2} \Pi(\bar{\xi}_*, k) d\bar{\xi}_* = 2 \frac{|D_\infty(\xi_*)|^2}{|h''_*|} \frac{1}{k(\bar{\xi}_2 - \bar{\xi}_1)} \sum \frac{|C_n|^2}{n^2} \\ &\quad \{ \sin[(1 + \bar{\xi}_1)kn] - \sin[(1 + \bar{\xi}_2)kn] \} = O(1/k) \ll 1 \end{aligned} \quad (\text{IV.20})$$

Hence, the  $\Pi/k\bar{z}$  contributions to the (spatial) average of the mean square (IV.26a) can be omitted along with other remainders belonging to the order  $1/k$  higher. Therefore, the square-root of the (spatial  $x$ ) average of the (timewise) mean square of  $p'$  may be represented as

$$|p'|_{RAMS} \equiv | \langle |p'|_{MS}^2 \rangle |^{1/2} \sim \sqrt{\frac{2}{k\bar{z}}} \frac{|D_\infty(\xi_*)|}{\sqrt{|h''_*|}} \sqrt{\sum_{-\infty}^{\infty} \frac{|C_n|^2}{|n|}} \quad (\text{IV.21})$$

for large  $k\bar{z}$  [excluding  $x'=O(1)$ ], and remains indeed at the order  $1/\sqrt{k\bar{z}}$ .

#### IV.4 Surface Wave Train Generated by Continuous Spectra

Solution with surface waves generated by a continuous spectrum can be built up from the synchronous solution of the monochromatic surface waves pertaining to surface wave number  $k$ . Of interest is the question how the integrated result from a continuous  $k$ -distribution may alter the field behaviour for  $k\bar{z} \gg 1$ , the inverse square-root rule in particular. The two terms of  $\hat{p}_2$  in (IV.8) associated with the two

question how the integrated result from a continuous  $k$ -distribution may alter the field behaviour for  $k\bar{z} \gg 1$ , the inverse square-root rule in particular. The two terms of  $\hat{p}_2$  in (IV.8) associated with the two stationary  $\xi_*$  values together with their products with  $e^{-i\Omega t} (= e^{-ikt})$ , indicate that the integrated effect in question may in essence be seen by examining the effects of  $\bar{z}$ ,  $a$  and  $k_0$  in the integral

$$I(k_0, \bar{z}; a) = \frac{1}{2a} \int_{k_0-a}^{k_0+a} \frac{e^{ikz}}{\sqrt{k}} dk \quad (\text{IV.22a})$$

where functions which do not vary sensibly with  $k$  and  $\bar{z}$  have been omitted, and  $2a$  is the wave number band width of the distribution. Note that unlike  $e^{ikz}$  and  $1/\sqrt{k}$ , the functions  $D_\infty(\xi_*)$  in (IV.8 b) do not vary significantly with  $k$ , and that in the limit of a vanishing band width, the integral becomes

$$I \sim \frac{e^{ikz}}{\sqrt{k}} \quad (\text{IV.22b})$$

recovering the result which corresponds to the synchronous solution. Recasting the integral differently, we have

$$I(k_0, \bar{z}; a) = \frac{1}{a\bar{z}} \int_{v_1}^{v_2} e^{iv^2} dv \quad (\text{IV.23a})$$

with

$$v_1 = \sqrt{(k_0 - a)\bar{z}}, v_2 = \sqrt{(k_0 + a)\bar{z}} \quad (\text{IV.23b})$$

Under a large  $k_0\bar{z}$ , we have

$$I \sim \frac{-i}{2a\bar{z}} \left| \frac{e^{iv^2}}{v} \right|_{v_1}^{v_2}$$

thus,

$$I \sim \frac{-ie^{ik_0\bar{z}}}{2(a\bar{z})\sqrt{k_0\bar{z}}} \left[ \frac{e^{ia\bar{z}}}{\sqrt{1 + \frac{a}{k_0}}} - \frac{e^{-ia\bar{z}}}{\sqrt{1 - \frac{a}{k_0}}} \right] \quad (\text{IV.24})$$

If  $a\bar{z} \ll 1$  and  $k_0\bar{z} \gg 1$ , which implies a narrow bandwidth  $a/k_0 \ll 1$ ,

$$I \sim \frac{e^{ik_0\bar{z}}}{\sqrt{k_0\bar{z}}} \left[ 1 + i \frac{1}{k_0\bar{z}} \right] \quad (\text{IV.25})$$

and the result for the monochromatic case (IV.22 b) is recovered. Significantly, the order of magnitude of  $I$ , hence that of  $p'$ , established by the inverse square root law, namely,

$$|I| = O[1/\sqrt{k_0\bar{z}}] \quad (\text{IV.26a})$$

is seen from (IV.24) to remain for a wider wave-number band width as long as

$$a\bar{z} = O(1), \quad 1/k_0\bar{z} = O(1), \quad (\text{IV.26b})$$

except if  $a/k_0$  is too close to one. Numerical calculations for wild ranges of  $k_0\bar{z}$  and  $a\bar{z}$  show that departure from cylindrical-spreading rule, (IV.26a), remain insignificant as long as

$$a\bar{z} \leq 1.5, \quad k_0\bar{z} \geq 2 \quad (\text{IV.26c})$$

For bandwidth wider than this, the rule (IV.26a) does not hold; an attenuate rate as high as  $|I| \sim (\bar{z})^{-3/2}$  under  $k_0\bar{z} \gg 1$  may be expected, in view of (IV.24). In such a case neither can a distinct wave length nor recognizable frequency be detected from the surface waves.

## Appendix V Notes On Power-Law Shear Speed

One important improvement needed in the foregoing analysis is the relaxation in the assumption of a constant elastic properties, particularly with regards to the  $C_s$  behaviour next to the interface. While the power-law model with

$$C_s = \text{const.}(z)^\omega \quad (0 < \omega) \quad (\text{V.1})$$

has not received endorsement from most researchers in marine seismology and related fields, the unrefutable fact is that for certain sediments, materials near the interface  $C_s$  is typically much lower than its value in the deeper part of the sediment. The power-law model may help bringing certain features unaccounted for by the homogenous model, but it raises an analytical issue requiring more thorough studies. In the following, we outline the problem with the power-law model and note the issues to be resolved.

### Wave-Train Solution

The PDE for the  $\bar{\Psi}$  field with a power-law shear-wave speed like (V.1) is

$$\left[ \sigma^2 F(z) \frac{\partial^2}{\partial x^2} - \frac{\partial^2}{\partial z^2} \right] \bar{\Psi} = 0 \quad (\text{V.2a})$$

where  $x$  and  $z$  have been normalized by scalars  $\lambda$  and  $z_*$  respectively, so that

$$F(z) \equiv M_s^2 - 1 = \left( \frac{U}{C_s} \right)^2 - 1 \quad (\text{V.2b})$$

$$\sigma \equiv z/\lambda = kz_*/2\pi \quad (\text{V.2c})$$

and  $z_*$  is chosen to be where  $F$  vanishes and changes sign

$$F(1) = 0 \quad (\text{V.2d})$$

For a shear-wave speed, of the form of (V.1) in the region  $0 < z < z_*$ , the function  $F$  becomes simply

$$F(z) = (z)^{-2\omega} - 1 \quad (\text{V.3})$$

If the wave-train solution form  $\bar{\Psi} = e^{i\alpha x} \psi$  is stipulated, (V.2a) yield an ODE for  $\psi$

$$\left[ \frac{d^2}{dz^2} + \sigma^2 F(z) \right] \psi = 0 \quad (\text{V.4a})$$

where  $F(z)$  has the properties

$$F \sim z^{-2\omega} \rightarrow \infty, \text{ as } z \rightarrow 0 \quad (\text{V.4b})$$

$$F \sim \text{const.}(1-z) \rightarrow 0, \text{ as } z \rightarrow 1 \quad (\text{V.4c})$$

The transition through  $z=1$  can be expected to be smooth, and the evanescent solution is expected to be able to accept the far-boundary condition at some  $z > 1$  or  $z \rightarrow \infty$ . The additional data needed for  $\psi$ 's determination must be furnished by the three conditions at the interface (4.8 a,b,c) and the condition on the (flat) water surface, as those in the analysis for the homogenous sediment model.

For  $\omega \neq 1/2$  and  $\omega < 1$ , (V.4a) yields an expansion of  $\psi$  for a sufficiently small  $z$

$$\psi = C_1 \sqrt{z} Z_p(\xi) + C_2 \sqrt{z} Z_{-p}(\xi) \quad (\text{V.5a})$$

where  $Z_p$  and  $Z_{-p}$  are Bessel functions with

$$\xi \equiv \frac{\sigma}{1-\omega} z^{1-\omega}, \quad p = \frac{1}{2(1-\omega)} \quad (\text{V.5b, c})$$

where  $C_1$  and  $C_2$  are the two arbitrary constants.

### Solution Behaviour Next to Interface

Next to the interface ( $z=0$ ) (V.4) yields the behaviour

$$\begin{aligned} \psi \sim & C_1 \left( \frac{\sigma}{2(1-\omega)} \right)^p \frac{z}{\Gamma(1+p)} \left[ 1 - \left( \frac{\sigma}{2(1-\omega)} \right)^2 \frac{z^{2(1-\omega)}}{p+1} + \dots \right] \\ & + C_2 \left( \frac{\sigma}{2(1-\omega)} \right)^{-p} \frac{1}{\Gamma(1-p)} \left[ 1 - \frac{\Gamma(1-p)}{\Gamma(2-p)} \left( \frac{\sigma}{2(1-\omega)} \right)^2 z^{2(1-\omega)} + \dots \right] \end{aligned} \quad (\text{V.6a})$$

where  $\Gamma$  is the gamma function. It follows that, next to the interface,

$$\psi_z \sim C_1 O(1) + C_2 O(z^{1-2\omega}) \quad (\text{V.6b})$$

$$\psi_{zz} \sim C_1 O(z^{1-2\omega}) + C_2 O(z^{-2\omega}) \quad (\text{V.6c})$$

For simplicity, we shall consider only the case with  $\omega < 1/2$ . The possible contributions  $\psi$  to the interface boundary conditions and the problem are seen as follows.

### The Problem

Whereas, with the solution behaviour (V.6a) and the fact that  $\mu \propto (C_s)^2$ , indicate the entry of the constant  $C_2$  in (4.8a) and the influence of  $C_1$  and  $C_2$  on the second condition (4.8b), the last interface condition (4.8c) on the shear stress would have to require  $C_2$  to vanish, since

$$\mu_2 \frac{\partial^2 \bar{\psi}}{\partial z^2} \propto \mu \frac{\partial^2 \psi}{\partial z^2} \propto C_2 \quad (\text{V.7})$$

must vanish. On the other hand, the transition at the *turning* point  $z=1$  demands the proportion  $C_1/C_2 = O(1) \neq 0$ . Thus the power-law model with  $C_s$  vanishing at the interface would appear to be a "gate keeper". That is,  $\bar{\psi}$  would vanish altogether for the power-law model, unless the sediment layer were thin enough to avoid the turning point, i.e.  $z < 1$ .

### Need of a new model

A modification in the mathematical model may help resolving the issue: (i) Inclusion of the tangential stress component and of tangential displacement into the interface condition; (ii) Introduction of a viscous boundary layer for water to the model with a non-slip boundary. How this problem was resolved in the works of Godin and Chapman(1998) of which the full text is unavailable is unclear.